Politecnico di Milano

Facoltà di Ingegneria Industriale

Corso di Laurea in Ingegneria Meccanica

A comparison of different turbulence models for the simulation of the heat transfer from a wall-mounted matrix of cubes

Relatore: Prof. Fabio Inzoli

Correlatore: Ing. Paolo Lampitella

Tesi di Laurea di:

Federico Vandoni Matr. 720528

Anno accademico 2010/11

Abstract

The flow and heat transfer characteristics in a matrix of surface mounted cubes are investigated by means of an unstructured finite volume solver and the numerical results are validated against experimental data. Several simulations have been performed, with different turbulence models: the classical URANS models ($k-\varepsilon$, $k-\omega$), a non-linear $k-\varepsilon$ model and the more recent Scale Adaptive Simulation (SAS); in addition, also Large Eddy Simulations (LES) have been performed, in order to investigate their performances on computational grids which were designed mainly for URANS applications. The comparison is made for first and second order statistical quantities as well as for the general flow structure. The LES results show several characteristics which are out of the modelling capabilities of classical URANS models (including SAS) and, in turn, influence the local temperature distribution. Also, for this kind of flow, LES higher accuracy is shown to be only slightly influenced by the grid resolution and accurate results are achievable at costs even smaller than those typical of URANS computations.

Abstract

Lo scambio termico ed il flusso intorno ad una matrice di cubi è stato analizzato utilizzando un codice non strutturato ai volumi finiti: i risultati delle simulazioni sono poi stati messi a confronto con i dati sperimentali disponibili. Sono state effettuate simulazioni con diversi modelli di turbolenza: i tradizionali modelli URANS ($k-\varepsilon$, $k-\omega$), un modello $k-\varepsilon$ non lineare e la recente "Scale Adaptive Simulation" (SAS); in aggiunta, sono state effettuate anche delle simulazioni "Large Eddy" (LES), per valutarne le prestazioni su griglie di calcolo per applicazioni URANS. Nel confronto sono state considerate quantità statistiche del primo e del secondo ordine, nonché la struttura generale del flusso. A differenza dei modelli URANS e SAS, la LES è stata in grado di ricostruire in modo estremamente dettagliato le caratteristiche dinamiche del flusso, che giocano un ruolo fondamentale nella previsione della distribuzione locale di temperatura. Inoltre, nel caso analizzato, l'accuratezza dei risultati della LES si è dimostrata poco dipendente dal passo di griglia utilizzato ed il costo computazionale è risultato addirittura minore di quello delle simulazioni URANS.

Contents

List of Figures

List of Tables

Nomenclature

Greek characters

α	Coefficient of the $k-\omega$ model
α^*	Damping function of the $k-\omega$ model
β, β^*	Constants of the $k-\omega$ model
Γ_t	Turbulent diffusivity
Γ_φ	Diffusion coefficient for the scalar φ
Δ	Filter cutoff width
δ_v	Viscous length scale
δ_{ij}	Kronecker delta
$\widehat{\Delta}$	Test filter cutoff width
ε	Dissipation rate of turbulent kinetic energy
ε_t	User defined tolerance
ε_0	Instaneous dissipation rate
η	Kolmogorov length scale
η_2	Constant of the SAS model
κ	Von Karman constant

λ	Thermal conductivity
μ	Dynamic viscosity
μ_t	Turbulent viscosity
μ_{SGS}	Subgrid scale viscosity
ν	Kinematic viscosity
ρ	Density
σ_k	Turbulent Prandtl number for kinetic energy
$\sigma_{\omega 2}$	Constant of the $k-\omega$ model
σ_ε	Turbulent Prandtl number for dissipation rate
σ_{phi}	Constant of the SAS model
$\tau(l)$	Characteristic time scale of an eddy of size l
τ_η	Kolmogorov time scale
τ_{ij}	Subgrid scale stress tensor
τ_0	Time scale of the largest eddies
u_η	Kolmogorov velocity
$\overline{\varphi}$	Mean value of φ
Φ	Heat flux
φ	Generic scalar
$\varphi^{'}$	Fluctuation of the scalar quantity φ
$\overline{\varphi}(\mathbf{x},t)$	Space filtered scalar φ
Ψ	Generic function
ω	Specific dissipation rate

$\widehat{\Omega_{ij}}$ Normalized mean rate of rotation tensor

Roman characters

A_f Face area

b_{ij} Normalized Reynolds stress anisotropy

c Constant of the SAS model

c_0, c_i Generic cell centres

$C_1, \cdots, C_7$ Constants of the third order non linear $k - \varepsilon$ model

c_p Specific heat at constant pressure

C_s Smagorinsky constant

$C_{1\varepsilon}, C_{2\varepsilon}$ Constants of the $k - \varepsilon$ model

C_μ Turbulent viscosity constant in the $k - \varepsilon$ model

c_μ Constant of the SAS model

CFL Courant-Friedrichs-Levy number

$[D]$ Discrete divergence operator (in matrix form)

d Distance to the closest wall

d_i Generic coefficient

D_ω Cross-diffusion term

$E(k)$ Energy spectrum function

f Frequency

f Generic cell face

F_1, F_2 Blending functions

f_μ Damping function of the third order non linear $k - \varepsilon$ model

$[G]$ Discrete gradient operator (in matrix form)

G Filter function

H Cube height

h Heat transfer coefficient

I Identity operator

k Turbulent kinetic energy

K_0 Universal Kolmogorov constant

$[L]$ Discrete diffusion term (in matrix form)

L Characteristic length scale

l Length scale

l_0 Length scale of the largest eddies

l_i Geometry-dependent coefficient

l_m Mixing length

l_{DI} Demarcation length scale between the dissipation range ($l < l_{DI}$) and the inertial subrange ($l > l_{DI}$)

l_{EI} Demarcation length scale between the energy containing range of eddies ($l > l_{EI}$) and smaller eddies ($l < l_{EI}$)

L_{ij} Resolved stress

L_{SGS} Mixing length for the subgrid scales

M_{ij} Scaled composite rate of strain tensor

$[N]$ Discrete convective term (in matrix form)

$\vec{n}$ Normal unity vector

n	Number of cells
$\overline{p}$	Space-filtered value of p
p	Pressure
p_j	Generic coefficient
P_k	Production of k
P_ω	Production of ω
PSD	Power spectral density
$\mathcal{P}_{ij}$	Reynolds stress production rate
Q	Second invariant of the velocity gradient tensor
Q_{SAS}	Source term of the SAS model
R_{ij}	Reynolds stress tensor
Re	Reynolds number
Re_0	Reynolds number based on u_0,l_0
Re_H	Cube-height-based Reynolds number
Re_y	Reynolds number based on y
Re_τ	Friction Reynolds number
$\mathcal{R}_{ij}$	Pressure rate-of-strain tensor
$\vec{S}$	Generic momentum source term
$\widehat{S_{ij}}$	Normalized mean rate of strain tensor
S	Cube face-to-face distance
S	Scalar invariant of the strain rate tensor
S_φ	Source term for φ

S_{ij} Mean rate of strain tensor

s_{ij} Rate of strain tensor

St Strouhal number

T Time interval

T_{ij} Subgrid scale stress tensor based on the test filter

T_{ref} Reference temperature

$\mathcal{T}$ Rate of energy transfer

$\mathcal{T}(l)$ Rate of transfer of energy from eddies larger than l to thos smaller than l

$\mathcal{T}_{EI}$ Rate of transfer of energy from large eddies to small eddies

$\overline{u}$ Space-filtered value of u

$\vec{u}$ Velocity vector

U Mean value of u

u x component of the velocity

$u(l)$ Characteristic velocity of an eddy of size l

$u^{'}$ Fluctuation of u

u^{+} Mean velocity normalized by the friction velocity

u_0 Velocity scale of the largest eddies

u_b Bulk velocity

u_i i component of the velocity vector

V Cell volume

v y component of the velocity

w z component of the velocity

W_{i0}^{j} j-th component of the weight used for the gradient reconstruction

x Cartesian coordinate

$\mathbf{x}$ Position vector

y Cartesian coordinate

y Distance from the wall

y^{+} Distance from the wall normalized by δ_v

z Cartesian coordinate

Symbols

δp Pressure correction

Δt Time step

Chapter 1

Introduction

1.1 Introduction

The prediction of turbulent airflow and heat transfer around bluff bodies is a matter of considerable importance. A typical example is the cooling of electronic components attached to a printed circuit board, which act as concentrated heat sources: long term reliability can be ensured only adopting an efficient heat removal technique, in order to avoid excessive local overheating. Furthermore, the continuous tendency to component miniaturisation and power density increment makes the accurate prediction of heat transfer a fundamental prerequisite of optimum component design.

Another interesting application is the internal cooling of gas turbine blades: the engine efficiency can in fact be improved increasing the temperature of combustion gases, but this is possible only if an efficient blade cooling method is provided. The cooling fluid passes through internal ducts which are equipped with wall-mounted protrusions and ribs, in order to enhance heat removal: it is therefore very important to provide an accurate prediction of local heat transfer, since a local overeating could cause serious damages to the blades and, consequently, to the whole engine.

Many other examples can be found, such as flow around buildings in urban areas: in these cases the attention is focussed on aerodynamic forces or dispersion of pollutants.

An idealised model which can be used to investigate the complex flow physics involved in the practical applications listed above is -in spite of the differences with respect to the real configurations- a matrix of wall-mounted cubes.

Such a case was experimentally investigated by Meinders and Hanjalić [7] and the gathered data served as reference for the 6^{th} and 8^{th} ERCOFTAC Workshop [4] on refined flow and turbulence modelling. In fact, according to the periodic conditions of the flow and the complex involved turbulence phenomena, this case is also well suited for benchmarking and validation of turbulence models and numerical methods.

The conclusions of the two workshops substantiate the fact that RANS computations are not able to reproduce the main features of the flow due to

the assumption of steadiness. In contrast, unsteady computations perform considerably better, with large eddy simulations (LES) and direct numerical simulations (DNS) achieving an excellent agreement with the available experimental data.

In the present work, different turbulence models have been employed to simulate the turbulent flow and the heat transfer of the same configuration considered by Meinders and Hanjalić. The obtained results have then been compared with the experimental data provided by the measurements in order to find the model which yields the most accurate results, in consideration of the computational costs. Furthermore also the influence of the computational grid has been investigated: computations have therefore been performed on two different meshes, a coarse one and a fine one.

The *Unsteady Reynolds averaged Navier-Stokes* (URANS) approach has first been adopted, and several models have been tested: the standard and the non linear version of the $k - \varepsilon$ model, the $k - \omega$ model and the *Scale Adaptive Simulation*, which is an hybrid between the URANS and the *large eddy simulation* (LES) approach. Then, two LES on both computational grids have been performed, in order to investigate their performances on meshes which were specifically designed for URANS applications.

It is important to notice that the aim of the present work was neither to improve existing models in order to obtain the best conformance with the experimental measurements, nor exclusively to perform LES simulations: the main purpose was in fact to investigate the performances and the accuracy of the standard URANS and LES models, as they are implemented on the solver.

All computations have been performed with the commercial solver ANSYS FLUENT 12.2.1.

1.2 Thesis outline

In the following chapters first a brief description of turbulence phenomenology and turbulence modelling will be given. Then the main characteristics of the solver ANSYS FLUENT will be discussed, focussing in particular on the

numerical schemes which were adopted in the performed simulations. The analysed case will then be described, with a brief explanation of the experimental and numerical setup, with particular attention to the characteristics of the mesh.

Subsequently, results will be presented and compared with experimental data. Some additional results will also be shown, for which a comparison with experiments has not been possible, since measured data were not available.

Finally some remarks about computational costs will be made, and the conclusions will be drawn.

Chapter 2

Turbulent flows

2.1 Phenomenology of turbulence

It is easy to find examples of turbulent flows in our everyday life, such as smoke from a chimney or water in a waterfall. One can also immediately observe what the characteristics of turbulent flows are: irregularity, presence of eddies of different size, unsteadiness etc.

All flows tend to become turbulent under certain conditions. It is possible to describe the level of turbulence by means of a non-dimensional parameter, the *Reynolds number*, that is defined as follows:

$$Re = \frac{LU}{\nu} \tag{2.1}$$

where L and U are respectively a characteristic length and velocity of the flow while ν is the kinematic viscosity of the fluid. The Reynolds number is essentially a ratio between inertial forces and viscous effects. Flows dominated by viscosity are called laminar and are characterized by a regular spatial and temporal behaviour. If the Reynolds number Re of this flow increases, inertial effects become more important than the viscous ones and the flow becomes turbulent: the flow looses regularity and its characteristics start exhibiting chaotic features in time and space. Figure 2.1 shows an example of flows at different Reynolds number. All flows encountered in engineering practice are turbulent; besides this, turbulence significantly increases the transport and mixing of matter, momentum and heat in flows, therefore its study is of great practical importance.

Turbulence is a phenomenon characterized by rotational flow structures called turbulent eddies, which have a very wide range of length scales. Eddies of size l have a characteristic velocity $u(l)$ and time scale $\tau(l) \equiv l/u(l)$: if the size l decreases, also $u(l)$ and $\tau(l)$ decrease.

There is a wide range of turbulent eddies: the largest ones are essentially inviscid, because viscous effects are negligible compared to inertial effects; the smallest ones are instead dominated by viscosity so that their kinetic energy is converted into thermal internal energy. Furthermore, the largest eddies interact with the main flow and receive energy from it.

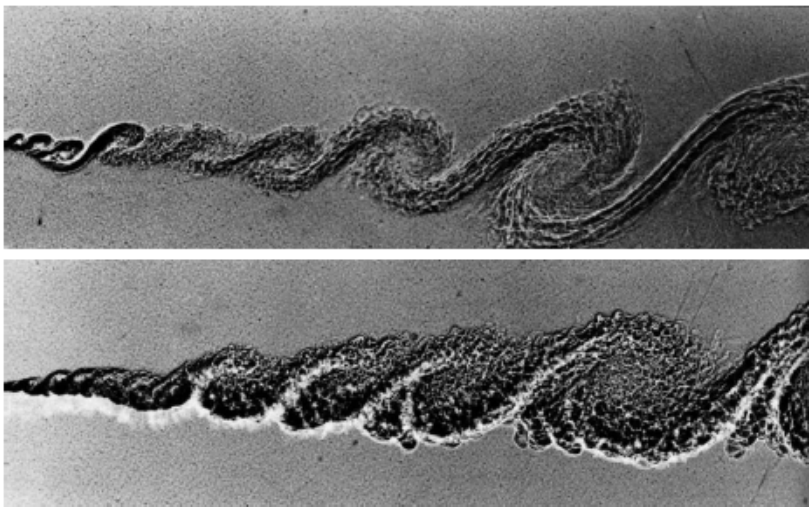

Figure 2.1: Turbulent mixing layer. The Reynolds number of the flow in the picture below is two times the Reynolds number of the one in the picture above. (From [17])

Through the so called *vortex stretching* and *eddy break up* processes the energy is then handed down to progressively smaller eddies until it is dissipated at the smallest scales: this phenomenon is called *energy cascade*.

The largest eddies have energy of order u_0^2 and time scale $\tau_0 = l_0/u_0$, so that the energy transfer rate can be supposed to be $u_0/\tau_0 = u_0^3/l_0$. Since the small eddies -due to their small lenght and time scales- are supposed quickly to adapt to the energy transfer from the largest ones, it can also be supposed that small eddies are in dynamic equilibrium with large eddies. Under this hypothesis, it can be assumed that the viscous dissipation ε is nearly equal to the energy transfer at the smaller scales (supposed to be u_0^3/l_0).

The typical spectrum of a turbulent flow contains energy across a wide range of spatial frequencies or wavenumbers, as shown in figure 2.2.

A. N. Kolmogorov, who in the 1940s carried out fundamental work on the structure of turbulence, formulated three hypothesis, on which his theory is based. The first one is:

1. *Hypothesis of local isotropy*: At sufficiently high Reynolds number, the small scale turbulent motions ($l \ll l_0$) are statistically isotropic.

It is then useful to introduce a length scale l_{EI} as demarcation between the

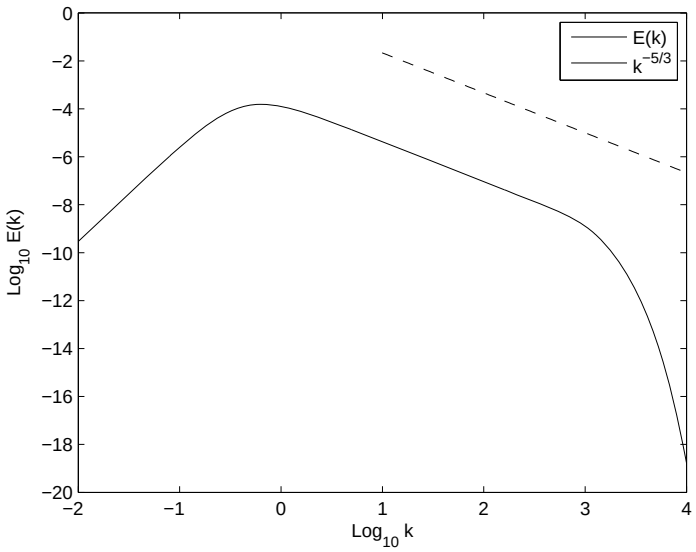

Figure 2.2: Energy spectrum of turbulence

anisotropic large eddies ($l > l_{EI}$) and the isotropic small eddies ($l < l_{EI}$): this range of small scale motions is the so called *universal equilibrium range*. Every information about geometry and direction of the large scales is supposed to be lost by passing down the cascade: therefore the statistics of the small scale motions are similar in every high-Reynolds-number turbulent flow. It is important to understand on which parameters does this statistically universal state depend. The two most important processes that take place in the energy cascade are the energy transfer through different scales and the viscous dissipation. A plausible hypothesis is then that the important parameters are the rate $\mathcal{T}_{EI}$ at which the small scales receive energy from the large ones, and the kinematic viscosity ν. According to the equilibrium hypothesis, the dissipation rate ε is determined by the energy transfer rate $\mathcal{T}_{EI}$, so it can be assumed that these two rates are nearly equal: $\varepsilon \approx \mathcal{T}_{EI}$. Hence the second hypothesis introduced by Kolmogorov:

2. *First similarity hypothesis*: In every turbulent flow at sufficiently high Reynolds number, the statistics of the small scale motions ($l < l_{EI}$) have a universal form that is uniquely determined by ν and ε.

If the two parameters ν and ε are given, the only length, velocity and time scales that can be formed from these are:

$$\eta \equiv \left(\frac{\nu^3}{\varepsilon}\right)^{\frac{1}{4}} \tag{2.2}$$

$$u_\eta \equiv \ (\varepsilon\nu)^{\frac{1}{4}} \tag{2.3}$$

$$\tau_\eta \equiv \left(\frac{\nu}{\varepsilon}\right)^{\frac{1}{2}} \tag{2.4}$$

These are the so called *Kolmogorov scales*, which characterize the smallest eddies. It should be observed that the Reynolds number based on the Kolmogorov scales is:

$$\frac{\eta u_\eta}{\nu} = 1 \tag{2.5}$$

It means that at the smallest motion scales the effects due to inertia are comparable to those due to viscosity, so dissipation can take effect. Considering:

$$\varepsilon_0 \approx \frac{{u_0}^3}{l_0} \tag{2.6}$$

$$Re_0 = \frac{u_0 l_0}{\nu} \tag{2.7}$$

$$\tau_0 = \frac{l_0}{u_0} \tag{2.8}$$

and the definition of η, the following quantities can be derived:

$$Length\ scale\ ratio: \quad \frac{\eta}{l_0} \approx \left(\frac{\nu^3}{u_0^3 l_0^3}\right)^{\frac{1}{4}} = {Re_0}^{-\frac{3}{4}} \approx Re^{-\frac{3}{4}} \tag{2.9}$$

$$Velocity\ scale\ ratio: \quad \frac{u_\eta}{u_0} \approx \left(\frac{\nu}{u_0 l_0}\right)^{\frac{1}{4}} = {Re_0}^{-\frac{1}{4}} \approx Re^{-\frac{1}{4}} \tag{2.10}$$

$$Time\ scale\ ratio: \quad \frac{\tau_\eta}{\tau_0} \approx \left(\frac{\nu}{u_0 l_0}\right)^{\frac{1}{2}} = Re_0^{-\frac{1}{2}} \approx Re^{-\frac{1}{2}} \tag{2.11}$$

It must now be observed that if the flow Reynolds number is high, the ratio η/l_0 sensibly decreases and it can therefore be found a very large range of scales of size l that are much smaller than l_0 but still very large compared with η, so that $l_0 \gg l \gg \eta$.

It can then be supposed that these eddies are still dominated by inertial effects because they are too large for viscous dissipation to take effect, but still small enough to be independent from the large scales. This leads to the third Kolmogorov's hypothesis:

3. *Second similarity hypothesis*: In every turbulent flow at sufficiently high Reynolds number, the statistics of the motions of scale l in the range $l_0 \gg l \gg \eta$ have a universal form that is uniquely determined by ε, independent of ν.

It is thus convenient to split the universal equilibrium range ($l < l_{EI}$) in two subranges: the *inertial subrange* for $l_{EI} > l > l_{DI}$ and the *dissipation range* for $l < l_{DI}$. For $l > l_{EI}$ there is the so called *energy-containing range*: eddies of this size range contain the bulk of the energy[1].

In the inertial subrange the viscosity ν cannot be used to form length, velocity and time scales, however, if a length l is given, it is possible to derive the following relations:

$$u(l) = (\varepsilon l)^{\frac{1}{3}} = u_\eta \left(\frac{l}{\eta}\right)^{\frac{1}{3}} = \frac{u_\eta}{u_0} u_0 \left(\frac{l\ l_0}{l_0\ u_0}\right)^{\frac{1}{3}} = u_0 \left(\frac{l}{l_0}\right)^{\frac{1}{3}} \tag{2.12}$$

$$\tau(l) = \left(\frac{l^2}{\varepsilon}\right)^{\frac{1}{3}} = \tau_\eta \left(\frac{l}{\eta}\right)^{\frac{2}{3}} = \frac{\tau_\eta}{\tau_0} \tau_0 \left(\frac{l\ l_0}{l_0\ \tau_0}\right)^{\frac{2}{3}} = \tau_0 \left(\frac{l}{l_0}\right)^{\frac{2}{3}} \tag{2.13}$$

These two equations have some important consequences. First of all they confirm the assumption that the velocity and time scales decrease with l.

[1]The suffixes EI and DI respectively indicate the boundary between energy containing range and inertial subrange and the boundary between dissipation and inertial subrange.

Secondly, considering an energy of order $u^2(l)$ and a time scale $\tau(l)$ to be associated to an eddy of size l, the rate $\mathcal{T}(l)$ at which energy is transferred from motions of size l to the smaller ones can be expected to be:

$$\frac{u^2(l)}{\tau(l)} = \frac{(\varepsilon l)^{\frac{2}{3}}}{\left(\frac{l^2}{\varepsilon}\right)^{\frac{1}{3}}} = \varepsilon \tag{2.14}$$

$\mathcal{T}$ is therefore independent of l and equal to ε: it means that the energy transfer rate remains constant through the energy cascade:

$$\mathcal{T}_{EI} = \mathcal{T} = \mathcal{T}_{DI} = \varepsilon \tag{2.15}$$

that is the equilibrium hypothesis: $\varepsilon \approx \mathcal{T}_{EI}$.

As mentioned above, referring to figure 2.2, the energy content of a turbulent flow is distributed among a wide range of frequencies or wavenumbers. It is useful to introduce the *energy spectrum function* $E(k)$, that is the amount of kinetic energy, per unit mass and wavenumber, associated to the wavenumber k; its typical trend is shown in figure 2.2.

According to the first similarity hypothesis, when $(l < l_{EI})$ the governing parameters are ν and ε: following the same reasoning as before, the energy spectrum function can be shown to have -in the universal equilibrium range- the following form:

$$E(k) = \varepsilon^{2/3} k^{-5/3} \Psi(k\eta) \tag{2.16}$$

where $\Psi(k\eta)$ is a function that takes account for viscosity. If k tends to zero the size of the eddies tends to increase and viscous effect become negligible, as assumed in the second similarity hypothesis. The function $\Psi(k\eta)$ tends therefore to a constant value K_0. For the inertial subrange it can then be written:

$$E(k) = K_0 \varepsilon^{2/3} k^{-5/3} \tag{2.17}$$

which is the well known Kolmogorov $-5/3$ spectrum and $K_0 \approx 1.5$ is the universal Kolmogorov constant.

It emerges from the previous explanations that the fundamental problem in the study of turbulence is the presence of a very large number of space

and time scales.

A powerful tool to investigate the features of fluid flow is computational fluid dynamics (CFD), which essentially consists in a numerical solution of the discretized system of the Navier-Stokes equations. Details about numerical procedures will be explained in chapter 3; now only the aspects concerning turbulence will be treated.

As mentioned above, turbulent flows are characterised by the presence of an extremely wide range of space and time scales: this means that in order to perform a correct simulation, the Navier-Stokes equations have to be discretized with space and time steps which are at least equal to the smallest scales present in the flow. Nonetheless, the computational costs will sensibly increase if the size of the space and time steps decreases.

The approach that leads to the most correct results is the *direct numerical simulation* (DNS): it is based on the solution of the Navier-Stokes equations, which govern the flow of Newtonian fluids, without any kind of averaging or approximation.

The main problem of such a kind of simulation is -as already noticed- the computational cost. A DNS requires in fact the grid resolution to be so high that all scales of motion are resolved and all the kinetic energy dissipation is captured. This phenomenon -as explained above- is due to viscosity and takes place at the smallest turbulence scales, whose characteristic length is η.

A rough estimate of the minimum number of cells needed to perform a DNS can be found assuming the *viscous length scale* δ_v, which can be computed from the flow Reynolds number and from the channel height, as an estimate of η. This approximation is valid only in case of simple channel flows, for which the following relation between the Reynolds number and the *friction Reynolds number* can be found:

$$Re_\tau = \frac{\delta}{\delta_v} = 0.09 \cdot Re^{0.88} \tag{2.18}$$

where δ is half the channel height L. Considering, for example, a simple

channel with the same L and Re of the case analysed in the present work:

$$L = 3.4H = 0.051\ m \tag{2.19}$$

$$Re \approx 13000 \tag{2.20}$$

yields:

$$\delta_v = \frac{\delta}{Re_\tau} = \frac{1.7H}{375} = 6.8 \cdot 10^{-5} \tag{2.21}$$

Which is the maximum grid spacing that ensures a correct resolution of all turbulent scales. It means that considering a computational domain with size:

$$(4 \cdot 4 \cdot 3.4)\, H \tag{2.22}$$

and assuming an uniform grid spacing, the minimum needed number of cells is:

$$n = \left(\frac{4H}{\delta_v}\right)^2 \cdot \left(\frac{3.4H}{\delta_v}\right) \approx 5.8 \cdot 10^8 \tag{2.23}$$

So, in spite of the small dimensions of the computational domain, the number of cells that are needed for a DNS is very large and this implies extremely high computational costs.

It must be remarked that if the Reynolds number is not too high and a grid with non-uniform spacing is adopted, the number of cells can be kept sensibly lower: for example, a DNS of the same case analysed in the present work has been run ([18],[19]) adopting a grid of circa 9 million cells.

However, DNS still remain too costly for engineering applications, and are therefore used only as a research tool.

Two more practical approaches to the simulation of turbulent flows are possible. Both are based on the fact that most of times a very accurate description of all the turbulent structures is not necessary: engineers are in fact normally interested only in a few quantitative properties of a turbulent flow, such as average forces on a body or the degree of mixing of two flows.

The main idea is to resolve only the biggest scales and find a suitable model for the smaller ones: according to the size of the minimum resolved scale it can be distinguished between the *Reynolds-averaged Navier-Stokes*

(RANS) approach and the *large eddy simulation* (LES) approach.

2.2 RANS and URANS approach

This method is based on ideas proposed by Osborne Reynolds at the end of the 19^{th} century. The attention is focused on the mean flow and the effects of turbulence on it. Since turbulent flows are chaotic, but characterized by deterministic statistical quantities, Reynolds introduced a distinction between mean and fluctuating quantities. In this way, every generic quantity φ can in general be written as the sum of the mean value $\overline{\varphi}$ and a fluctuating quantity $\varphi^{'}$, so that:

$$\varphi = \overline{\varphi} + \varphi^{'} \tag{2.24}$$

This is the so called *Reynolds decomposition*. The instantaneous continuity and Navier-Stokes equations[2] for an incompressible unsteady isothermal flow are:

$$\frac{\partial (u_i)}{\partial x_i} = 0 \tag{2.25}$$

$$\frac{\partial (\rho u_i)}{\partial t} + \frac{\partial}{\partial x_j}\left(\rho u_j u_i\right) = -\frac{\partial p}{\partial x_i} + \frac{\partial}{\partial x_j}\left(\mu \frac{\partial u_i}{\partial x_j}\right) \tag{2.26}$$

The Reynolds decomposition[3] can now be introduced in equations 2.25 and 2.26. Then, since averaging commutes with summation, integration and differentiation, an average of these equations can be taken, yelding a new system of equations, the unsteady *Reynolds averaged Navier-Stokes equations* (URANS):

$$\frac{\partial (\rho U_i)}{\partial x_i} = 0 \tag{2.27}$$

$$\frac{\partial (\rho U_i)}{\partial t} + \frac{\partial}{\partial x_j}\left(\rho U_j U_i\right) = -\frac{\partial P}{\partial x_i} + \frac{\partial}{\partial x_j}\left(\mu \frac{\partial U_i}{\partial x_j} - \rho \overline{u^{'}_i u^{'}_j}\right) \tag{2.28}$$

[2]For the sake of simplicity, in this chapter the Einstein summation convention will be adopted: when an index variable appears twice in a single term it implies that we are summing over all of its possible values.

[3]According to the Reynolds decomposition, velocity will be written as $u_i = U_i + u_i^{'}$ and pressure as $p = P + p^{'}$

Aside from replacement of instantaneous variables by mean values, the only difference between the averaged and the instantaneous equations is the appearance of the term $\rho\overline{u'_i u'_j}$, which essentially represents the velocity covariances. It derives from the averaging of the non linear convective term, since averaging does not commute with multiplication. This product of fluctuating velocities is associated with convective momentum transfer due to turbulent eddies.

In these extra turbulent stresses, the so called *Reynolds stresses* $R_{ij} = -\rho\overline{u'_i u'_j}$, lies the fundamental problem of turbulence: R_{ij} is in fact a symmetric tensor with six independent components, which are all unknown, so that the total amount of unknowns is ten (pressure, three velocity components, six R_{ij} terms), while the system consist only in four equations. It is therefore necessary to find a suitable model to predict the Reynolds stresses and thus close the system.

Later on the problem of turbulence modelling will be discussed, with particular consideration for the models employed in the performed simulations. Finally a few words must be spent on the term:

$$\frac{\partial\left(\rho U_i\right)}{\partial t} \tag{2.29}$$

Herein lies the difference between RANS and URANS equations, according to the kind of averaging -time or ensemble- which was employed. If a flow is statistically steady, the Reynolds decomposition becomes:

$$\varphi\left(x_i, t\right) = \overline{\varphi}\left(x_i\right) + \varphi'\left(x_i, t\right) \tag{2.30}$$

with

$$\overline{\varphi}\left(x_i\right) = \lim_{T\to\infty} \frac{1}{T} \int_0^T \varphi\left(x_i, t\right) dt \tag{2.31}$$

where t is the time and T the averaging interval, which must be large compared to the typical scale of fluctuations. If T is large enough, $\overline{\varphi}$ does not depend on the time at which the averaging is started and every time dependence is lost. This time averaging leads therefore to the RANS equations,

which are steady because:

$$\frac{\partial (\rho U_i)}{\partial t} = 0 \tag{2.32}$$

as a consequence of the elimination of time-dependence. Otherwise if the flow is unsteady, a sort of moving averaging is used:

$$\overline{\varphi}(x_i, t) = \frac{1}{T} \int_t^{t+T} \varphi \left(x_i, t^{'} \right) dt^{'} \tag{2.33}$$

where T, usually identified with the time-integration step Δt, is supposed to be large compared to the time scale of the fluctuations but small enough to accurately describe the large scale unsteadiness. Time-dependence is instead not eliminated.

Hence the unsteady RANS (URANS) equations listed above are obtained.

2.3 LES approach

Although many efforts have be done in order to develop general-purpose RANS models suitable for a wide range of practical applications, an optimal solution has not been found so far. The main problem is the different behaviour of small and large eddies: the first ones are in fact almost isotropic and do not strictly depend on the geometry of the domain. The second ones are instead very anisotropic, depend directly on geometry and boundary conditions and are generally much more energetic. It is therefore clear that the approximation introduced by RANS equations -where a single turbulence model must describe the collective behaviour of all eddies- is very strong. It makes then more sense to introduce a distinction between large anisotropic eddies and small isotropic ones: the first ones will be directly computed, while the second ones will be modelled. According to their isotropy, in fact, small eddies are easier to capture with a simpler model (compared to RANS). This is the idea on which the *large eddy simulation* is based. In order to obtain a velocity field that contains only the large scale components, an operation of space-filtering must be performed, so that the generic filtered quantity $\overline{\varphi}$

can be written as:

$$\overline{\varphi}\left(\mathbf{x},t\right)=\int_{-\infty}^{\infty}G\left(\mathbf{x},\mathbf{x}^{'},\Delta\right)\varphi\left(\mathbf{x}^{'},t\right)dx^{'} \tag{2.34}$$

where G is the *filter function*, which depends on the *cutoff width* Δ. This width is extremely important, because it precisely determines which scales will be resolved and which ones will be modelled. Of course it makes no sense to specify a cutoff width that is smaller than the grid size: generally a value of $\Delta=\sqrt[3]{\Delta x\Delta y\Delta z}$ is taken, where $\Delta x\Delta y\Delta z$ is equal to the cell volume V. Many filter functions can be used; in FLUENT a box filter is implemented, since this kind of filtering is implicitly provided by the finite volume discretization:

$$G\left(\mathbf{x},\mathbf{x}^{'},\Delta\right)=\begin{cases}1/\Delta^{3} & \left|\mathbf{x}-\mathbf{x}^{'}\right|\leq\Delta/2\\ 0 & \left|\mathbf{x}-\mathbf{x}^{'}\right|>\Delta/2\end{cases} \tag{2.35}$$

where Δ^3 is equal to the cell volume V. Filtering -under the assumption that space-filtering commutes with derivation- leads to the *resolvable-scale equations*:

$$\frac{\partial\left(\rho\overline{u}_{i}\right)}{\partial x_{i}}=0 \tag{2.36}$$

$$\frac{\partial\left(\rho\overline{u}_{i}\right)}{\partial t}+\frac{\partial}{\partial x_{j}}\left(\rho\overline{u_{i}u_{j}}\right)=-\frac{\partial\overline{p}}{\partial x_{i}}+\frac{\partial}{\partial x_{j}}\left(\mu\frac{\partial\overline{u}_{i}}{\partial x_{j}}\right) \tag{2.37}$$

It is important to notice that:

$$\overline{u_{i}u_{j}}\neq\overline{u}_{i}\overline{u}_{j} \tag{2.38}$$

and that $\overline{u_j u_i}$ cannot be computed. It is therefore necessary to find a model for the difference between the two sides of the inequality:

$$\tau_{ij}=\rho\left(\overline{u_{i}u_{j}}-\overline{u}_{i}\overline{u}_{j}\right) \tag{2.39}$$

The quantity τ_{ij} represents the *subgrid scale Reynolds stresses*. Introducing it in the filtered Navier Stokes equations leads to:

$$\frac{\partial\left(\rho\overline{u}_i\right)}{\partial t}+\frac{\partial}{\partial x_j}\left(\rho\overline{u}_i\overline{u}_j\right)=-\frac{\partial\overline{p}}{\partial x_i}+\frac{\partial}{\partial x_j}\left(\mu\frac{\partial\overline{u}_i}{\partial x_j}\right)-\frac{\partial\tau_{ij}}{\partial x_j} \tag{2.40}$$

As mentioned above, it is now necessary to find a suitable model for the subgrid scale stresses: this problem is similar to the closure of the RANS equations, but in this case only the smallest unresolved scales -for which it is easier to provide a good description- will be modelled. In the next sections the models adopted in the performed simulations will be described.

2.4 RANS models

As already explained, both the RANS and the LES equations need to be closed: it means that a model for the Reynolds stresses $R_{ij}=-\rho\overline{u'_i u'_j}$ and for the subgrid scale stresses τ_{ij} must be provided. Since in computational fluid dynamics a very wide range of different problems can be found, several turbulence models are available. No one of these has so far been accepted as being superior for all classes of problems, it is therefore necessary to choose case by case the most suitable models.

All models used in the present computations are based on the presumption that there is an analogy between the action of viscous stresses and Reynolds stresses on the main flow (*Boussinesq hypothesis)*.

In Newton's law of viscosity the viscous stresses are considered to be proportional to the rate of deformation of the fluid elements:

$$\tau_{ij}=\mu\left(\frac{\partial u_i}{\partial x_j}+\frac{\partial u_j}{\partial x_i}\right)-\frac{2}{3}\mu\frac{\partial u_k}{\partial x_k}\delta_{ij} \tag{2.41}$$

where in this case τ_{ij} are the viscous stresses and not the LES subgrid scale stresses. Since turbulent stresses are found to increase as the mean rate of deformation increases [20], it was proposed by Boussinesq (1877) that

Reynolds stresses might be proportional to mean rates of deformation:

$$R_{ij} = -\rho\overline{u'_i u'_j} = \mu_t \left(\frac{\partial U_i}{\partial x_j} + \frac{\partial U_j}{\partial x_i} \right) - \frac{2}{3}\rho k \delta_{ij} \tag{2.42}$$

where

$$k = \frac{1}{2}\overline{u'_i u'_i} \tag{2.43}$$

is the turbulent kinetic energy per unit mass and δ_{ij} is the Kronecker delta ($\delta_{ij} = 1$ if $i = j$, 0 otherwise). Equation 2.41 is exactly the same as equation 2.42, except for the term μ_t, that is the *turbulent* or *eddy viscosity*, and the term $-2/3\rho k\delta_{ij}$, which ensures that the formula gives the correct result for the normal Reynolds stresses (those with $i = j$). As a consequence of the introduction of μ_t, models based on the Boussinesq hypothesis are known as *eddy viscosity models*.

Turbulent transport of heat, mass and other scalar quantities can be similarly modelled: since equation 2.42 shows a proportionality between the turbulent momentum transport and the mean gradients of velocity, the turbulent transport of a scalar is by analogy taken to be proportional to the gradient of the mean value of the transported quantity:

$$-\rho\overline{u'_i \varphi'_i} = \Gamma_t \frac{\partial \overline{\varphi}}{\partial x_i} \tag{2.44}$$

where Γ_t is the *turbulent diffusivity*. Experiments show that the value of the turbulent diffusivity is proportional to that of the turbulent viscosity [20], so that it can be assumed:

$$\Gamma_t \approx \mu_t \tag{2.45}$$

The problem is now to find a suitable value for the turbulent viscosity μ_t. All the models that were used in the present simulations compute μ_t and thus R_{ij} by means of two equations: they are therefore known as *two equations models*, since turbulence models are generally classified according to the number of extra transport equations which must be solved to obtain R_{ij} . Also *one equation models* exist: they are very cheap in terms of computational costs, but exhibit relevant problems where convection and diffusion cause significant

differences between production and destruction of turbulence.

Finally it must be noted that not all the RANS models are based on the Boussinesq hypothesis: there are in fact the *Reynolds stress models* (RSM), which use seven additional equations to provide an approximation for all the six independent components of the Reynolds stress tensor, without involving the turbulent viscosity and thus preserving all the information about the anisotropy of turbulence.

In the next sections the models adopted in the performed computations will be presented.

2.4.1 Standard $k-\varepsilon$ model

Assuming that for high Reynolds numbers the energy transfer rate remains almost the same across the whole energy cascade, it is possible to use the turbulent kinetic energy k and the turbulence dissipation rate ε, whose dimensions are respectively m^2/s^2 and m^2/s^3, to obtain the characteristic velocity u_0 and length l_0 of the large scale eddies[4]:

$$u_0 = k^{\frac{1}{2}} \tag{2.46}$$

$$l_0 = \frac{k^{\frac{3}{2}}}{\varepsilon} \tag{2.47}$$

Applying dimensional analysis leads to the following equation for turbulent viscosity:

$$\mu_t = C\rho u_0 l_0 = \rho C_\mu \frac{k^2}{\varepsilon} \tag{2.48}$$

with C_μ dimensionless constant. Two transport equations to determine k and ε are now needed [5]:

$$\frac{\partial(\rho k)}{\partial t} + \frac{\partial}{\partial x_i}(\rho k u_i) = \frac{\partial}{\partial x_j}\left[\left(\mu + \frac{\mu_t}{\sigma_k}\right)\frac{\partial k}{\partial x_j}\right] + 2\mu_t s_{ij} s_{ij} - \rho\varepsilon \tag{2.49}$$

[4]This assumption is not valid for low-Reynolds-number fluxes.

[5]For the sake of simplicity the mean velocity components will from now on be indicated with lower case letters.

$$\frac{\partial(\rho\varepsilon)}{\partial t}+\frac{\partial}{\partial x_i}(\rho\varepsilon u_i)=\frac{\partial}{\partial x_j}\left[\left(\mu+\frac{\mu_t}{\sigma_\varepsilon}\right)\frac{\partial\varepsilon}{\partial x_j}\right]+C_{1\varepsilon}\frac{\varepsilon}{k}2\mu_t s_{ij}s_{ij}-C_{2\varepsilon}\rho\frac{\varepsilon^2}{k} \quad (2.50)$$

where $C_\mu = 0.09, \sigma_k = 1, \sigma_\varepsilon = 1.3, C_{1\varepsilon} = 1.44, C_{2\varepsilon} = 1.92$ are adjustable constants which derive from experimental analysis, and:

$$s_{ij}=\left(\frac{\partial u_i}{\partial x_j}+\frac{\partial u_j}{\partial x_i}\right) \quad (2.51)$$

The meaning of single terms of these equations is the following:

Rate of change of k or ε	+	Transport of k or ε by convection	=	Transport of k or ε by diffusion	+	Rate of production of k or ε	-	Rate of destruction of k or ε

It can be observed that production and destruction of turbulent kinetic energy are strictly linked: production of ε is large if production of k is large. There is therefore an equilibrium between production and dissipation of turbulence.

The standard $k-\varepsilon$ model is the most widely validated turbulence model and as a consequence of its robustness, economy and reasonable accuracy over a wide range of turbulent flows it has become the most used model in practical engineering applications. This model has however some disadvantages, in particular -like all other eddy viscosity models- its performances are quite poor in certain circumstances, such as flows characterized by anisotropy of normal Reynolds stresses, i.e. it is not possible to predict secondary flows in non circular ducts.

2.4.2 Menter's SST $k-\omega$ model

Since the SST $k-\omega$ model proposed by Menter is an improvement of Wilcox's $k-\omega$ model, the latter will first be explained and then the SST version will be derived.

While in the $k-\varepsilon$ model the length-scale-determining quantity was the rate of dissipation of turbulent kinetic energy ε, the turbulence frequency

$\omega = \varepsilon/k$ is now used instead. The turbulent viscosity is then defined as:

$$\mu_t = \alpha^* \rho \frac{k}{\omega} \tag{2.52}$$

where α^* is a damping function which ensures low-Reynolds-number correction. k and ω are calculated by means of the two following transport equations:

$$\frac{\partial(\rho k)}{\partial t} + \frac{\partial}{\partial x_i}(\rho k u_i) = \frac{\partial}{\partial x_j}\left[\left(\mu + \frac{\mu_t}{\sigma_k}\right)\frac{\partial k}{\partial x_j}\right] + 2\mu_t s_{ij} s_{ij} - \beta^* \rho k \omega \tag{2.53}$$

$$\frac{\partial(\rho \omega)}{\partial t} + \frac{\partial}{\partial x_i}(\rho \omega u_i) = \frac{\partial}{\partial x_j}\left[\left(\mu + \frac{\mu_t}{\sigma_\omega}\right)\frac{\partial \omega}{\partial x_j}\right] + 2\alpha\frac{\omega}{k}\mu_t s_{ij} s_{ij} - \beta \rho \omega^2 \tag{2.54}$$

The meaning of the single terms of the equation is exactly the same of those of the $k-\varepsilon$ model. The Reynolds stresses can then be calculated with the Boussinesq hypothesis:

$$R_{ij} = -\rho\overline{u'_i u'_j} = \mu_t\left(\frac{\partial U_i}{\partial x_j} + \frac{\partial U_j}{\partial x_i}\right) - \frac{2}{3}\rho k \delta_{ij} \tag{2.55}$$

The main advantage of the $k-\omega$ model on the $k-\varepsilon$ model is that it does not require the use of wall- or damping functions in the low-Reynolds-number near-wall regions. However, the $k-\omega$ model has the disadvantage of a strong dependency of the results on the value of ω in a free stream, which must be set as boundary condition, while the $k-\varepsilon$ model is much less sensitive to it.

These considerations led to the SST $k-\omega$ model proposed by Menter (1992), which is an hybrid of the two models: the standard $k-\varepsilon$ is used in the fully turbulent region far from the wall, and is then converted in a $k-\omega$ in the near-wall region. The two transport equations for k and ω are derived from the equations for k and ε , by substituting $\varepsilon = k\omega$:

$$\frac{\partial(\rho k)}{\partial t} + \frac{\partial}{\partial x_i}(\rho k u_i) = \frac{\partial}{\partial x_j}\left[\left(\mu + \frac{\mu_t}{\sigma_k}\right)\frac{\partial k}{\partial x_j}\right] + P_k - \beta^* \rho k \omega \tag{2.56}$$

$$\frac{\partial(\rho \omega)}{\partial t} + \frac{\partial}{\partial x_i}(\rho \omega u_i) = \frac{\partial}{\partial x_j}\left[\left(\mu + \frac{\mu_t}{\sigma_\omega}\right)\frac{\partial \omega}{\partial x_j}\right] + P_\omega - \beta \rho \omega^2 + D_\omega \tag{2.57}$$

The meaning of the terms in equation 2.57 is:

Rate of change of k or ω	+	Transport of k or ω by convection	=	Transport of k or ω by diffusion	+	Rate of production of k or ω	-	Rate of destruction of k or ω	-	Cross diffusion

These equations are quite similar to those of the original $k-\omega$ model: the only differences are the form of the production terms for k and ω and the appearance of an extra source term D_ω on the right hand side, which represents the cross diffusion and arises from the substitution of $\varepsilon = k\omega$. The production terms are:

$$P_k = min\left(2\mu_t s_{ij} s_{ij},\ 10\rho\beta^* k\omega\right) \tag{2.58}$$

$$P_\omega = \frac{\alpha}{\nu_t} P_k \tag{2.59}$$

This ensures that the production of turbulence is limited to prevent the build-up of turbulence in stagnation regions. Also the turbulent viscosity is limited:

$$\mu_t = \frac{\rho k}{\omega} \frac{1}{\max\left(\frac{1}{\alpha^*}, \frac{2F_2\ \sqrt{s_{ij}s_{ij}}}{a_1\omega}\right)} \tag{2.60}$$

to give improved performance in flows with adverse pressure gradients and in wake regions. Finally the cross diffusion term is:

$$D_\omega = 2\left(1-F_1\right)\frac{\rho}{\sigma_{\omega 2}}\ \frac{1}{\omega}\frac{\partial k}{\partial x_j}\frac{\partial \omega}{\partial x_j} \tag{2.61}$$

Many coefficients appear in the equations: $\beta^* = 0.09, \sigma_{\omega 2} = 1.168$ are constant, while $\sigma_k, \sigma_\omega, \alpha, \beta$ are made variable by means of the blending functions:

$$F_1, F_2 = f\left(\frac{\sqrt{k}}{\omega}, y, Re_y\right) \tag{2.62}$$

which ensure a smooth transition between the $k-\varepsilon$ and the $k-\omega$ model and thus numerical stability (y is the distance from the wall). Finally α^* is a

damping function which provides a low-Reynolds correction damping out the turbulent viscosity. In spite of the improved performances in the treatment of near-wall regions, the $k-\omega$ model has -as all eddy viscosity models- the same weaknesses of the $k-\varepsilon$ in case of anisotropy of the normal Reynolds stresses.

2.4.3 Menter's SAS model

The SAS model is presented as an advanced URANS model which can produce spectral content for unsteady flows. The $k-\varepsilon$ and $k-\omega$ models use the exact equation for the turbulent kinetic energy k as a starting point, while a model is used to determine ε and ω: this because the exact equations for these terms, although available, contain complex correlations which are difficult to evaluate. Consequently the ε and ω equations are modelled in analogy with the k equation using dimensional and intuitive arguments. Such an approach has however several disadvantages, because some important terms and physical effects can be missed in the derivation.

A different approach was proposed by Rotta (1968), who formulated an exact equation for kL, where k is the turbulent kinetic energy and L is an integral length scale of turbulence. The distinguishing factor of this model was the appearance of a length scale in the kL source terms, that allows the determination of a turbulence integral length scale L which -unlike the other two-equation models- is independent from the shear layer thickness and avoids the damping of the resolved scales.

The main disadvantage of this model is that the source term for L involves a third derivative of the velocity, which is very problematic because it is complex to be treated numerically and also prevents the logarithmic law to be satisfied.

In recent years Menter and Egorov [9][10] showed that instead of the third derivative term it is more correct to keep the second derivative: this ensures that the logarithmic layer equations are satisfied and furthermore it allows the model to adjust to resolved turbulent structures, without dissipating them. It means that under certain conditions the model automatically balances the

contribution of modelled and resolved parts of the turbulent stresses and smoothly changes from an LES to a steady RANS model and vice versa.

Menter and Egorov derived their KSKL (*K-Square root KL*) model from Rotta's $k - kL$ model and then transformed it to other variables in order to introduce it into existing two-equation models: the traditional SST $k-\omega$ model is thus converted into the SAS model by means of an additional source term Q_{SAS}.

$$\frac{\partial(\rho k)}{\partial t} + \frac{\partial}{\partial x_i}(\rho k u_i) = \frac{\partial}{\partial x_j}\left[\left(\mu + \frac{\mu_t}{\sigma_k}\right)\frac{\partial k}{\partial x_j}\right] + P_k - c_\mu \rho k \omega \tag{2.63}$$

$$\frac{\partial(\rho\omega)}{\partial t} + \frac{\partial}{\partial x_i}(\rho\omega u_i) = \frac{\partial}{\partial x_j}\left[\left(\mu + \frac{\mu_t}{\sigma_\omega}\right)\frac{\partial \omega}{\partial x_j}\right] + P_\omega - \beta\rho\omega^2 + D_\omega + Q_{SAS} \tag{2.64}$$

The transport equations are exactly the same of the $k-\omega$ model except for the presence of the term Q_{SAS} :

$$Q_{SAS} = \max\left[\rho\eta_2\kappa S^2\left(\frac{L}{L_{vk}}\right)^2 + \right. \\ \left. - C\frac{2\rho k}{\sigma_\varphi}\max\left(\frac{1}{\omega^2}\frac{\partial\omega}{\partial x_j}\frac{\partial\omega}{\partial x_j}, \frac{1}{k^2}\frac{\partial k}{\partial x_j}\frac{\partial k}{\partial x_j}\right), 0\right] \tag{2.65}$$

The model constants are $\eta_2 = 3.51$, $C = 2$, $\sigma_\varphi = 2/3$, while $\kappa = 0.41$ is the von Karman constant. The activation of the SAS functionality is due to the ratio L/L_{vk}, where L is the length scale of the modelled turbulence and L_{vk} is the von Karman length scale, by means of which the second derivative of velocity- that appears in Rotta's equation- is introduced in the ω equation:

$$L = \frac{\sqrt{k}}{c_\mu^{1/4}\omega} \tag{2.66}$$

$$L_{vk} = \frac{\kappa S}{|U''|} \tag{2.67}$$

The ratio L/L_{vk} is a measure of the local flow length scale and in unsteady situations it becomes much more important than the other terms, thus leading to the activation of the source term and hence to a reduction of the turbulent

viscosity, allowing therefore an adjustment of the turbulence length scale to the local flow inhomogeneities. Finally, the terms S and $|U''|$ are:

$$S = \sqrt{2S_{ij}S_{ij}},\ with\ S_{ij} = \frac{1}{2}\left[\frac{\partial u_i}{\partial x_j} + \frac{\partial u_j}{\partial x_i}\right] \tag{2.68}$$

$$\left|U''\right| = \sqrt{\frac{\partial^2 u_i}{\partial x_k^2} + \frac{\partial^2 u_i}{\partial x_j^2}} \tag{2.69}$$

They are respectively the scalar invariant of the strain rate tensor and the magnitude of the velocity laplacian and represent the first and the second velocity derivative. In the SAS model a high wave number damping is also provided, by means of a constraint on the value of the von Karman's length scale:

$$L_{vk} = max\left(\frac{\kappa S}{|U''|}, C_s\sqrt{\frac{\eta_2\kappa}{(\beta/c_\mu) - \alpha}} \cdot \Delta\right) \tag{2.70}$$

$$\Delta = V^{\frac{1}{3}} \tag{2.71}$$

where η_2, β, α are constants and V is the cell volume. This kind of damping is necessary because the von Karman length adjusts to the smallest scales and thereby produces a turbulent viscosity small enough to allow the formation of even smaller eddies until the grid resolution is reached. At this point no smaller eddies can form, however the model, if no cut-off limit is implemented, provides a turbulent viscosity that allows further formation of smaller scales. As this is not possible due to the resolution limit, the energy accumulates at the high wave number limit. It is therefore necessary to introduce a constraint for L_{vk} which ensures that scales that are smaller than the grid resolution are damped out.

2.4.4 Non-linear $k - \varepsilon$ model

The most important disadvantage of the models that are based on the Boussinesq hypothesis (the so called *eddy viscosity models*) is that they cannot capture anisotropy of the Reynolds normal stresses, and consequently they are not able to predict secondary flows.

As mentioned above, a different approach to the problem of turbulence modelling is the *Reynolds stress model* (RSM), in which a transport equation for every independent component of the Reynolds stress tensor is written, thus leading to an R_{ij} term which is effectively a tensor. This ensures that the information about anisotropy is conserved, but several other problems arise. First of all many unknown turbulence processes, such as pressure-strain correlations, need to be modelled; second, seven extra transport equations need to be introduced: six for the independent Reynolds stresses and one for the turbulent kinetic energy dissipation. It means that the computational cost significantly increases compared with two-equations models. Also, the mathematical character of the turbulence model is not anymore of viscous type, with possible limitations on the stability of the computations

Rodi [15] made a first attempt to improve the RSM method: he observed that the convection and diffusion terms of the transport equations can be neglected (*weak equilibrium assumption*), thus leading to a set of algebraic equations instead of differential equations. It is the so called *Algebraic Reynolds Stress Model* (ARSM): computational costs are sensibly reduced while the results -in presence of stress anisotropy- are better than those of the eddy viscosity models. The ARSM equation is:

$$\frac{\overline{u_i' u_j'}}{k}\left(P_k - \varepsilon\right) = \mathcal{P}_{ij} + \mathcal{R}_{ij} - \frac{2}{3}\varepsilon\delta_{ij} \tag{2.72}$$

where P_k is the rate of production of turbulent kinetic energy, $\mathcal{P}_{ij}$ is the Reynolds stresses production and $\mathcal{R}_{ij}$ is the pressure rate-of-strain tensor. Furthermore, the term $\overline{u_i' u_j'}/k$ is equivalent to the normalized Reynolds stress tensor anisotropy b_{ij}, in fact:

$$b_{ij} = \frac{1}{2k}\left(\overline{u_i' u_j'} - \frac{2}{3}\delta_{ij}\right) \Rightarrow \frac{\overline{u_i' u_j'}}{k} = 2b_{ij} + \frac{2}{3}\delta_{ij} \tag{2.73}$$

The main disadvantage is that the ARSM involves the resolution of a system of strongly coupled implicit algebraic equations, which sometimes leads to numerical instability and convergence difficulty. The efforts to overcome

these problems led to the so called *Explicit Algebraic Reynolds Stress Models* (EARSM).

In order to find an explicit relation for the anisotropy b_{ij}, Pope (1975) [13] introduced the following expression:

$$b_{ij} = B_{ij}\left(\widehat{\mathbf{S}}, \widehat{\mathbf{\Omega}}\right) = \sum_{n=1}^{10} G^{(n)} \widehat{\mathcal{T}}_{ij}^{n} \tag{2.74}$$

which represents the most general possible relationship between the Reynolds stresses and strain.

$\widehat{\mathbf{S}}$ and $\widehat{\mathbf{\Omega}}$ are the normalized mean rate-of-strain and rotation tensors, $\widehat{S}_{ij} = \frac{k}{\varepsilon} S_{ij}$; $\widehat{\Omega}_{ij} = \frac{k}{\varepsilon}\Omega_{ij}$.

$\widehat{\mathcal{T}}^{(n)}$are non dimensional symmetric deviatoric tensors while $G^{(n)}$ are coefficients which depend upon the five invariants $\widehat{S}_{ii}^2,\ \widehat{\Omega}_{ii}^2, \widehat{S}_{ii}^3,\ \widehat{\Omega}_{ij}^2\widehat{S}_{ji},\ \widehat{\Omega}_{ij}^2\widehat{S}_{ji}^2$.

Since the ten tensors $\widehat{\mathcal{T}}^{(n)}$ form an integrity basis, every second order tensor formed from $\widehat{\mathbf{S}}$ and $\widehat{\mathbf{\Omega}}$ can be expressed as a linear combination of them; the finite number of independent tensors and invariants is a consequence of the Cayley-Hamilton theorem of matrix algebra.

Assuming $G^{(1)} = -C_\mu$ and $G^{(n)} = 0$ for $n > 1$ leads to the linear $k - \varepsilon$ turbulent viscosity formula, while a non trivial specification of $G^{(n)}$ for $n > 1$ yields a non-linear viscosity model, it means an explicit formula for $\overline{u'_i u'_j}$ that is non-linear in the mean velocity gradients.

Since these models are based on explicit equations, they have been classified as EARSM; furthermore, according to the appearance of non-linear terms, they are also known as *non-linear eddy viscosity models*: $\overline{u'_i u'_j}$ depends now not only upon S -as in the Boussinesq hypothesis- but also on higher order terms, such as S^2. It has also been demonstrated that to obtain sensitivity to normal stress anisotropy and mean streamline curvature a cubic stress-strain relationship is sufficient. This leads to the following general

relation for the Reynolds stresses:

$$
\begin{aligned}
-\rho\overline{u'_i u'_j} = &-\frac{2}{3}\rho k\delta_{ij} + \mu_t S_{ij} - C_1\mu_t\frac{k}{\varepsilon}\left[S_{ik}S_{kj} - \frac{1}{3}\delta_{ij}S_{kl}S_{kl}\right] + \\
&- C_2\mu_t\frac{k}{\varepsilon}\left[\Omega_{ik}S_{kj} + \Omega_{jk}S_{ki}\right] - C_3\mu_t\frac{k}{\varepsilon}\left[\Omega_{ik}\Omega_{jk} - \frac{1}{3}\delta_{ij}\Omega_{kl}\Omega_{kl}\right] + \\
&- C_4\mu_t\frac{k^2}{\varepsilon^2}\left[\Omega_{lj}S_{ki} + \Omega_{li}S_{kj}\right]S_{kl} + \\
&- C_5\mu_t\frac{k^2}{\varepsilon^2}\left[\Omega_{il}\Omega_{lm}S_{mj} + \Omega_{mj}\Omega_{lm}S_{il} - \frac{2}{3}S_{lm}\Omega_{mn}\Omega_{nl}\delta_{ij}\right] + \\
&- C_6\mu_t\frac{k^2}{\varepsilon^2}\left[S_{kl}S_{kl}S_{ij}\right] - C_7\mu_t\frac{k^2}{\varepsilon^2}\left[\Omega_{kl}\Omega_{kl}S_{ij}\right] \qquad (2.75)
\end{aligned}
$$

In the performed simulations a third order model with eddy viscosity damping has been adopted, which was implemented in ANSYS FLUENT by means of an user defined function (UDF), see [11].

This model is based on a standard $k-\varepsilon$ model which has been improved adding five source terms derived from equation 2.75 in each momentum equation and in the turbulence production and dissipation equations, while a damping function f_μ proposed by Wilcox [21] has been introduced in the definition of the eddy viscosity, in order to ensure a good accuracy in low-Reynolds-number regions:

$$\mu_t = C_\mu\rho f_\mu\frac{k^2}{\varepsilon} \qquad (2.76)$$

$$f_\mu = \frac{0.024 + Re_t/6}{1 + Re_t/6} \qquad (2.77)$$

where Re_t is a Reynolds number based on turbulent quantities.

The coefficients $C_1 \dots C_7$ are chosen in order to ensure the realizability of the model, i.e. the diagonal elements of the Reynolds stress tensor must be positive and the Schwarz inequality must be verified[6]

[6]The two conditions are $\overline{u'_\alpha u'_\alpha} > 0$ and $\overline{u'_i u'_j}^2 > \overline{u_i^2}\cdot\overline{u_j^2}$ so that unphysical results are avoided.

2.5 LES models

As mentioned above, also the filtered LES Navier-Stokes equations need to be closed: a suitable model for the subgrid scale stresses τ_{ij} must therefore be found. In ANSYS FLUENT these stresses are modelled -as in the RANS approach- by means of the Boussinesq hypothesis:

$$\tau_{ij} = -\rho\overline{u_i u_j} - \rho\overline{u}_i\overline{u}_j = -\mu_{SGS}\left(\frac{\partial\overline{u}_i}{\partial x_j} + \frac{\partial\overline{u}_j}{\partial x_i}\right) + \frac{1}{3}\tau_{kk}\delta_{ij} \tag{2.78}$$

where the constant of proportionality between stress and strain is the dynamic subgrid scale (SGS) viscosity μ_{SGS}, while the term $1/3\tau_{kk}\delta_{ij}$ is not modelled but added to the filtered static pressure term. At this point a model for μ_{SGS} must be provided.

2.5.1 Smagorinsky-Lilly model

This is the simplest subgrid scale model, and it builds on Prandtl's mixing length model[7]:

$$\mu_{SGS} = \rho L_{SGS}^2 \left|\overline{S}\right| \tag{2.79}$$

$$\left|\overline{S}\right| = \sqrt{2\overline{S}_{ij}\overline{S}_{ij}} \tag{2.80}$$

L_{SGS} is the mixing length for the subgrid scales and its size is determined by the details of the filtering function, i.e. the filter cutoff width Δ. In ANSYS FLUENT L_{SGS} is computed as:

$$L_{SGS} = min\left(\kappa d, C_s\Delta\right) \tag{2.81}$$

$$\Delta = V^{1/3} \tag{2.82}$$

where κ is the von Karman constant and d is the distance to the closest wall, C_s is the Smagorinsky constant and V is the generic cell volume.

[7]In case of simple two-dimensional flows it can be assumed that the only significant stresses are $\tau_{xy} = \tau_{yx} = -\rho\overline{u'v'}$ and the only significant velocity gradient is $\partial U/\partial y$. The Reynolds stresses can therefore be described with the relation: $\tau_{xy} = \rho l_m^2 \left|\frac{\partial U}{\partial y}\right| \frac{\partial U}{\partial y}$, where l_m is the so called mixing length, which varies case-by-case.

The main shortcoming of this model lays in the fact that the constant C_s is not universal: Lilly derived a value of 0.17 for isotropic homogeneous turbulence in the inertial subrange, nonetheless a value of 0.1 has been found to yield the best results for a wide range of flows. This means that the behaviour of the small eddies is not as universal as it was conjectured at first and that a correct LES modelling might require case-by-case adjustment of C_s or a more sophisticated approach.

2.5.2 Dynamic SGS model

Germano (1991) proposed to compute local values of C_s by means of a dynamic procedure: its concept is to apply a second filter (called *test filter*, with $\widehat{\Delta} > 2\Delta$) to the filtered equations of motion. The difference between the two resolved fields represents the contribution of the scales whose size is comprised between the two different filter widths. When applying the test filter the SGS stress tensor can be expressed as:

$$T_{ij} = \rho \left(\widehat{\overline{u_i u_j}} - \widehat{\overline{u}}_i \widehat{\overline{u}}_j \right) \tag{2.83}$$

Both T_{ij} and τ_{ij} are modelled with the Smagorinsky model, assuming that C_s is the same:

$$\tau_{ij} = -2\rho C_s^2 \Delta^2 \left| \overline{S} \right| \overline{S}_{ij} \tag{2.84}$$

$$T_{ij} = -2\rho C_s^2 \widehat{\Delta}^2 \left| \widehat{\overline{S}} \right| \widehat{\overline{S}}_{ij} \tag{2.85}$$

According to the Germano identity, the difference between the two SGS stress tensors can be written as:

$$L_{ij} - \frac{1}{3} L_{kk} \delta_{ij} = T_{ij} - \widehat{\tau}_{ij} = \rho \left(\widehat{\overline{u}_i \overline{u}_j} - \widehat{\overline{u}}_i \widehat{\overline{u}}_j \right) \tag{2.86}$$

This yields:

$$\begin{aligned} L_{ij} - \frac{1}{3} L_{kk} \delta_{ij} = T_{ij} - \widehat{\tau}_{ij} = \\ = C_S^2 \left(-2\rho \widehat{\Delta}^2 \left| \widehat{\overline{S}} \right| \widehat{\overline{S}}_{ij} + 2\Delta^2 \widehat{\left| \overline{S} \right| \overline{S}_{ij}} \right) = C_S^2 M_{ij} \end{aligned} \tag{2.87}$$

The value of C_S^2 can be then found by means of a least squares approach proposed by Lilly (1992):

$$C_S^2 = \frac{(L_{ij} - L_{kk}\delta_{ij}/3)\, M_{ij}}{M_{ij} M_{ij}} \tag{2.88}$$

Finally $C_S = \sqrt{C_S^2}$.

2.6 General remarks about turbulence models

It is at this point important to spend a few words to explain the criterion which lead to the adoption of the models listed above. First of all the standard $k - \varepsilon$ has been chosen as a reference URANS model; also, it is one of the most widely used models in industrial applications. Furthermore, it has also been employed in several works about the same test case of this thesis [4], [2].

The SAS model has instead been chosen because it is quite recent and it was therefore interesting to investigate its performances. In addition, since it is derived from the $k - \omega$ SST model and aims to be an hybrid between URANS and LES computations, also these two approaches have been adopted, in order to allow a comparison of the different models.

Finally, also a non linear version of the $k - \varepsilon$ model has been used, in order to investigate its improvements over the standard version of the model.

Since the y^+ values were of unity order, in all simulations a down-to-the-wall approach has been adopted. In case of $k - \omega$ SST, SAS and LES (with dynamic SGS model) the computation of the viscous sublayer does not require a particular treatment. On the other side, simulations with the standard $k-\varepsilon$ model use the one equation model of Wolfstein [1] in proximity of the walls. Finally, as mentioned above, the non linear $k - \varepsilon$ model adopts a low-Reynolds damping function proposed by Wilcox.

2.7 Effects of turbulence models on computational costs

As mentioned above, in spite of the efforts that have been taken, a universal model for turbulence seems unlikely to exist. Instead of it, many models have been proposed, which have substantial differences either in the hypotheses on which they are based or in the resolution that they ensure.

No model has so far been accepted as being superior for all classes of problems: every model has particular strengths and weaknesses and will be more suitable for a certain kind of applications. It goes without saying that turbulence models have also an important influence on the computational costs, since they require additional transport equations to be solved. Furthermore, models that ensure high resolution need necessarily the adoption of very fine grids, and this again increases the computational costs.

The models that were adopted in the performed simulations are mainly two-equations models, it means that for every time step two additional transport equations must be solved, besides the three momentum equations, the pressure-velocity coupling and the energy equation.

Among these models, the SAS requires the evaluation of an additional source term, which is essentially computed from the velocity laplacian and the first derivatives of production and dissipation rate of turbulence. These quantities are not computed by default by ANSYS FLUENT, therefore they require a further discretization procedure: the SAS model is therefore expected to need slightly more computational time then the other two-equation models. On the other hand the LES approach does not introduce additional transport equations or complex source terms, thus leading to faster calculations: the dynamic model for the SGS stresses introduces in fact only algebraic equations, which are not expensive to solve.

The non linear $k-\varepsilon$ is instead expected to be the slowest one: it requires in fact the definition of a large amount of scalars, of source terms and the calculation of derivatives which are not computed by default by FLUENT. Besides this the specific model implementation puts some limitations on the numerical solver (see paragraph 3).

Finally it must be observed that the duration of the simulation depends not only on the time needed for the computation of a single time step, but also on the number of time steps needed to obtain converged statistics. As the resolution of the model increases, the time step size decreases (in order to resolve the smallest scales of motion), thus leading to a large amount of time steps required to reach convergence.

Chapter 3

Solver

3.1 The solver ANSYS FLUENT

As already noticed, the aim of the present work is to compare the performances -in terms of accuracy and computational costs- of different turbulence models implemented in the commercial finite volume solver ANSYS FLUENT.

The results of the simulations are strictly dependent on the adopted discretization schemes, since they directly influence the numerical error; furthermore, as mentioned above, in the case of the LES approach the influence of the solver is even more important, as the filtering procedure is implicitly determined by the finite volume discretization, the numerical flux evaluation and the time integration method. It is therefore important to give a brief description of the numerical methods adopted in the solver.

The commercial CFD code FLUENT is a co-located, cell centred, unstructured finite volume solver for both compressible and incompressible flows, which also provides a large variety of models for many physical applications, such as heat transfer, combustion and multi-phase flows.

In the next sections the main features of the solver will be described, such as the spatial and temporal discretization, the available numerical schemes and the pressure-velocity coupling; in particular, the attention will be focused to numerical methods adopted in the performed computations.

3.2 Flow solver

In ANSYS FLUENT, two different solvers are available: the pressure based and the density based solver. While the pressure-based approach was developed for low-Mach-number incompressible flows, the density based solver is instead well suited for high-speed compressible flows.

Since in the analysed case the flow velocity is low, only the pressure based solver has been adopted. Velocity is computed from the momentum equations, while the pressure field is obtained using a *pressure-velocity coupling* algorithm which derives from a manipulation of the momentum and continuity equations.

Generally speaking, the governing equations are first discretized by means of a finite volume approach: the domain is therefore divided into discrete control volumes using a computational grid. The discrete equations are then integrated over each control volume, thus leading to a system of algebraic equations for the unknown variables. Finally, the system is linearized and solved.

3.3 Discretization of the general scalar transport equation

The discretization procedure can be clearly explained by considering the unsteady transport equation for a generic scalar quantity φ. For a generic control volume V, this equation can be written as follows:

$$\frac{\partial}{\partial t}\int_V \rho_0\varphi dV + \int_{\partial V}\left(\rho_0\varphi\vec{u} - \Gamma_\varphi\vec{\nabla}\varphi\right)\cdot\vec{n}dA = \int_V S_\varphi dV \tag{3.1}$$

Where ρ_0 is the constant density, $\vec{u}$ a divergence free velocity field, Γ_φ the diffusion coefficient for φ and S_φ a source term for φ.

In order to obtain a numerical solution for the problem, several approximations must be introduced. These include the computation of surface and volume integrals, the evaluation of the fluxes on the faces of the volumes and the computation of the variable gradient from its value in the cell centres.

Since the integral on the volume boundary ∂V can be written as the sum of the integrals on the volume faces, the equation -according to the mean value theorem- can be rewritten as follows:

$$\frac{\partial}{\partial t}\ (\overline{\rho_0\varphi}V) + \sum_{f=1}^{N_{faces}}\left[\widetilde{\left(\rho_0\varphi\vec{u} - \Gamma_\varphi\vec{\nabla}\varphi\right)}\cdot\vec{n}\right]_f A_f = \overline{S_\varphi}V \tag{3.2}$$

Where V is the volume of the cell and A_f the area of the generic cell-face f; the overbar refers to a volume average, the tilde to an area average and the subscript f to the face f. Introducing a second order approximation, it is possible to replace the volume averaged quantity in the time derivative with

the local value in the cell centre (denoted by the subscript c), yielding:

$$\frac{\partial}{\partial t}\left[\left(\rho_0\varphi\right)_c V\right] + \sum_{f=1}^{N_{faces}} \left[\left(\rho_0\varphi\widetilde{\vec{u} - \Gamma_\varphi\vec{\nabla}\varphi}\right)\cdot\vec{n}\right]_f A_f = \overline{S_\varphi}V \tag{3.3}$$

Furthermore, assuming the cell faces to be flat, equation 3.3 can be rewritten as:

$$\frac{\partial}{\partial t}\left[\left(\rho_0\varphi\right)_c V\right] + \sum_{f=1}^{N_{faces}} \left(\rho_0\varphi\widetilde{\vec{u} - \Gamma_\varphi\vec{\nabla}\varphi}\right)_f \cdot\vec{n}_f A_f = \overline{S_\varphi}V \tag{3.4}$$

since the unity vector $\vec{n}_f$ is now constant on every cell face.

It must be noticed that if the faces are not flat, this operation introduces a second order approximation, which is however consistent with the approximation introduced before.

Finally, like in the discretization of the volume average, the face averages which appear in the sum can be approximated with the value in centre of the face, which is again a second order approximation. This leads to the following equation, which represents the discretized form of the general scalar transport equation implemented in FLUENT:

$$\frac{\partial}{\partial t}\left(\rho_0\varphi\right)_c V + \sum_{f=1}^{N_{faces}} \left(\rho_0\varphi\vec{u} - \Gamma_\varphi\vec{\nabla}\varphi\right)_f \cdot\vec{n}_f A_f = \overline{S_\varphi}V \tag{3.5}$$

For the sake of clarity the subscript f now implies that the quantities have been evaluated in the centre of the cell face. Furthermore, since the cell volume has been assumed not to be time dependent, V has been taken out from the time derivative.

In the next paragraphs the discretization of the convection and the diffusion term will be explained, but first a brief description of the numerical schemes adopted for the reconstruction of gradients will be given.

3.4 Evaluation of gradients

Gradients need to be computed in order to allow the evaluation of scalar quantities at the cell faces and the discretization of convection and diffusion terms: for this purpose, FLUENT provides three different methods. For all the computations the *least squares cell-based method* has been adopted, which assumes a linear variation of the solution between the cell centres sharing a face. With regard to figure 3.1 this can be written as follows:

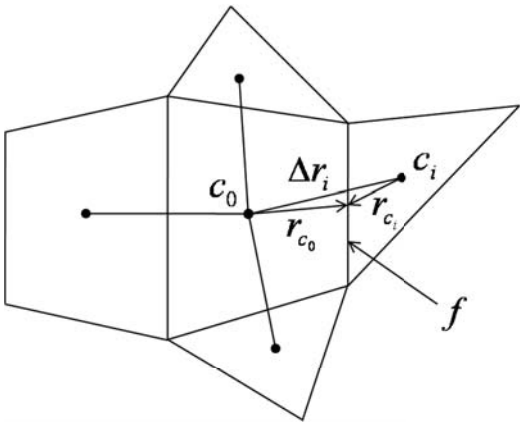

Figure 3.1: Gradients evaluation.

$$\vec{\nabla}\varphi\Big|_{c_0} \cdot \overrightarrow{\Delta r_i} = (\varphi_{ci} - \varphi_{c0}) \tag{3.6}$$

Where c_0 is the centre of the cell in which the gradient is computed, c_i is the centre of the generic neighbour cell and $\overrightarrow{\Delta r_i}$ is the distance between c_0 and c_i. A similar equation can be written for every neighbouring cell, yielding the following over-determined system:

$$[J]\ \vec{\nabla}\varphi\Big|_{c_0} = \Delta\varphi \tag{3.7}$$

Where $[J]$ is the coefficient matrix, which depends only on the geometry and the unknowns are the three components of the gradient in c_0. The least-squares solution of the problem is obtained by means of a Gram-Schmidt decomposition of the coefficient matrix, which yields a matrix of weights for

each cell: three components weights $(W_{i0}^x, W_{i0}^y, W_{i0}^z)$ are produced for each face i of the cell with centre c_0. The gradient at the cell centre can therefore be obtained as follows:

$$\left.\frac{\partial\varphi}{\partial x}\right|_{c_0} = \sum_{1=1}^{N_{faces}} W_{i0}^x \left(\varphi_{c_i} - \varphi_{c_0}\right) \tag{3.8}$$

$$\left.\frac{\partial\varphi}{\partial y}\right|_{c_0} = \sum_{1=1}^{N_{faces}} W_{i0}^y \left(\varphi_{c_i} - \varphi_{c_0}\right) \tag{3.9}$$

$$\left.\frac{\partial\varphi}{\partial z}\right|_{c_0} = \sum_{1=1}^{N_{faces}} W_{i0}^z \left(\varphi_{c_i} - \varphi_{c_0}\right) \tag{3.10}$$

The other two available methods for the computation of gradients are the *Green Gauss cell based* and the *Green Gauss node based*; however, as they are not used in the present thesis, their description is omitted: the interested reader may refer to [1].

3.5 Discretization of the convective term

The computation of the convective term requires the value of φ in the centre of the cell face: this has to be reconstructed from the values stored in the cell centres. Several methods are available: with the *first order upwind scheme*, the face value is assumed to be equal to the value in the centre of the upwind cell, relative to the mass flux through the face. With regard to figure 3.1 The convective term is therefore discretized as follows:

$$\left(\rho_0\varphi\vec{u}\right)_f \cdot \vec{n}_f = \max\left(\rho_0\vec{u}\cdot\vec{n}_f, 0\right)\varphi_{c_0} + \min\left(\rho_0\vec{u}\cdot\vec{n}_f, 0\right)\varphi_{c_i} \tag{3.11}$$

By means of a Taylor series expansion it can be shown that this introduces a first order approximation of the face value and the truncation error acts as a further dissipation term.

In the *second order upwind scheme* the gradients in the cell centres are used to improve the approximation of the face value. The convective term is

therefore computed as:

$$(\rho_0\varphi\vec{u})_f \cdot \vec{n}_f = \max(\rho_0\vec{u}\cdot\vec{n}_f, 0)\left(\varphi_{c_0} + \overrightarrow{r_{c_0}}\cdot\vec{\nabla}\varphi\Big|_{c_0}\right) + \\ + \min(\rho_0\vec{u}\cdot\vec{n}_f, 0)\left(\varphi_{c_i} + \overrightarrow{r_{c_i}}\cdot\vec{\nabla}\varphi\Big|_{c_i}\right) \tag{3.12}$$

The gradient is computed as explained in the previous paragraph. In this case, it can be shown that a second order approximation is introduced, the truncation error still acting as an additional dissipation.

In order to avoid spurious oscillations, several different gradient limiters are implemented in FLUENT, which avoid that the linearly reconstructed field variable exceeds the minimum and the maximum values in the neighbouring cells. Due to its second order accuracy, this scheme has been adopted in all the performed URANS computations.

A further second order scheme is the *central-differencing scheme*, which has been introduced in FLUENT purposely for LES simulations. The convective term becomes:

$$(\rho_0\varphi\vec{u})_f \cdot \vec{n}_f = \frac{1}{2}(\rho_0\vec{u}\cdot\vec{n}_f)\left[\left(\varphi_{c_0} + \overrightarrow{r_{c_0}}\cdot\vec{\nabla}\varphi\Big|_{c_0}\right) + \right. \\ \left. + \left(\varphi_{c_i} + \overrightarrow{r_{c_i}}\cdot\vec{\nabla}\varphi\Big|_{c_i}\right)\right] \tag{3.13}$$

and its computational stencil is independent from the velocity field. This scheme should be particularly indicated for LES, since it does not alter the energy content of the flow[1]; it can however introduce oscillations of the solution, which may cause numerical instability, due to the low introduced diffusivity and to the low dissipative nature of the LES subgrid scales. To avoid stability problems, it is possible to adopt a deferred approach, in which the face value is calculated adopting simultaneously the upwind and the central differencing schemes.

Finally the *bounded central differencing scheme* is implemented in FLUENT. This is also a second order scheme, which does not exhibit the problems

[1]Except for the gradient part.

of the central differencing scheme mentioned above, and has therefore been adopted in all the performed LES simulations. Due to the limited available information, it is not possible to give an accurate description of the scheme: it essentially consists of a pure central differencing, a blended scheme of the central differencing and the second order upwind scheme, and the first order upwind scheme. The first order upwind scheme is adopted only if the *convection boundedness criterion is violated*, that is when new minima or maxima are introduced in the solution.

3.6 Discretization of the diffusion term

The discretization of the diffusion term employs a second order accurate central differencing scheme. It requires the reconstruction of the gradient at the face centres from the values stored in the centres of the neighbouring cells. The discretized diffusion term is written as sum of two terms:

$$\left(\Gamma_\varphi \vec{\nabla}\varphi\right)_f \cdot \vec{n}_f = (\Gamma_\varphi)_f \left[\frac{\varphi_{c_i} - \varphi_{c_0}}{\vec{n}_f \cdot \overrightarrow{\Delta r_i}} + \left\langle \vec{\nabla}\varphi \right\rangle_f \cdot \left(\vec{n_f} - \frac{\overrightarrow{\Delta r_i}}{\vec{n}_f \cdot \overrightarrow{\Delta r_i}}\right)\right] \tag{3.14}$$

where

$$\left\langle \vec{\nabla}\varphi \right\rangle_f = \frac{\vec{\nabla}\varphi\Big|_{c_i} + \vec{\nabla}\varphi\Big|_{c_0}}{2} \tag{3.15}$$

The component of the gradient along the line connecting the cell centres is reconstructed according to the classical finite differences approach; the remaining part is instead computed as the average of the gradients in the adjacent cell centres. This formulation avoids the checkerboard effect, which is due to the exclusive use of $\left\langle \vec{\nabla}\varphi \right\rangle_f$ in the discretization of the diffusion term.

3.7 Temporal discretization

The final step is the discretization of the time derivative, in order to obtain a computable model. In Fluent both a first[2] and a second order scheme are implemented. Because of its higher accuracy, the latter one has been adopted in the performed simulations.

The Taylor series expansions of the quantity φ in c_0 at the time steps[3] n and $n-1$ are:

$$\varphi_{c_0}^{n} = \varphi_{c_0}^{n+1} - \Delta t \frac{\partial \varphi}{\partial t}\bigg|_{c_0}^{n+1} + \frac{\Delta t^2}{2}\frac{\partial^2 \varphi}{\partial t^2}\bigg|_{c_0}^{n+1} - \frac{\Delta t^3}{6}\frac{\partial^3 \varphi}{\partial t^3}\bigg|_{c_0}^{n+1} + O\left(\Delta t^4\right) \quad (3.16)$$

$$\varphi_{c_0}^{n-1} = \varphi_{c_0}^{n+1} - 2\Delta t \frac{\partial \varphi}{\partial t}\bigg|_{c_0}^{n+1} + 2\Delta t^2 \frac{\partial^2 \varphi}{\partial t^2}\bigg|_{c_0}^{n+1} - \frac{4\Delta t^3}{3}\frac{\partial^3 \varphi}{\partial t^3}\bigg|_{c_0}^{n+1} + O\left(\Delta t^4\right) \quad (3.17)$$

Subtracting four times equation 3.16 from equation 3.17 yields the following identity:

$$\frac{3\varphi_{c_0}^{n+1} - 4\varphi_{c_0}^{n} + \varphi_{c_0}^{n-1}}{2\Delta t} = \frac{\partial \varphi}{\partial t}\bigg|_{c_0}^{n+1} - \frac{\Delta t^2}{3}\frac{\partial^3 \varphi}{\partial t^3}\bigg|_{c_0}^{n+1} + O\left(\Delta t^3\right) \quad (3.18)$$

which can be used for a second order approximation of the time derivative in equation 3.5:

$$\frac{3\varphi_{c_0}^{n+1} - 4\varphi_{c_0}^{n} + \varphi_{c_0}^{n-1}}{2\Delta t} = -\sum_{f=1}^{N_{faces}} \left(\varphi \vec{u} - \frac{\Gamma_\varphi}{\rho_0}\vec{\nabla}\varphi\right)_f \cdot \vec{n}_f \frac{A_f}{V} + \frac{S_\varphi}{\rho_0} \quad (3.19)$$

The terms in brackets are in turn discretized by means of the schemes illustrated above, thus yielding the following reformulation:

$$\frac{3\varphi_{c_0}^{n+1} - 4\varphi_{c_0}^{n} + \varphi_{c_0}^{n-1}}{2\Delta t} = -\sum_i l_i \varphi_i^m + s \quad (3.20)$$

where the first term on the right hand side of equation 3.19 has been expressed

[2] First order Euler.

[3] The adopted convention is that the time t can be written as $t = n\Delta t$, where Δt is the discretization time step.

as the weighted sum of the value of φ in the centre of the integration cell c_0 and the adjacent cells. The sum extends over an unspecified number of cells, which depends on the scheme that has been adopted, while the coefficients l_i depend from the geometry and, possibly, from external parameters. The term s takes account of the part of the source term which can be computed independently from the values φ_i^m.

Writing equation 3.20 for every finite volume of the domain with proper initial and boundary conditions yields a closed system of equations which can be solved for the value of the variable at the following time step, φ^{n+1}.

A last issue to discuss is the choice of the time step m at which the sum on the right hand side has to be evaluated. According to equation 3.18, in which the time derivative at the time step $n+1$ is discretized, the value φ^{n+1} would be required, leading to a fully implicit method, which, for linear systems like the simplified one considered above, has the advantage of being unconditionally stable with respect to the time step.

However, in order to avoid the computational costs due to the high order terms, the *deferred correction approach* is used in Fluent: all schemes which involve higher order terms such as gradients are split into a low order and a correction term. The first one, which involves only the nearest cells, is evaluated at the time level $n+1$, and is therefore treated implicitly; the second one is instead expressed as the difference between the higher order approximation, which involves all the adjacent cells, and the low order term, and is evaluated at the time step n (and therefore treated explicitly). The equation system can then be rewritten as:

$$\varphi_{c_0}^{n+1} + \frac{2}{3}\Delta t \sum_i^{nc+1} d_i \varphi_i^{n+1} = -\frac{2}{3}\Delta t \sum_j p_j \varphi_j^{nk} + \frac{4\varphi_{c_0}^n - \varphi_{c_0}^{n-1} + 2\Delta t s}{3} \quad (3.21)$$

where unknown terms, i.e. quantities at the time level $n+1$, have been split from computable terms (those at the time levels n and $n-1$). The sum on the left hand side extends over the neighbouring cells nc in addition to the cell with centre c_0; the one on the right hand side involves instead the quantity φ_j^{nk}, which refers to the previous iteration (i.e. the k-th iteration)

performed in the computation of the $n+1$-th time step. The system can now be rewritten in a more compact form:

$$a_{c_0}\varphi_{c_0}^{n+1} + \sum_i a_i\varphi_i^{n+1} = b \tag{3.22}$$

where b includes the boundary conditions and all the computable terms, i.e. those that are available from the previous time steps or iteration. The resulting system of equation 3.22 is then resolved by means of the *Gauss-Seidel* method with an *algebraic multigrid* acceleration technique. The iterative method stops when the *scaled residual*, defined as:

$$R = \frac{\sum_{cells}\left(\left|a_{c_0}\varphi_{c_0}^{n+1} + \sum_i a_i\varphi_i^{n+1} - b\right|\right)}{\sum_{cells}\left|a_{c_0}\varphi_{c_0}^{n+1}\right|} \tag{3.23}$$

falls under a certain prefixed tolerance level.

Only the discretization and the solution of the general scalar transport equation has been discussed so far: in the following paragraph, while explaining the problem of the *pressure-velocity coupling* for incompressible flows, the previously introduced issues will be extended to the complete system of the incompressible Navier-Stokes equations. However, since in the analysed case a heat-transfer problem is involved, in addition to the set of incompressible Navier-Stokes equations also the general transport equation for the temperature will be solved.

3.8 Pressure-velocity coupling

The complete system of the incompressible and isothermal Navier-Stokes equations for a Newtonian fluid has the following integral form:

$$\frac{\partial}{\partial t}\int_V \rho_0\vec{u}dV + \int_{\partial V}\left(\rho_0\vec{u}\vec{u} + p\,[I] - \mu\vec{\nabla}\vec{u}\right)\cdot\vec{n}dA = \int_V \vec{S}dV \tag{3.24}$$

$$\int_{\partial V}\vec{u}\cdot\vec{n}dA = 0 \tag{3.25}$$

where ρ_0 is the constant density, $\vec{u}$ the velocity filed, $[I]$ the identity matrix, μ the dynamic viscosity, $\vec{n}$ the outward unity vector normal to the boundary of the domain V and S a generic momentum source term.

A first important point to remark is that the equations of the system are strongly coupled and non linear. More in detail, the discretized convective term $\rho_0\varphi\vec{u}\cdot\vec{n}$ that appeared in the general scalar transport equation analysed in the previous chapter becomes now $\rho_0\vec{u}\vec{u}\cdot\vec{n}$, since the generic variable φ is replaced by $\vec{u}$. As a consequence, the flux through the faces of the volume becomes a function of $\vec{u}$, which is also the solution variable.

The coefficients introduced in paragraph 3.5 are therefore not anymore constant and, since the low order terms -as mentioned above- are treated implicitly, the resulting system becomes non linear. Problems due to equation coupling and non linearities are faced in a way similar to that for the higher order terms in the deferred approach: coefficients are evaluated at the previous iteration and frozen to make the system linear.

The lack of an independent equation for the pressure is a further important issue, which is also strictly related to the continuity (divergence-free) constraint on the velocity field. In case of a compressible fluid, in fact, the link between pressure and density is described by the equation of state; otherwise, assuming the density to be constant, the continuity equation becomes a kinematic constraint on the velocity field and, in addition, an independent equation for the pressure is missing. As a consequence, an algorithm which provides a *pressure-velocity coupling* is needed.

In ANSYS FLUENT several different algorithms are implemented, but for the performed simulations mainly the so called *fractional-step method* (FSM) has been adopted, since it allows to minimize the computational time. The unique exception is the simulation with the non linear $k-\varepsilon$ model: in this case the iterative PISO algorithm has been chosen because the model implementation requires the property update inside an iterative loop.

With the *fractional step method* the momentum equations are iteratively solved (with the so called *inner iterations*) using a provisional pressure field: this yields a velocity field which is not divergence free. The obtained velocity field is then corrected with a gradient term, obtained from the solution of

a Poisson equation for the pressure, so that the divergence becomes zero; from this equation it is also possible to obtain the correction to update the pressure at the next time level.

Unlike the FSM, other pressure velocity coupling algorithms (such as those of the SIMPLE family), require for every time step also a cycle of so called *outer iterations*. The new pressure value obtained from the correction is in fact not directly used to compute the next time step but is instead substituted again in the momentum equations and this iterative process stops when the scaled residuals reach the tolerance level.

Since the main difference between the two approaches is the need of the outer iterations, the FSM is labelled as *non-iterative time advancement* (NITA) method, while the other algorithms are classified as *iterative time advancement* (ITA) methods. The NITA sensibly reduces the computational time, while on the other side the ITA ensures higher stability. The PISO is the only algorithm which can be used both with iterative or non iterative time advancement because, like the FSM, the splitting error is of the same order of magnitude of the time integration error and the outer iterations are therefore not necessary. However, since it requires two equations to be solved in order to yield the pressure correction, it increases the computational costs, therefore in the performed simulations, where possible, the FSM has been preferred, while the PISO has been adopted with an iterative time advancement. The FSM implemented in FLUENT is based on an approximated factorization of the system of discretized equations, which is:

$$\overbrace{\left[\frac{3\rho_0 V}{2\Delta t} I + (N - L)\right]}^{A} \vec{u}^{n+1} + G p^{n+1} = \overbrace{\frac{\rho_0 V}{2\Delta t}\left(4\vec{u}^{n} - \vec{u}^{n-1}\right) + \vec{S}_u}^{\vec{r}} \tag{3.26}$$

$$D\vec{u}^{n+1} = 0 \tag{3.27}$$

where $\vec{u}$ is the discrete solution, i.e. the components of the velocity field in the cell centres, p is the pressure in the cell centres, I the identity operator, N and L stem from the discretization of the convection and diffusion terms, G and D derive from the discretization of the gradient and divergence terms,

while $\vec{S}_u$ is the momentum source term. The equation above can be rewritten in compact form as follows:

$$\begin{bmatrix} A & G \\ D & 0 \end{bmatrix} \begin{bmatrix} \vec{u}^{n+1} \\ p^{n+1} \end{bmatrix} = \begin{bmatrix} \vec{r} \\ 0 \end{bmatrix} + \begin{bmatrix} m.b.c. \\ c.b.c. \end{bmatrix} \tag{3.28}$$

where $m.b.c$ are the momentum boundary conditions and $c.b.c$ are the continuity boundary conditions. This represents the complete system for the whole domain, which has to be resolved for $\vec{u}$ and p[4] at the time level $n+1$ starting from the values at the time steps $n-1$ and n. To solve the system, a factorization is needed. The exact LU factorization of the matrix is:

$$\begin{bmatrix} A & 0 \\ D & -DA^{-1}G \end{bmatrix} \begin{bmatrix} I & A^{-1}G \\ 0 & I \end{bmatrix} \begin{bmatrix} \vec{u}^{n+1} \\ \delta p^{n+1} \end{bmatrix} = \begin{bmatrix} \vec{r} - Gp^n \\ 0 \end{bmatrix} + \begin{bmatrix} m.b.c. \\ c.b.c. \end{bmatrix} \tag{3.29}$$

The pressure has been split in a computable term and an unknown correction:

$$p^{n+1} = p^n + \delta p^{n+1} \tag{3.30}$$

According to the FSM the following approximation is then introduced:

$$A^{-1} \approx \frac{2\Delta t}{3\rho_0 V} I = \Delta t^* \cdot I \tag{3.31}$$

This leads to the following approximated system:

$$\begin{bmatrix} A & 0 \\ D & -D\Delta t^* G \end{bmatrix} \begin{bmatrix} I & \Delta t^* G \\ 0 & I \end{bmatrix} \begin{bmatrix} \vec{u}^{n+1} \\ \delta p^{n+1} \end{bmatrix} = \begin{bmatrix} \vec{r} - Gp^n \\ 0 \end{bmatrix} + \begin{bmatrix} m.b.c. \\ c.b.c. \end{bmatrix} \tag{3.32}$$

Which can be decomposed in the following three steps:

$$A\widetilde{\vec{u}} = \vec{r} - Gp^n + b.c. \tag{3.33}$$

$$DG\delta p^{n+1} = \frac{D\widetilde{\vec{u}}}{\Delta t^*} - b.c. \tag{3.34}$$

[4]Since the system has been written in a block-matrix form, p is a vector but, for the sake of clarity, the over-arrow has been omitted.

$$\vec{u}^{n+1} = \widetilde{\vec{u}} - \Delta t^* G \delta p^{n+1} \tag{3.35}$$

Therefore, first the momentum equations are solved with the pressure field obtained at the previous time step: the resulting velocity field will not be divergence-free $\left(D\widetilde{\vec{u}} \neq 0\right)$; second, the Poisson equation is solved and the pressure correction is calculated. Finally, the velocity field is corrected by means of the pressure correction.

The approximation introduced by the FSM can be evaluated by substituting the relation:

$$A^{-1} = \Delta t^* \cdot I \tag{3.36}$$

in the un-factorized system:

$$\begin{bmatrix} A & \Delta t^* \cdot IAG \\ D & 0 \end{bmatrix} \begin{bmatrix} \vec{u}^{n+1} \\ \delta p^{n+1} \end{bmatrix} = \begin{bmatrix} \vec{r} - Gp^n \\ 0 \end{bmatrix} + \begin{bmatrix} m.b.c. \\ c.b.c. \end{bmatrix} \tag{3.37}$$

The upper right term can be written as:

$$\Delta t^* \cdot IAG = \Delta t^* \left[\frac{I}{\Delta t^*} + (N - L)\right] G = G + \Delta t^* (N - L) G \tag{3.38}$$

The introduced error, which only affects the momentum equations, is therefore:

$$\Delta t^* (N - L) G \delta p^{n+1} = \frac{2\Delta t^2}{3\rho_0 V} (N - L) G \frac{\partial p}{\partial t}\bigg|^n + O\left(\Delta t^3\right) \tag{3.39}$$

and is of the second order in time, since the pressure correction is used, instead of the pressure itself, which would otherwise lead to a first order error. As a consequence, outer iterations are not needed, since the error is of the same order of magnitude of the one introduced by the time discretization. The computational procedure can be summarised as follows:

for $t = 0 : \Delta t : T$

while $R_i > \varepsilon_t$

Solve $\widetilde{\vec{u}}$ equation

Solve $\widetilde{\vec{v}}$ equation

Solve $\widetilde{\vec{w}}$ equation

Update properties

end

Solve pressure correction equation for δp^{n+1}

Correct the velocity field: $\vec{u}^{n+1} = \widetilde{\vec{u}} - \Delta t^* G \delta p^{n+1}$

Correct the pressure field: $p^{n+1} = p^n + \delta p^{n+1}$

while $R_i > \varepsilon_t$

Solve additional equations

end

end where R_i is the scaled residual of the $i - th$ quantity and ε_t is the user-defined tolerance. As mentioned above, the Poisson equation is solved outside the inner iteration loop, i.e. only once per time step: the corrected pressure is then used to compute the next time step.

On the other side, as already noticed, when the PISO is used with an iterative time advancement the calculation of the pressure correction does not directly lead to the following time step but is instead used to update the momentum equations, which must be solved again (outer iterations). Finally it must be noted that the pressure values in the cell-face centres are needed, but since FLUENT is a co-located solver, the pressure values -as the velocity components- are stored in the cell-centres: a pressure interpolation scheme is therefore required.

In the performed simulations the PRESTO! scheme (*pressure staggering option*) has been adopted, which computes the pressure in the cell-face centre by means of a discrete continuity balance for a staggered control volume about the face.

Chapter 4

Problem setup

4.1 Experimental setup

The experiments of Meinders *et al.* [7] were performed in a wind tunnel with a rectangular test section of 600 $mm \times 51$ mm. On one of the walls was mounted a matrix of spatially equidistant cubes, the height of which (H) was 15 mm. The number of the cubes was respectively 25 in the streamwise direction and 10 in the spanwise direction; their face-to-face distance (S) in both directions was 45 mm ($S/H = 4$). A schematic sketch of the matrix is given in figure 4.1.

In order to ensure the full development of the flow in both spanwise and streamwise direction the measurements were performed around the 18^{th} row of cubes counted from the inlet, at mid position of the channel.

The flow field was measured with a Laser Doppler Anemometer (LDA) at a Reynolds number of $Re_H = 3854$, based on the cube height and the bulk velocity $u_b = 3.86$ m/s. The Reynolds number based on the channel height was instead $Re = 13103$.

The heat transfer was measured with infrared thermography at one electrically heated cube located in the centre of the matrix, while all the other cubes remained unpowered. The powered cube consisted of a copper core, whose temperature was kept constant at 75° C, covered with a thin epoxy layer 1.5 mm thick (0.1 H). The inlet temperature ranged between 19° C and 21° C.

4.2 Computational setup

The spatial and temporal periodicity of the flow shown by Meinders' experiments allowed to consider only a subchannel unit with dimensions $4H \times 4H \times 3.4H$. The cube was placed in the centre of the domain, on whose boundaries periodicity conditions were applied. Instead, on the top and bottom wall of the channel no slip conditions were applied.

For what concerns the simulation of the temperature field and the heat flux, the epoxy layer of the cube was meshed, in order to allow simultaneous solution of heat conduction in the layer and heat convection in the fluid and

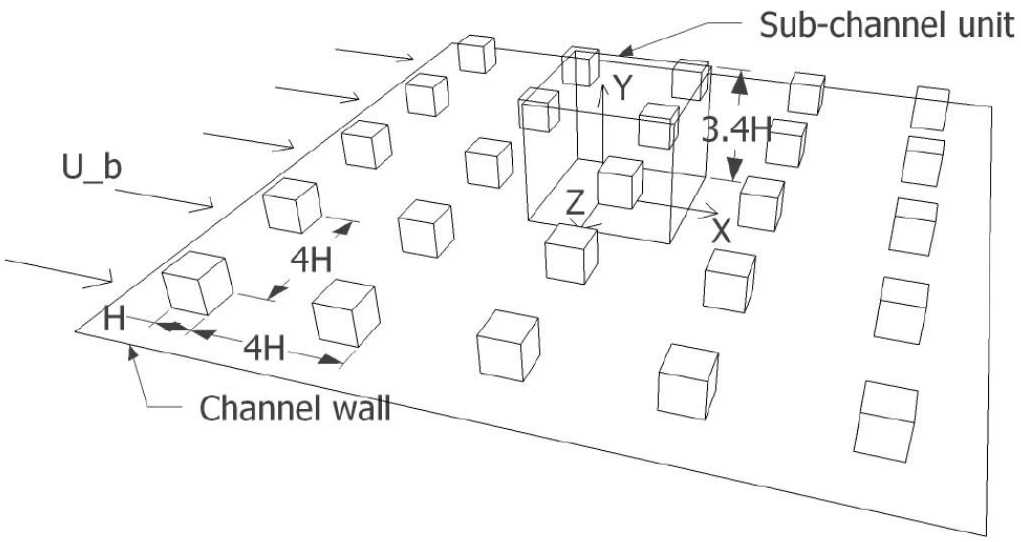

(a) Matrix of cubes

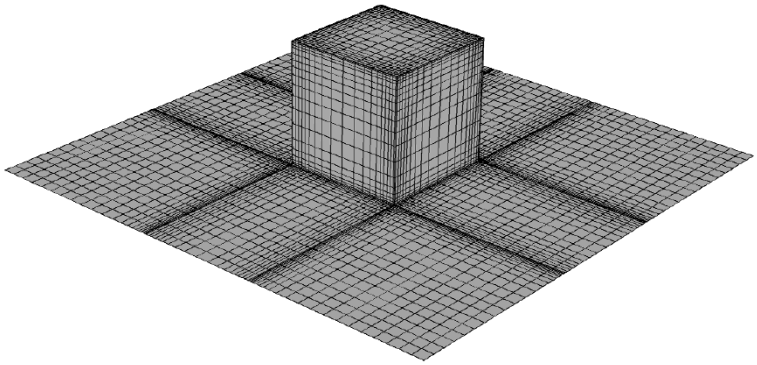

(b) Sub-channel unit

Figure 4.1: Experimental and computational setup.

Symbol	Property	Air	Epoxy
ρ	Density	1.204 kg/m^3	1150 kg/m^3
c_p	Specific Heat	1006.43 $J/kg \cdot K$	1668.5 $J/kg \cdot K$
λ	Thermal conductivity	0.0255 $W/m \cdot K$	0.236 $W/m \cdot K$
μ	Kinematic viscosity	$1.502 \cdot 10^{-5}$ m^2/s	-

Table 4.1: Material properties.

thus obtain the surface temperature of the cube. The inner side of the layer was set to a constant temperature of 75° C, that is the temperature of the copper core: it is correct to assume this temperature to be uniform because of the very high conductivity of copper.

Since in the experiment only one cube was heated, it was not possible to set periodic boundary conditions also for temperature: the temperature of the incoming fluid was therefore fixed to 20° C. This value has also been considered as reference for the computation of the heat flux. The heat transfer through the top and bottom wall of the channel was instead not modelled, as well as the radiative heat flux.

In addition, it must be remarked that in the experimental setup the matrix of cubes was mounted on a vertical wall: buoyancy effects have however not been taken into account, since it was shown [8] that at the considered Reynolds number they are negligible.

The simulations were performed approximately at the same Reynolds number of the experiments: some differences between the target Reynolds number and the effective one is due to the fact that it was preferred to set the pressure gradient's value between inlet and outlet rather than the mass flow rate through the channel. Nonetheless it was shown by the experiments that small variations of the Reynolds number have no significant influence on the results. All relevant physical properties are shown in table 4.1.

4.3 Computational grid

In order to investigate the effects of the mesh refinement on the performance of the tested models two different grids were used: a coarse one and a fine one.

In the first case (shown in figure 4.2) a small number of cells was employed: respectively 5184 for the epoxy layer (with 4 elements across its thickness) and 165600 for the outer region. In y direction (height of the channel) the size of the elements varied between 0.01 H and 0.256 H while in streamwise (x) and spanwise (z) direction it ranged between 0.01 H and 0.11 H. The refinement level of the mesh was higher in the region close to the cube and the walls in order to provide a good resolution of the boundary layer and of the turbulence phenomena, and lower in the upper part of the channel. The sizing of the elements ensured an y^+ value of approximately 1.7 in the near-wall region, with a local maximum of 3.99 around the cube edges.

At the considered Reynolds number and setting the time step size Δt to $3.8 \cdot 10^{-5} s$, this grid spacing led also to a Courant number of 1.286 (0.334 for the LES, where Δt was set to $1 \cdot 10^{-5} s$).

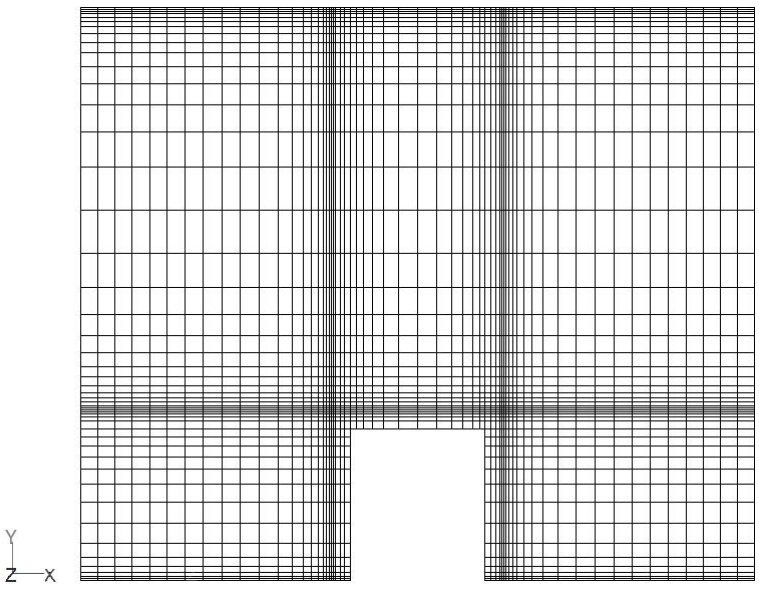

Figure 4.2: Coarse grid.

Mesh	Cells	Cells (epoxy)	Cells (fluid)	y^+ (max)	Max. CFL $\triangle t_1$	Max. CFL $\triangle t_2$
Coarse	170784	5184	165600	3.99	1.286	0.334
Fine	638000	170000	621000	4.15	1.35	0.36

Table 4.2: Grid properties. $\triangle t_1 = 3.8 \cdot 10^{-5}$ and $\triangle t_2 = 1 \cdot 10^{-5}$.

The fine grid (shown in figure 4.3) was obtained from the coarse one keeping the same minimum element size of 0.01 H, but increasing the number of elements per edge. The total number of cells was 638000, respectively 17000 for the epoxy layer (5 elements across its thickness) and 621000 for the fluid domain. The element size ranged from the minimum to 0.13 H in y direction and to 0.1 H in streamwise and spanwise direction.

The near wall y^+ value was approximately 1.5, while the local maximum around the cube edges was 4.15; the cell Courant number (abreviated with CFL, Courant-Friedrichs-Levy number) was 1.35 (0.36 for the LES), considering the same time step size as for the coarse grid. Table 4.2 summarizes

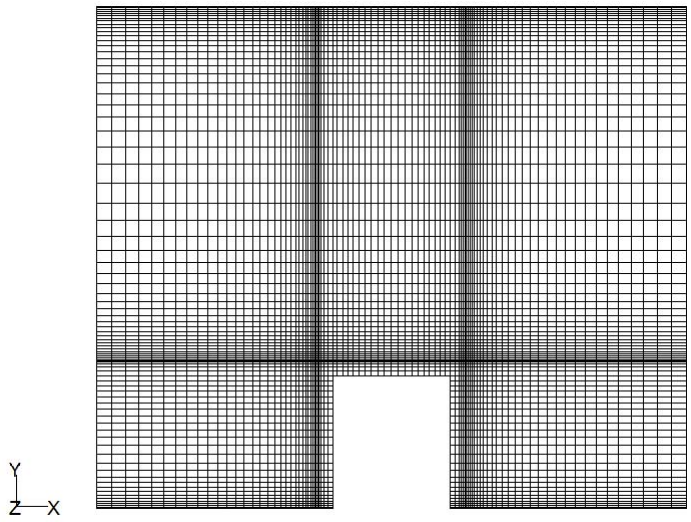

Figure 4.3: Fine grid.

the properties of both grids. Since the problem had a very simple geometry it was possible to adopt structured computational grids.

It must anyway be noted that both grids were not specifically designed for LES simulations because the majority of the performed computations adopted a RANS (or hybrid RANS-LES) approach: the grids are therefore well suited for this kind of simulations. Otherwise, adopting a LES approach, the strong grading -especially in y direction- of the cell size determined a loss of resolution that slightly affected the results of the computations.

4.4 Numerical procedure

In this section a brief summary of the adopted numerical procedure will be given, although many issues have already been discussed in the previous chapters.

The flow was always considered unsteady: where possible a second order implicit transient formulation was adopted, with a non iterative time advancement (NITA) and the fractional step method (FSM) was used for coupling pressure and velocity. The choice of this kind of schemes is due to the fact that they permit to considerably reduce the computational time.

Only with the non linear $k-\varepsilon$ model it has not been possible to adopt the same settings, because of its specific implementation in ANSYS FLUENT. In this case an iterative time advancement was therefore chosen and the PISO algorithm was used for the pressure-velocity coupling.

For what concerns the space discretization, a second order upwind scheme was adopted, with the exception of SAS and LES simulations, where the bounded central differencing scheme was adopted.

Finally, the pressure was discretized by means of the PRESTO! algorithm while the gradients were always computed with the least-squares cell based method.

4.5 Setting of periodic conditions

In case of periodic boundaries FLUENT allows to choose between two periodic conditions: specified mass flow rate and specified pressure gradient. The

choice of the kind of time advancement -iterative or not iterative- restricts indeed the number of available options: when the NITA scheme is adopted, it is in fact not possible to impose a mass flow rate through the inlet and outlet surface. Only the pressure gradient between these surfaces can be specified.

It has therefore been possible to set the mass flow rate only in the simulation with the non linear $k - \varepsilon$ model, where the NITA scheme could not be employed, while in all the other simulations a pressure gradient had to be specified.

So, first of all a steady simulation with a standard $k - \varepsilon$ model was performed, in order to find a suitable value for the pressure gradient, which was found to be approximately $-7\ Pa/m$. This value was then taken as reference for all other computations and was successively adapted case by case in order to ensure a correct mean mass flow rate. It must however be noted that small corrections of this value are necessary because also if the fixed gradient is always the same, the choice of the turbulence model and the mesh refinement grade determine a different resulting mass flow rate through the computational domain.

With the LES simulations a slightly different approach was adopted. In this case, in fact, only one subgrid scale model was used, so only the mesh refinement grade affected the mass flow rate. It was therefore decided to keep the same pressure gradient for both the coarse and the fine grid, in order to investigate the effects of the mesh on the results.

Finally it should be observed that such an approach, i.e. the choice of a pressure gradient and its correction with regard to the average mass flow rate, could not ensure that precisely the target mass flow rate value was reached; nonetheless, as mentioned above, the results are not very sensitive to small variations of the Reynolds number therefore small differences from the target value were considered acceptable.

Table 4.3 summarizes the computational settings of the different cases while table 4.4 shows the different periodic settings and their effect on the average values of the bulk velocity and the Reynolds number.

Mesh	Turbulence model	$p-v$ coupling	Time discr.	Space discr.	Pressure discr.
coarse	$k-\omega$	FSM	II o. NITA	II o. upwind	PRESTO!
coarse	SAS	FSM	II o. NITA	Bounded c. diff.	PRESTO!
fine	$k-\omega$	FSM	II o. NITA	II o. upwind	PRESTO!
fine	SAS	FSM	II o. NITA	Bounded c. diff.	PRESTO!
fine	$k-\varepsilon$	FSM	II o. NITA	II o. upwind	PRESTO!
fine	$k-\varepsilon-NL$	PISO	II o. ITA	II o. upwind	PRESTO!
coarse	LES	FSM	II o. NITA	Bounded c. diff.	PRESTO!
fine	LES	FSM	II o. NITA	Bounded c. diff.	PRESTO!

Table 4.3: Numerical settings.

Mesh	Turbulence model	∇p Pa/m	v_{bulk} m/s	Re_H	% Diff. from target
coarse	$k-omega$	-5.85	3.80	3794,94	-1.55
coarse	SAS	-5.60	3.94	3934,75	2.07
fine	$k-omega$	-6.75	3.94	3934,75	2.07
fine	SAS	-6.00	3.99	3984,69	3.36
fine	$k-\varepsilon$	-7.66	3.85	3844,87	-0.25
coarse	LES	-7.00	3.60	3595,21	-6.73
fine	LES	-7.00	3.75	3745,01	-2.85
fine	$k-\varepsilon-NL$	-9.77	3.86	3854,86	0

Table 4.4: Periodic settings. With the $k-\varepsilon-NL$ model the mass flow rate was specified (0.01422 kg/s) instead of the pressure gradient. Target values were 3.86 m/s for the bulk velocity and 3854 for the Reynolds number.

Chapter 5

Results

5.1 General flow structure

Before explaining in detail the results of the simulations it is useful to give a brief description of the general flow structure, as shown by Meinders *et al.* [7]. A schematic sketch of the main features of the flow is given in figure 5.1. The formation of distinct vortex structures takes place only in the immediate

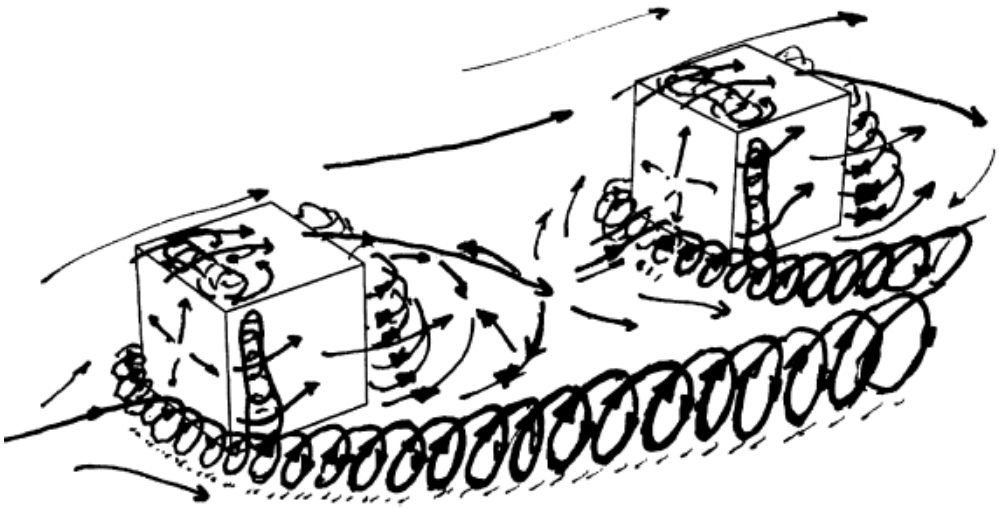

Figure 5.1: Sketch of the three dimensional flow pattern (from [7])

proximity of the cube, while in the upper region of the channel and in the streamwise corridors between the cubes the flow remains almost undistorted.

A horseshoe vortex forms at the windward face and it is then deflected downstream along both sides of the cube. It becomes then weaker proceeding further in the streamwise direction, as it interacts with the counter-rotating vortices formed along the side-neighbouring cubes. This results in negative velocities close to the side of the cube. Furthermore, the impinging flow separates at the leading edges giving rise to small recirculation bubbles on the top and side faces of the obstacle –which reattach few millimetres downstream– and to a two-cell recirculation structure immediately downstream of the cube, which causes a significant upwash close to the leeward face.

Besides the two recirculations, the wake flow is also dominated by the arch-shaped vortex, which originates from the flow separation on the front

edges. The flow then reattaches at about half cube height downstream of the cube. The centres of the two spirally wound vortices in the wake are clearly visible by means of an oil-film visualization (figure 5.2). In the same

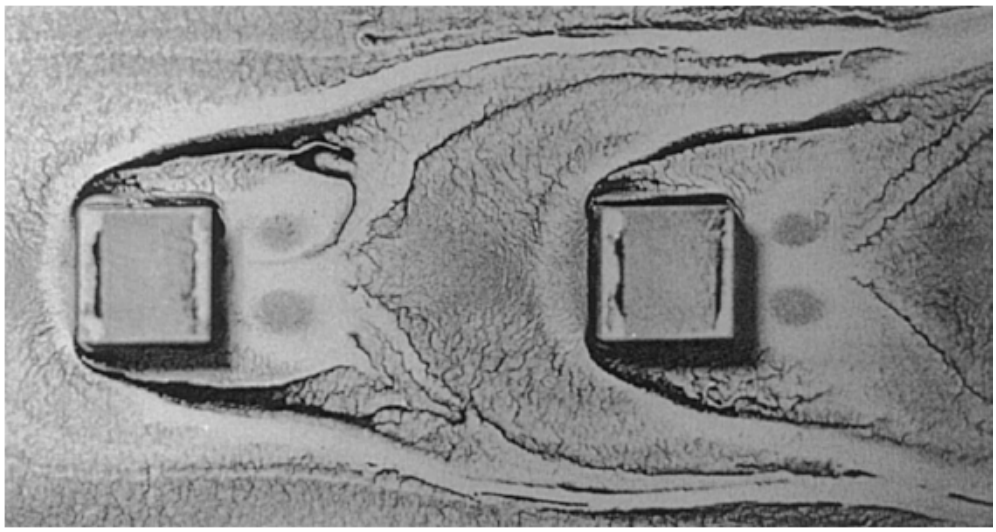

Figure 5.2: Oil-film visualization of the surface streaklines.

figure it is also possible to observe the horseshoe vortex, whose imprint is the white line which originates in front of the cube and bends downstream along the separation line, and the small recirculation on the top face, close to the leading edge.

The vector plots in figure 5.3 and 5.4 show the results of the measurements of Meinders *et al.* [7] for the plane $x - y$ and half $x - z$ plane. In this brief description of the general features of the flow around the cube the temperature field on and around its surfaces has not been considered. However, it goes without saying that the temperature distribution is strictly correlated with the turbulent phenomena: in presence of large recirculations the surface temperature will locally increase, while in zones characterised by strong flow accelerations the cooling will be more efficient.

As a consequence, numerical simulations that aim to give a good prediction of the local heat transfer characteristics must necessarily adopt an accurate turbulence model, since the two problems (i.e. heat transfer and turbulence) are strictly coupled.

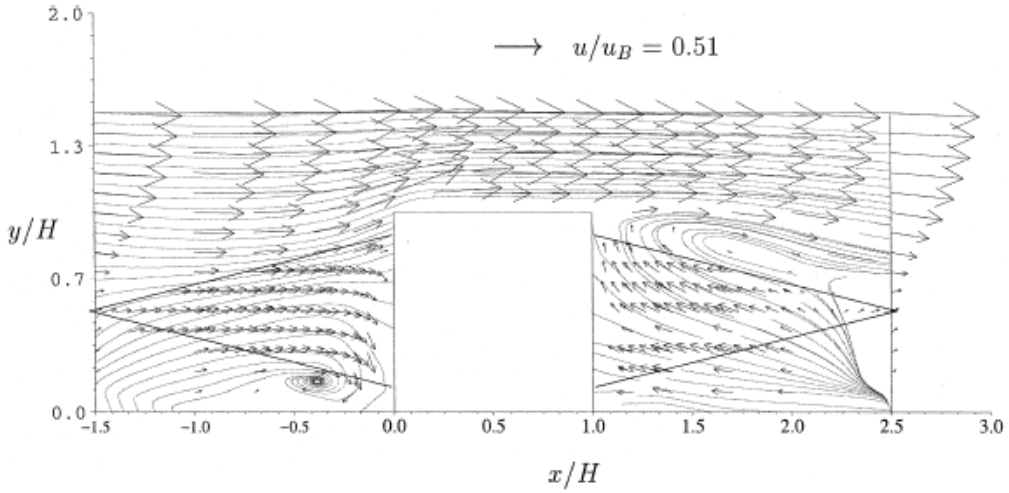

Figure 5.3: Time averaged vector plot on the $x - y$ plane at $z/H = 0$. The vectors in the triangular regions were obtained with laser measurements.

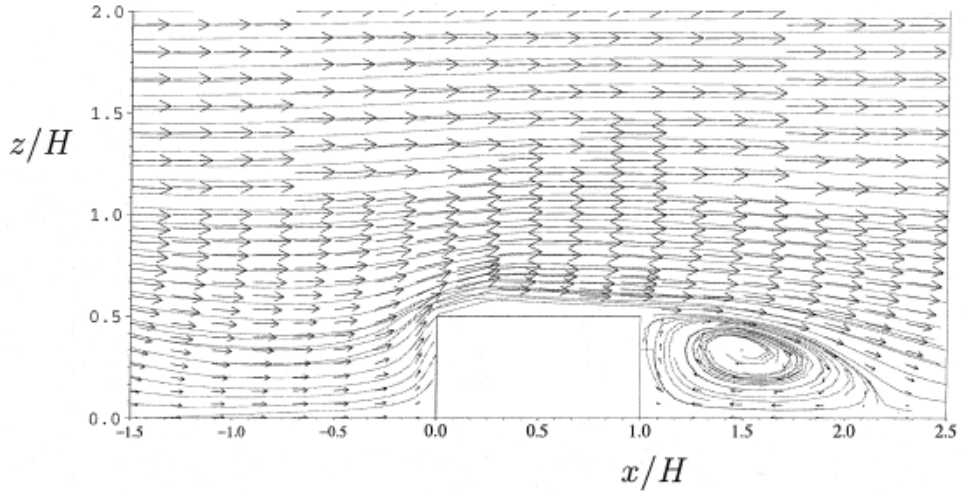

Figure 5.4: Time averaged vector plot on half $x - z$ plane at $y/H = 0.5$.

5.2 Numerical results

As mentioned in the previous chapters, the aim of the present work is to compare the performances of different turbulence models, taking into account the effect of the computational grid. Several simulations with different models have therefore been performed, and their results have then been compared with measurements.

Three main characteristics of the flow have been investigated: first of all its dynamic behaviour, i.e. vortex shedding phenomena, second the mean velocity profiles and the mean Reynolds stresses and finally the mean temperature field and the mean heat transfer coefficient through the cube surfaces[1]. In addition, at the end of this chapter, some further results for which experimental data are not available will be shown.

Figure 5.5 shows the origin of the coordinate system and the pathlines along which the measurements of velocity and temperature were taken.

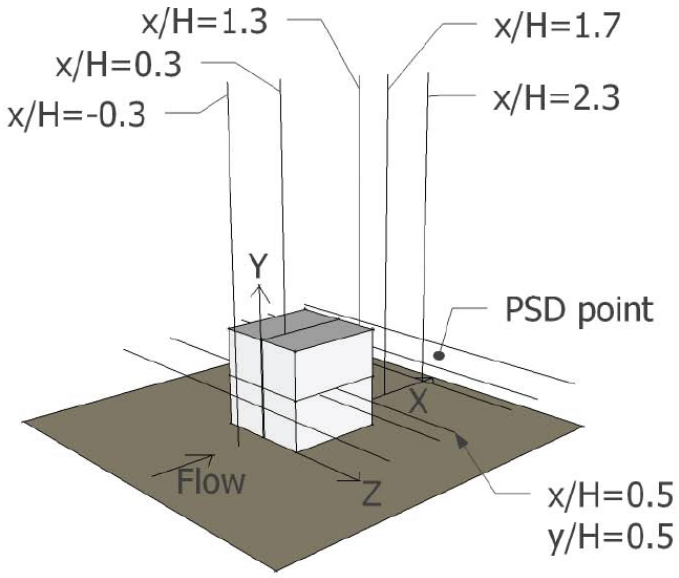

Figure 5.5: Pathlines and coordinate system origin.

Velocity measurements refer to the horizontal and vertical pathlines in the fluid domain, as summarized in Table 5.1.

[1]Mean data have been exported from FLUENT, and are based on a flow time of minimum 5 seconds.

Pathlines	x/H	y/H	z/H
Horizontal	-0.3	0.5	From -2 to 2
	0.3	0.5	From -2 to 2
	1.3	0.5	From -2 to 2
	1.7	0.5	From -2 to 2
	2.3	0.5	From -2 to 2
Vertical	-0.3	From 0 to 3.4	0
	0.3	From 0 to 3.4	0
	1.3	From 0 to 3.4	0
	1.7	From 0 to 3.4	0
	2.3	From 0 to 3.4	0

Table 5.1: Pathlines

Pathlines	y/H	z/H
Horizontal	0.25	
	0.52	
	0.75	
Vertical		0.02
		0.18
		0.32

Table 5.2: Surface pathlines

An additional horizontal pathline at$x/H = 0.5$, $y/H = 0.5$ from $z/H = 0.5$ to $z/H = 2$ is used to detect the presence of the horseshoe vortex. Furthermore, as in the experiment, a point has been defined in the wake of the cube (the *psd point* in figure 5.5) at $x/H = 2$, $y/H = 0.5$, $z/H = 0.5$, where time sampling of the spanwise component (w) has been carried out, in order to obtain its power density spectrum.

Finally, the temperature and heat transfer coefficient measurements refer to the pathlines on the cube surface whose positions are summarized in table 5.2. Since all these pathlines lay on a plane with constant y/H or z/H, only this coordinate is used to define the line. For the sake of clarity, in figure 5.5 only two surface pathlines -a horizontal one and a vertical one- are shown.

5.3 Dynamic behaviour

As mentioned above, like in the experiment, in order to detect coherent structures the power density spectrum of the spanwise component of the velocity in a point in the wake of the cube was calculated. The dominant characteristic frequency was then derived from the location in the spectrum which corresponded to a maximum of energy.

The experiments showed a vortex shedding frequency of ca. 27 Hz: this value was then made dimensionless with the cube size and the bulk velocity to yield the Strouhal number:

$$St = \frac{Hf}{u_b} \tag{5.1}$$

which was found to be 0.109. In the performed simulations a flow time of minimum 5 seconds was considered, which corresponded to about 130 vortex shedding cycles.

In order to obtain a clearer graph and highlight the fundamental frequencies, the collected data were then processed by means of the Welch's averaged modified periodogram method of spectral estimation implemented in Matlab: the data were divided into eight sections with 50% overlap, which were then windowed with a Hamming window.

In figure 5.6 the power density spectra obtained with the coarse grid are shown; the frequency of 27 Hz which was measured in the experiments has been highlighted by means of a black solid line.In figure 5.7 are shown the results obtained with the fine grid. As in the experiment, the spectra have all been truncated at $4 \cdot 10^2$ Hz: higher frequencies, in fact, are not related to resolved structures. Regardless of the adopted grid, the spectra confirm that as the resolution capabilities of the turbulence models increases, the energy content of the signal increases and is spread over a wider range of frequencies.

The $k - \omega$ model is only able to capture the single vortex shedding frequency: this is clearly visible in the graph, where peaks of power spectral density are associated to the fundamental frequency and its multiples. Since it has been developed as an hybrid between URANS and LES models, the

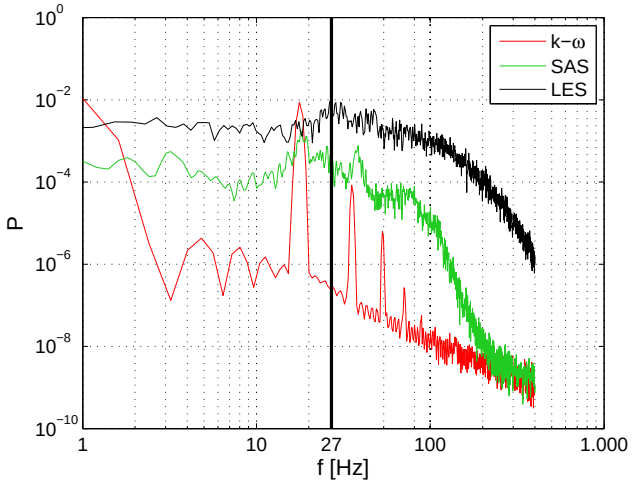

Figure 5.6: Power density spectra of the w-component obtained on the coarse grid with different models.

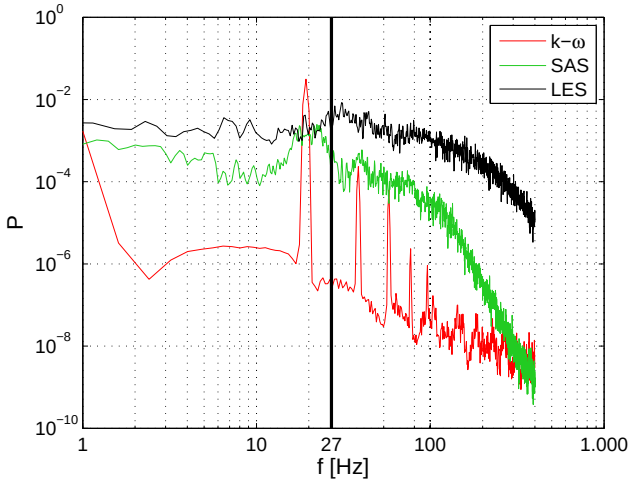

Figure 5.7: Power density spectra of the w-component obtained on the fine grid with different models.

Grid	Model	f Hz	St
Coarse	$k-\omega$	17.67	0.070
	SAS	18.27	0.070
	LES	28.61	0.112
Fine	$k-\omega$	19.27	0.074
	SAS	23.00	0.086
	LES	30.90	0.129

Table 5.3: Shedding frequencies and Strouhal numbers.

SAS model is able to resolve smaller scales than the $k-\omega$ model: as a consequence, there is a wider range of energy containing frequencies and a peak at the fundamental shedding frequency.

Finally the LES shows the highest spectral content, as it is able to resolve the smallest scales. As shown in table 5.3, the best predictions of the shedding frequency are given by the large eddy simulations: the $k-\omega$ and the SAS model tend in fact to underestimate it. It is also interesting to notice a certain similarity between the results obtained with these two models: like the $k-\omega$, also the SAS model predicts in fact peaks of power density at frequencies that are multiples of the fundamental one. Furthermore, even if the spectral content of the SAS is higher than that of the $k-\omega$, it is still too low -compared to the peak value- to sensibly affect the value of the fundamental frequency. It means that even if the model is able to capture turbulent fluctuations, they are still too weak to have an influence on the main flow features. The $k-\varepsilon$ models -linear and non linear- have not been considered because even if adopted in unsteady simulations, their results were nonetheless steady velocity fields: all the unsteadiness was duped by the viscosity.

Finally, it is important to notice that with the $k-\omega$ and SAS model the difference between measured data and numerical predictions is due to the incapability of the models to reconstruct small scales of motion. The over-prediction of the turbulent viscosity does in fact μ_t damp out the turbulent fluctuations. This error does not depend on the computational grid: a mesh refinement, in fact, only slightly modifies the results.

On the other side the results obtained with the LES are much more accurate: the error is mainly due to the fact that -as mentioned above- the grids were well suited for URANS simulations and not for LES, since one of the aims of the present work was to check the performance of LES on URANS grids.

5.4 Velocity field

Since the results of the large eddy simulations best agree with the measured data, it is useful to start from them the analysis of the results. In the streamline plots (figure 5.8) it is possible to observe the mean recirculation regions. In figure 5.8(a) the horseshoe vortex in front of the cube is clearly visible, as well as the recirculation in the wake of the cube, bounded by the shear layer, which causes a strong upwash close to the rear wall. Finally a small recirculation can also be found at the foot of the rear face, due to the arch vortex. The plot in figure 5.8(b) refers to a plane which is very close to

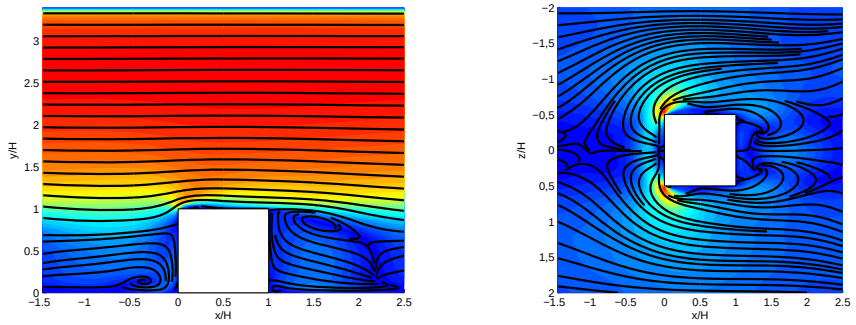

(a) Plane $x - y$, $z/H = 0$ (b) Plane $x - z$, $y/H = 0.006$

Figure 5.8: LES with fine grid: streamlines and contours of mean velocity in the plane.

the base wall ($y/H = 0.06$), and it closely resembles the oil-film visualization of the flow streaklines obtained by Meinders and Hanjalić [7].

It can be noticed how the horseshoe vortex forms in front of the cube (vortex centre in $x/H = -0.5$, see figure 5.8(a)) and bends around it along the separation line. Furthermore the streamlines reveal the presence of two

counter rotating foci in the wake, which form -together with the recirculation close to the top surface (figure 5.8(a))- the arch shaped vortex. The reattachment point in the wake of the cube is predicted approximately at $x/H = 2.5$, in good agreement with the experimental data. Two recirculation bubbles, produced by the separation of the flow from the sharp leading edges, are also visible on the side faces of the cube. Finally, it can be observed that in the core region above the cube and in the streamwise corridors between the cubes the flow remains almost undistorted.

In figure 5.9 are shown the mean velocity profiles of the streamwise component (u) of the velocity along the vertical pathlines summarised in table 5.1. The circles represent the measured values, while the coloured lines refer to the different adopted turbulence models; velocity is made dimensionless by means of the bulk velocity and every profile -with the exception of the first one- has been offset of one unit from the previous one. As mentioned

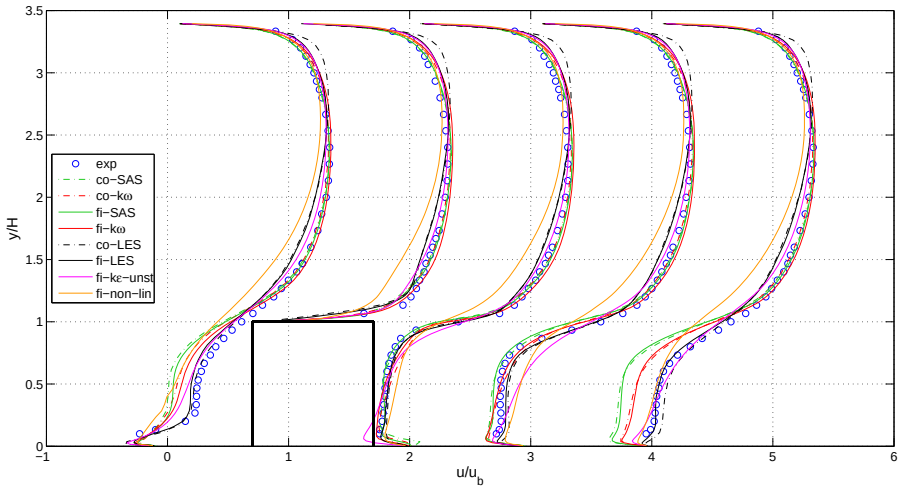

Figure 5.9: Vertical profiles of the mean streamwise component of the velocity u at $z/H = 0$.

above, both the coarse and fine-grid LES lead to the most accurate results, especially in the region $y/H < 1$. On the contrary, in the region above the cube ($y/H > 1$), a certain difference between numerical and experimental data can be noticed. The causes of this lack of accuracy are mainly two.

First of all, the adopted computational grids were designed to be well suited for URANS applications and not for LES, so they are significantly refined in the cube region and close to the walls, but quite coarse in the upper part of the channel. The coarseness of the mesh and the strong resulting cell-size grading between different regions imply therefore a worse performance of the large eddy simulations for $y/H > 1$.

Second, LES performed with finite volume solvers typically suffer of a lack of accuracy in simulations of simple channel flows, because they are not able to properly reconstruct the very-small-scale turbulence phenomena located in the near-wall regions. The length scales of these structures are in fact considerably smaller than the typical filter cutoff frequency but have a certain energy content, which is incorrectly transferred to larger length scales. This is clearly visible in figure 5.10, which shows a comparison (from [6]) between two velocity profiles for a flow in a simple channel obtained respectively with a DNS and a LES: the large eddy simulation sensibly overestimates the velocity. On the contrary, in presence of an obstacle -a cube, in this case- the

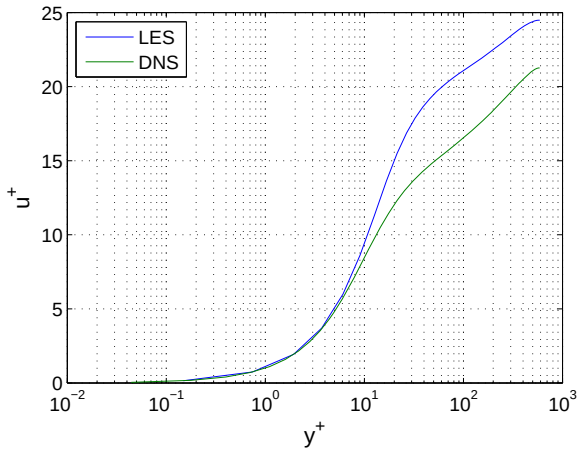

Figure 5.10: Comparison between LES and DNS in a simple channel.

flow around it is characterised by larger scales with higher energy content and the effects of the smallest scales can be supposed to be negligible.

The results of the performed simulations are therefore affected, for what concerns the upper part of the channel, by the two problems mentioned

above; nonetheless, since the aim of the simulations is the reconstruction of turbulence in proximity of the cube and the prediction of the local heat transfer coefficient on the cube surfaces, this lack of accuracy for $y/H > 1$ is not of great importance. Close to the cube, all the other models (5.9) perform worse than the LES. Starting from the top face, the small recirculation bubble is captured only by the $k - \omega$, as it can be seen in figure 5.11. Furthermore

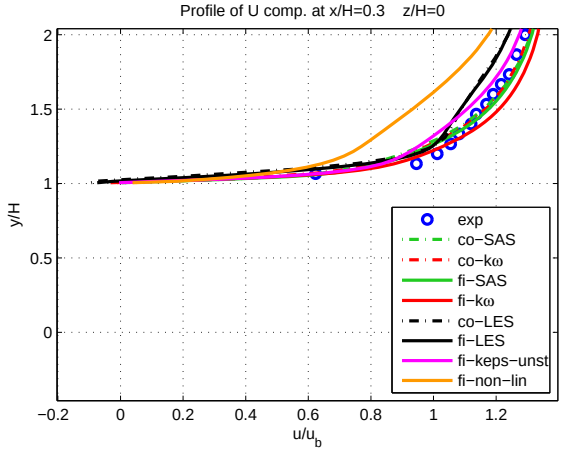

Figure 5.11: Mean streamwise velocity (u) along the vertical pathline $x/H = 0.3$ at $z/H = 0$.

URANS models show a lack of accuracy in the reconstruction of the profiles in $x/H = -0.3$ and$x/H = 2.3$, which are located approximately in the centre of the recirculation in front of the cube and close to the reattachment point in the wake.

The difference between the profiles can be better understood analysing the streamline plots obtained with each model shown in figure 5.12. The positions of the centres of the recirculations in front of the cube and in the wake are incorrectly predicted by all models, as well as their dimension.

In figure 5.13 are shown the velocity profiles along the vertical pathlines $x/H = -0.3$, $x/H = 1.3$, $x/H = 1.7$, $x/H = 2.3$, for$y/H < 1.2$. In these and in the following plots it is also possible to notice that the results -with the exception of the LES- do not strictly depend on the grid resolution. The main problem is that all the URANS models fail to reconstruct the recirculation zone close to the leeward face of the cube and do not correctly predict the

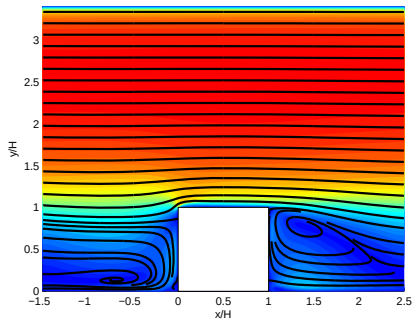

(a) $k-\varepsilon$: $z/H = 0$

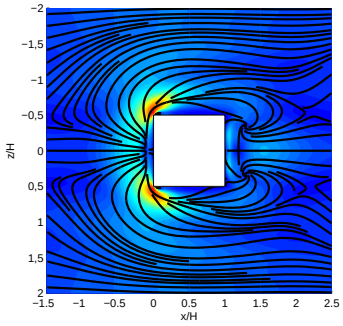

(b) $k-\varepsilon$: $y/H = 0.006$

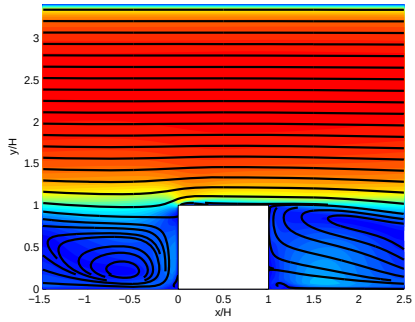

(c) $k-\omega$: $z/H = 0$

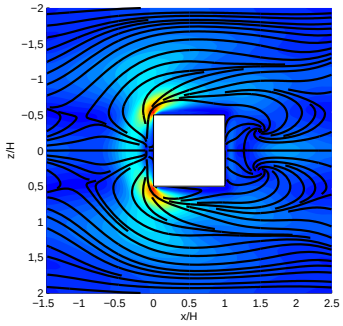

(d) $k-\omega$: $y/H = 0.006$

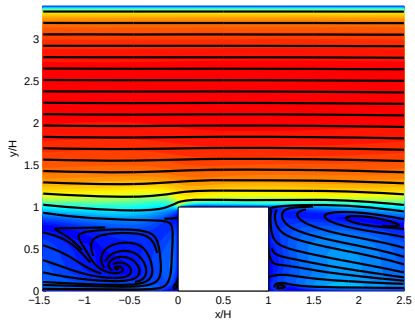

(e) SAS: $z/H = 0$

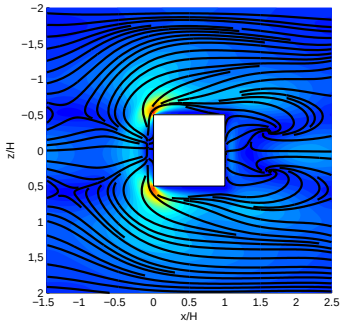

(f) SAS: $y/H = 0.006$

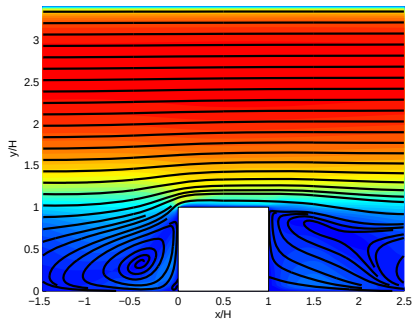

(g) $k-\varepsilon-NL$: $z/H = 0$

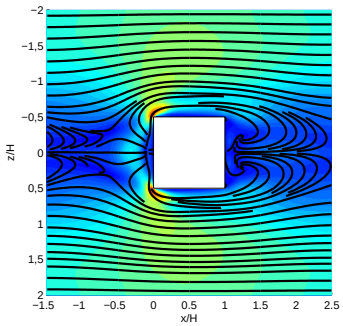

(h) $k-\varepsilon-NL$: $y/H = 0.006$

Figure 5.12: Streamline plots with contours of the mean velocity in the plane.

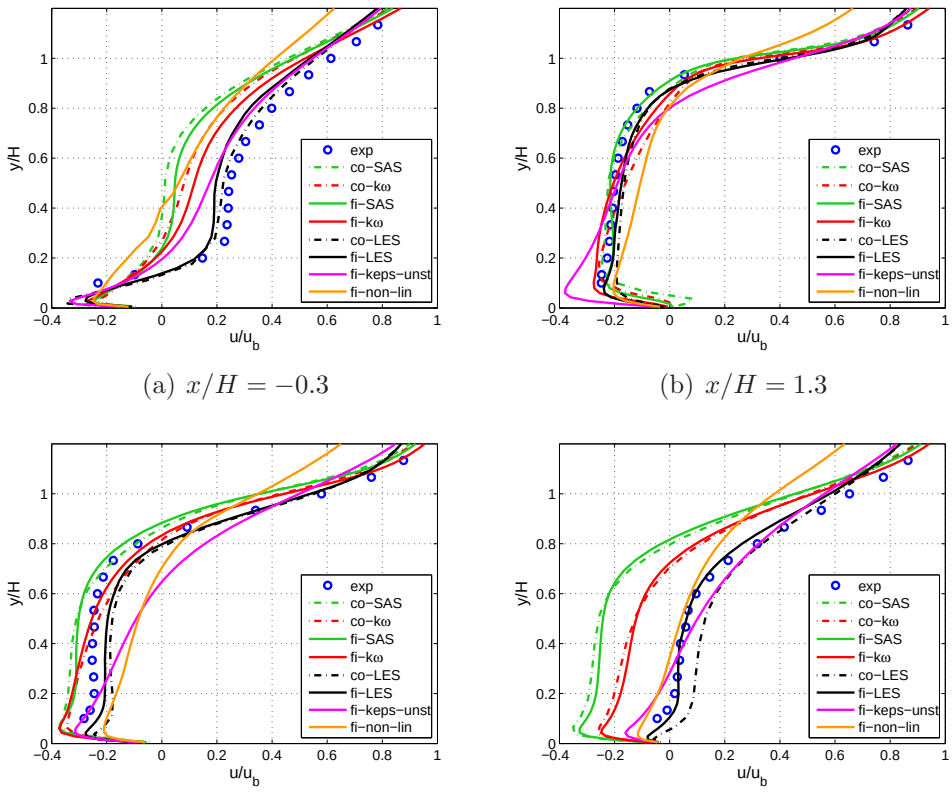

(a) $x/H = -0.3$ (b) $x/H = 1.3$

(c) $x/H = 1.7$ (d) $x/H = 2.3$

Figure 5.13: Vertical profiles of the mean streamwise component of velocity (u) at $z/H = 0$.

position of the reattachment point, which is shown by the measurements to be approximately in $y/H = 2.5$. This yields a too slow flow recovery in $x/H = -0.3$, which leads to an underestimation of u upstream of the cube and to an incorrect prediction of the position of the centre of the upstream vortex, which is located by all models in $y/H > 2.5$.

Among all URANS models, the one that gives the best prediction of the position of the reattachment point is the non linear $k - \varepsilon$, but this model is not able to accurately reconstruct the upstream vortex -which is considerably stretched compared with the other models- and gives the poorest conformance with experimental results for u in $x/H = -0.3$. A plausible cause of the stretching could be an influence of the third order terms which appear in the definition of the Reynolds stress tensor: similar results have in fact ben obtained with the non linear models which are available in FLUENT; this issue remains however unresolved and further investigation is needed. On the other side the sensible underestimation of u just upstream of the windward face of the cube leads -in order to maintain mass conservation- to an overestimation of u for $|z/H| > 0.5$ on the horizontal pathlines at $y/H = 0.5$, as shown in figure 5.14, where the u profiles along the horizontal pathlines of table 5.1 are shown; this also explains the high velocity values visible in figure 5.12(h). On the contrary, since the standard $k - \varepsilon$ gives the best results -among the URANS simulations- for u along the vertical line at $x/H = -0.3$, also the prediction of u along the horizontal pathlines is quite accurate, although it is not able to detect the velocity decrease in the centre of the channel.

It is important to remark that pointing out such a relationship between the profiles of u in the vertical and in the horizontal plane is only possible with the simulations performed with the $k-\varepsilon$ models, because -as mentioned above- even if the case was set as unsteady, the computations lead to a steady velocity field. On the contrary, this is not possible in case of unsteady velocity fields, because the time dependency makes this relationship less evident. This is for example the case of the $k - \omega$ simulations, which in $x/H = -0.3$ underestimate u on the vertical line (for $y/H < 1$) as well on the horizontal line (at $y/H = 0.5$).

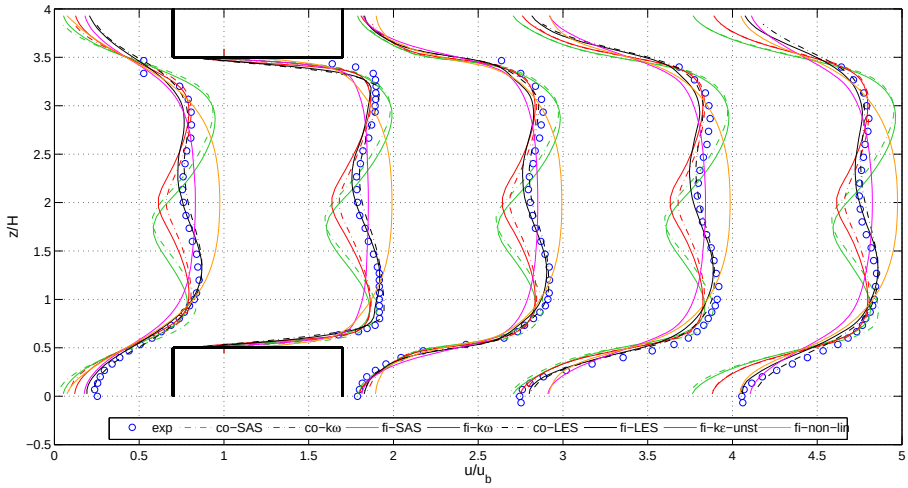

Figure 5.14: Horizontal profiles of the mean streamwise component of the velocity (u) at $y/H = 0.5$.

Furthermore, as shown also in the plots in figure 5.15, consistently with the overestimation of the reattachment length downstream of the cube, all models predict -in disagreement with the experimental data- a reverse wake flow for $x/H = 2.3$. Only the two $k-\varepsilon$ lead to a positive u/u_b value in $x/H = 2.3$, coherently with the fact that -among all URANS simulations- they give the best estimation of the position of the reattachment point and of the velocity profile in$x/H = 2.3$. All models, with the only exception of the non linear $k-\varepsilon$, are also able to capture the thin reverse flow on the side faces of the cube ($x/H = 0.3$).

Another interesting flow feature highlighted by SAS and LES simulations is an asymmetry of the u profiles on the horizontal pathlines with respect to the centre of the channel ($z/H = 2$), as clearly visible in figure 5.14 and in figure 5.15. With respect to the u component on the horizontal plane at $y/H = 0.5$, SAS simulations lead to a sensibly asymmetric velocity field, since the mean spanwise component of the velocity is non- zero. The under- and overestimation of the local peaks of u respectively at $z/H \approx 1$ and $z/H \approx 3$ also suggest that the calculated velocity profiles might be specular to the correct ones. This is also the case of the large eddy simulations, whose re-

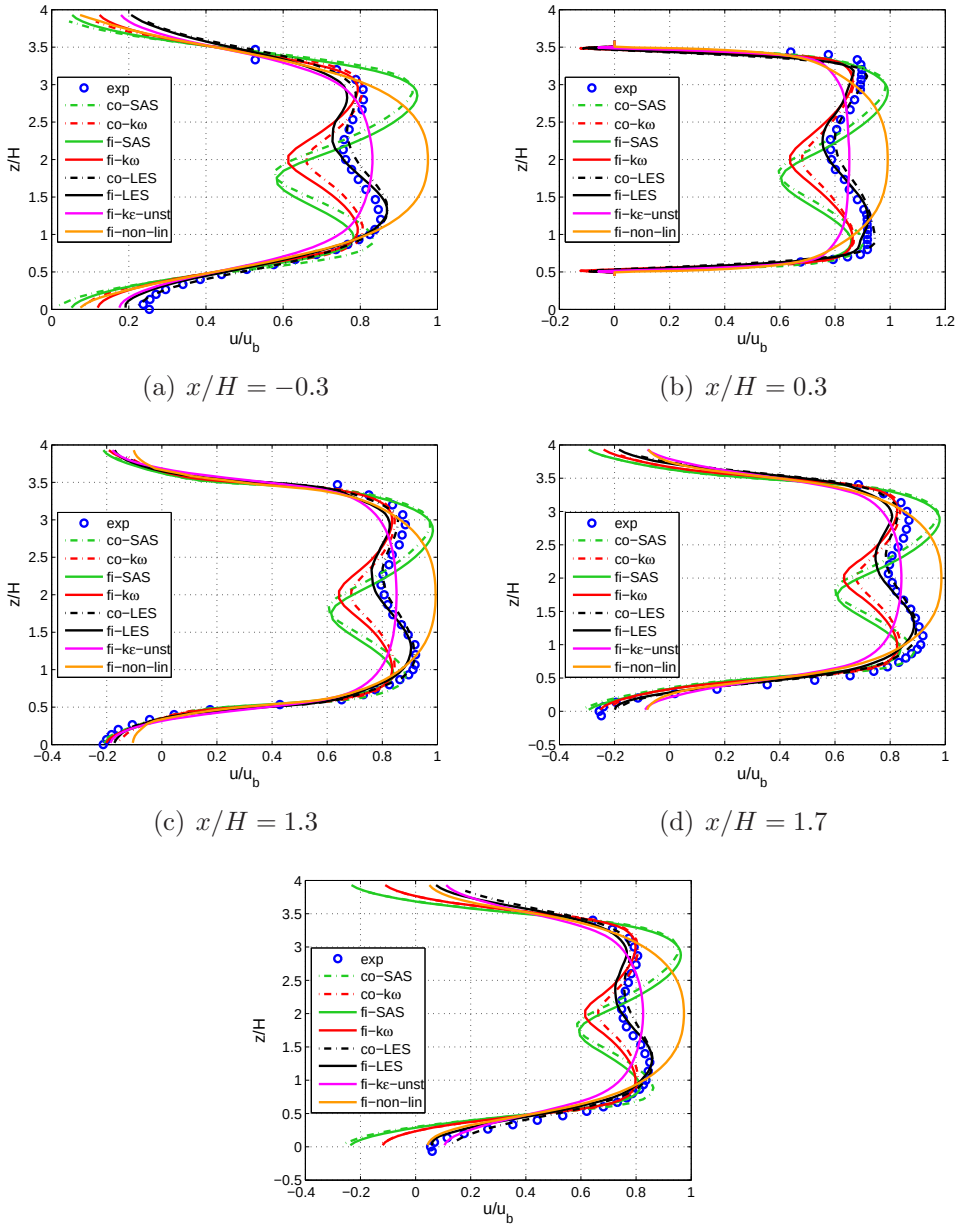

(a) $x/H = -0.3$ (b) $x/H = 0.3$

(c) $x/H = 1.3$ (d) $x/H = 1.7$

(e) $x/H = 2.3$

Figure 5.15: Horizontal profiles of the mean streamwise component of velocity (u) at $y/H = 0.5$.

sults are in good conformance with measurements and accurately reproduce their slight asymmetry; it was however surprisingly noticed that the results of the LES varied according to the starting point of the time sampling, although the number of data points was sufficiently large to ensure a correct time averaging. Some calculations lead to results in good agreement with the experimental data, as those shown in the figures above; others, on the other side, lead to profiles which were specular to these ones. A plausible cause could be some very-low-frequency phenomenon which could not be detected because the computational time would have been too high. Otherwise it is also possible that the asymmetry of the velocity field might actually be physical and that the mean direction of the flow might not be exactly parallel to the x-axis. If this is the case, an interesting question is how it is possible that an asymmetric solution is obtained on a symmetric domain with symmetric boundary conditions. However this currently remains an unresolved issue requiring further investigation. Some similar cases can be found in literature(e.g., [16]).

In figure 5.16 the mean profiles of the spanwise component (w) of the velocity along the horizontal pathlines are shown. In conformance with the measurements, all models capture the peak velocities close to the side faces of the cube in $x/H = 0.3$, although the accuracy of the prediction of the w profile changes among the different models. However, this suggests that the length of the separation bubble originating from the sharp vertical edge of the cube is not underestimated.

The best results are given by the LES on the fine grid, while on the coarse grid the LES shows some lack of accuracy in certain stations; among the URANS simulations, the best results, with the only exception of the pathline at $x/H = 0.3$, are given by the $k - \varepsilon$ model, and are very similar to those of the LES on coarse mesh.
Since the sign of the mean w velocity changes between $x/H = 1.3$ and $x/H = 1.7$, the centres of the two downstream recirculations close to the leeward face of the cube can be estimated to be somewhere between these two pathlines. This result is in good conformance with experimental measurements: from the streaklines on the horizontal plane (shown in figure 5.2) it can in fact

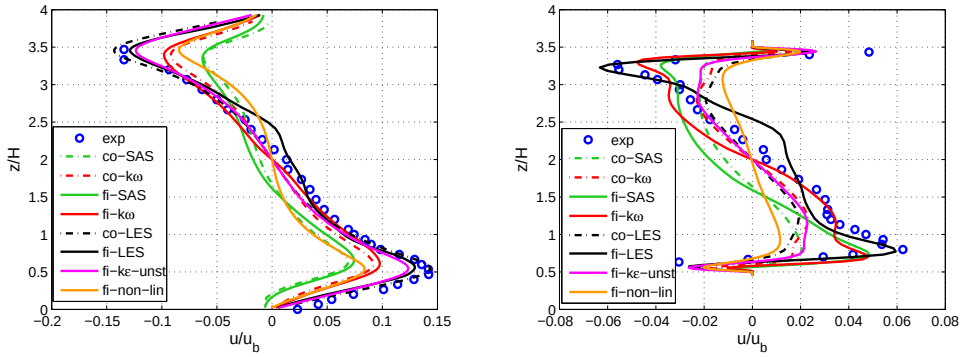

(a) $x/H = -0.3$ (b) $x/H = 0.3$

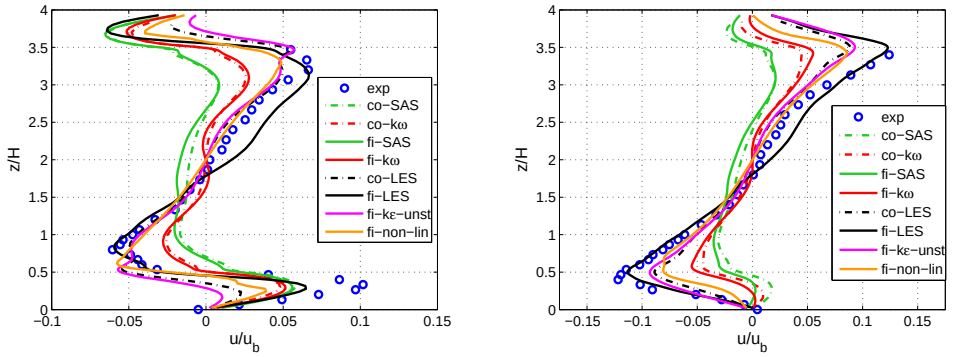

(c) $x/H = 1.3$ (d) $x/H = 1.7$

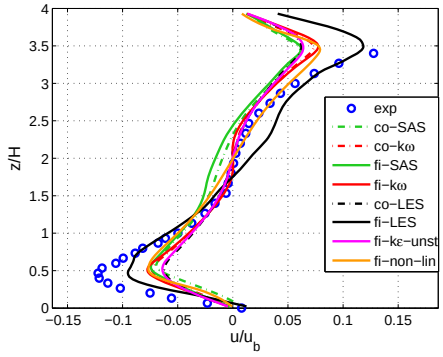

(e) $x/H = 2.3$

Figure 5.16: Horizontal profiles of the mean spanwise component of velocity (w) at $y/H = 0.5$.

be clearly noticed that the two counter rotating foci are located exactly in this position. The underestimation of w in $x/H = 2.3$ is due to the incorrect prediction of the position of the reattachment point downstream of the cube, which determines a too slow flow recovery.

Consistently with the prediction of an asymmetric velocity field, the w profiles obtained with LES and SAS simulations are non-zero in the centre of the channel ($z/H = 2$): the more the predicted asymmetry is strong, the more the value of w differs from zero. It must however be noticed that also the experimental profiles do not always exhibit a zero w-component of the velocity in $z/H = 2$: for example in $x/H = -0.3$ and $x/H = 0.3$ the measured value of w in the centre of the channel is approximately 10% of the maximum measured value of w.

The presence of a horseshoe vortex close to the side faces of the cube is revealed by the profiles of the normal component of the velocity v along a horizontal pathline $z/H > 0.5$ at $x/H = 0.5$, $y/H = 0.5$, which are shown in figure 5.17. Close to the side face of the cube, the velocity slightly increases

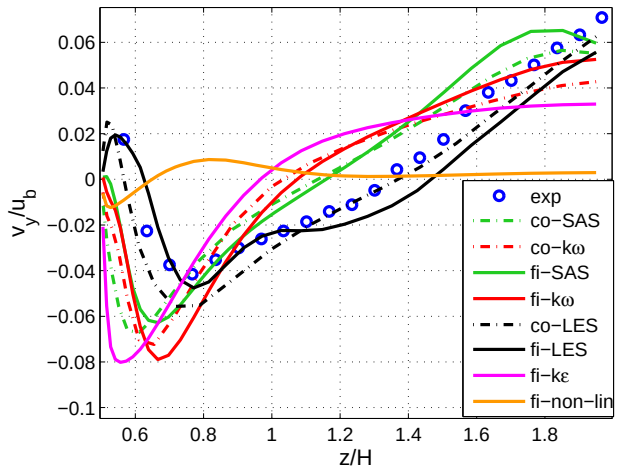

Figure 5.17: Profile of the y component of the velocity on a horizontal pathline ($z/H > 0.5$) at $x/H = 0.5$, $y/H = 0.5$.

due to a small corner vortex close to the bottom edge of the face, which is caused by the downwash of the horseshoe vortex. This downwash also determines negative velocities from $z/H \approx 0.6$ to $z/H \approx 1.4$. At $z/H \approx 1.4$

the horseshoe vortex interacts with the extensions of the outer horseshoe vortex, which formed around the upstream cube, whose downwash nullifies the upwash due to the inner vortex. Finally, according to the flow symmetry, in the centre of the channel ($z/H = 2$) the effects of the upwash generated by the outer vortex are superimposed to those of the outer vortex which bends around the side-neighbouring cube, determining an acceleration of the flow in the normal direction.

The best results are those of the large eddy simulations: the one on the fine grid is in good agreement with the measurements for $z/H < 1$, but shows a certain lack of accuracy moving towards the centre of the channel, while the LES on the coarse mesh tends to constantly underestimate v.

The non linear $k-\varepsilon$ model gives instead the poorest conformance with the experimental data: the prediction of the size and of the position of the horseshoe vortex is completely wrong. This result is coherent with the streamlines on the horizontal plane shown in figure 5.8(b), which are sensibly different from those obtained with the large eddy simulations: the size -and consequently its influence on the flow- of the horseshoe vortex is excessively underestimated.

All the other models tend to locate the vortex closer to the cube side surface and to underpredict its size: v changes in fact sign in $z/H \approx 1.1$. The resulting corner vortex is therefore smaller and the velocity gradient for $z/H < 1$ is higher. Furthermore since the horseshoe vortex remains closer to the cube side surface, its effects on the flow in the centre of the channel are weaker, and this results in an underestimation of v in $z/H = 2$.

5.5 Reynolds stresses

Figure 5.18 and figure 5.19 show the profiles of the streamwise component $\overline{u'u'}$ of the Reynolds stresses tensor on the vertical and horizontal pathlines.

Only the results obtained with the large eddy simulations have been considered, because the LES approach to the problem consists in resolving a wide range of motion scales, thus implying the adoption of a turbulence model only for the smallest scales. The prediction of the velocity fluctuations u' is there-

fore much more accurate than the one obtained with URANS simulations, where all turbulent scales are modelled, thus leading to fluctuations which are sensibly smaller than the effective ones.

With reference to figure 5.18, the peaks of the Reynolds stresses are located at $y/H \approx 1$, in correspondence to the generation and development of the thin intense shear layer on the rooftop of the cube. The maximum of $\overline{u'u'}$ is found at $x/H = 0.3$, where the shear layer is generated, due to the separation on the top face of the cube. Moving downstream of this position, the peak value attenuates, because of turbulent transport.

The profiles obtained with the LES on the fine mesh are in good agreement with the measurements in the near-wall region and for $y/H < 1$. Some discrepancies can be found in the centre of the channel, for $1.3 < y/H < 2.5$: they are very likely due to an insufficient grid resolution in this position; some further small disagreement can also be found in $x/H = -0.3$ and $x/H = 2.3$. It can also be observed that the results obtained with the coarse grid are overestimated compared to those obtained with the fine one. Similar re-

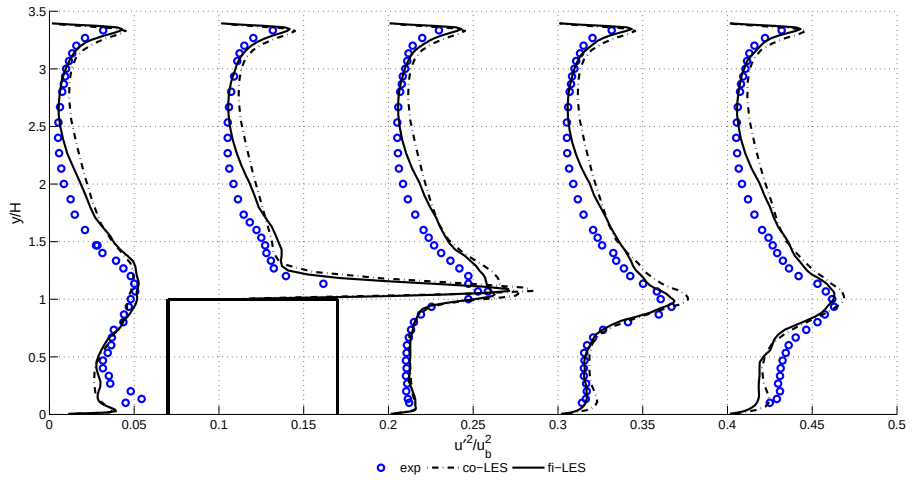

Figure 5.18: Profiles of streamwise Reynolds normal stress on the vertical pathlines at $z/H = 0$. Each profile (except $x/H = -0.3$) has been offset of 0.1 units from that of the previous one.

marks can be made about figure 5.19: the fine LES shows generally a good

agreement with the experimental data, and the coarse simulations tend to overpredict the value of the stresses. The peak value of $u^{'}$ is in proximity of the cube, as in the case of the vertical pathlines, according to the high shear production, and attenuates in the wake flow. The LES on the coarse grid

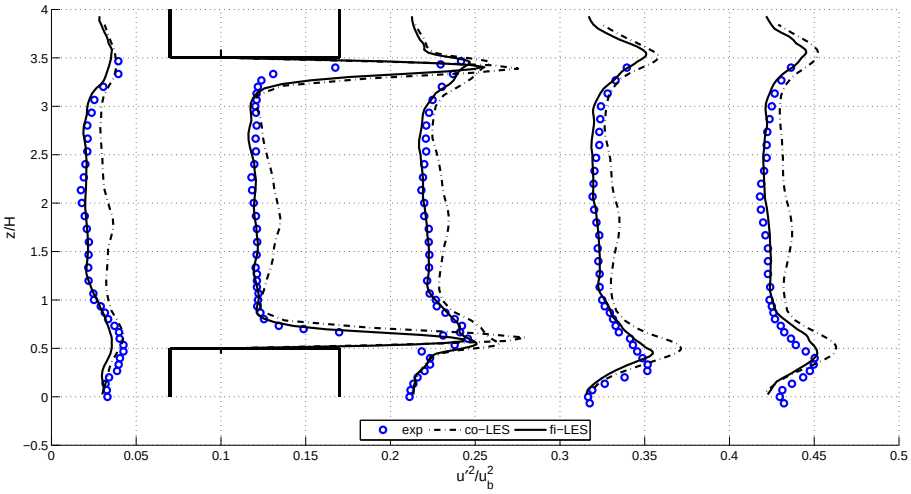

Figure 5.19: Profiles of streamwise Reynolds normal stress on the horizontal pathlines at $y/H = 0.5$. Each profile (except $x/H = -0.3$) has been offset of 0.1 units from that of the previous one.

still overestimates the Reynolds stresses: such a behaviour is typical for LES simulations. The use of a coarse grid has the same effect of a filter with a larger cutoff width and yields therefore overpredicted fluctuation values. In figure 5.20 and 5.21 the profiles of the Reynolds normal spanwise stress are shown. The value of the $\overline{w'w'}$ stres increases moving downstream of the cube, and has a maximum in $x/H \approx 2.3$. There is quite good agreement with the experimental data in $x/H \approx 0.3$ and $x/H \approx 1.3$ for both the horizontal and the vertical profiles; along the remaining pathlines the stresses are instead underestimated. In this case a direct influence of the grid refinement on the accuracy of the results cannot be detected, since the profiles obtained with the fine mesh show a higher discrepancy from the measured data. Figure 5.22 exhibits the profiles of the Reynolds shear stress on the horizontal pathlines. The peak value approximately coincides with the separation line

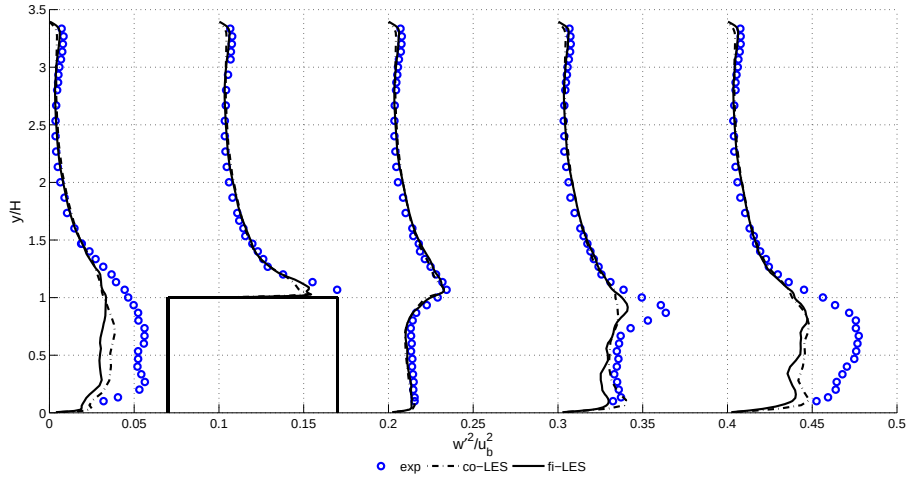

Figure 5.20: Profiles of spanwise Reynolds normal stress on the vertical pathlines at $z/H = 0$. Each profile (except $x/H = -0.3$) has been offset of 0.1 units from that of the previous one.

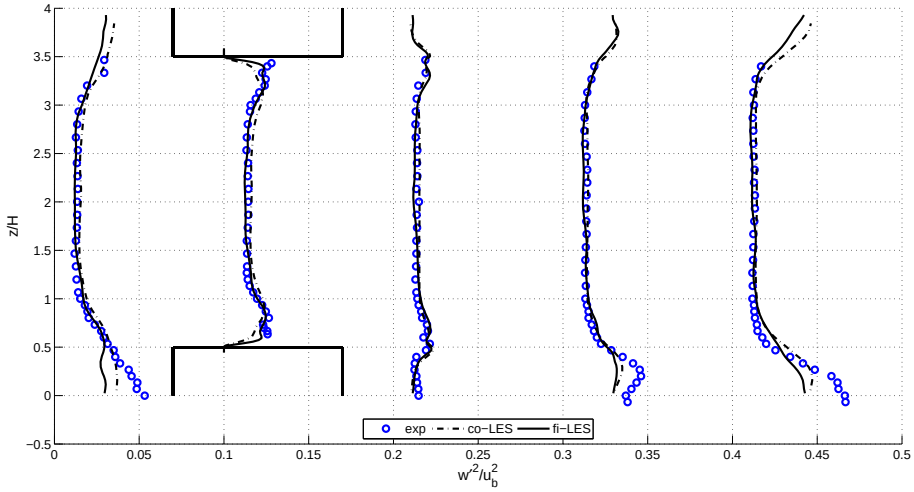

Figure 5.21: Profiles of spanwise Reynolds normal stress on the horizontal pathlines at $y/H = 0.5$. Each profile (except $x/H = -0.3$) has been offset of 0.1 units from that of the previous one.

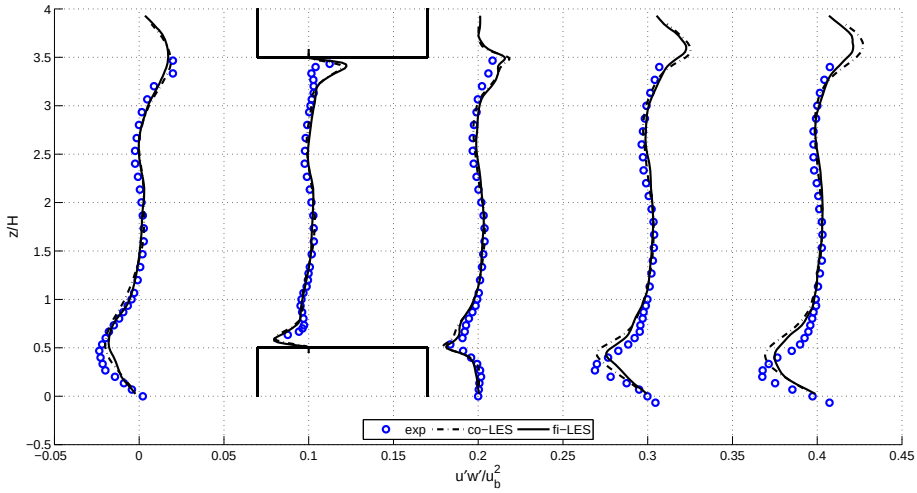

Figure 5.22: Profiles of $\overline{u'w'}$ Reynolds shear stress on the horizontal pathlines at $y/H = 0.5$. Each profile (except $x/H = -0.3$) has been offset of 0.1 units from that of the previous one.

originating from the back face of the cube, where the shear strain has its maximum. The results are in quite good agreement with the measurements: some discrepancy can be found in the wake, where the peak tends to remain in $z/H \approx 0.5$ instead of moving towards the centre of the channel and is slightly underestimated.

5.6 Temperature and heat transfer coefficient profiles

Temperature and heat transfer coefficient profiles refer to the horizontal and vertical pathlines summarised in figure 5.23 and in table 5.2. The measure-

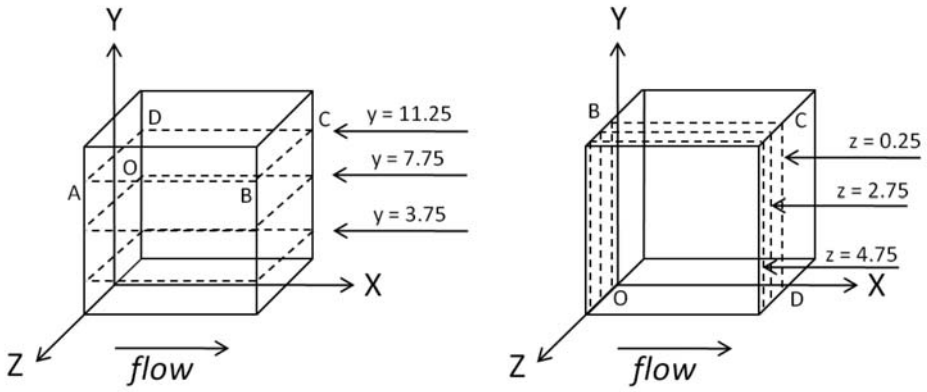

(a) Horizontal pathlines (b) Vertical pathlines

Figure 5.23: Temperature and heat transfer coefficient pathlines.

ments carried out by Meinders *et al* [7]. were performed by means of liquid crystal and infrared pictures of the surface temperature: the detailed profiles were then reported for the pathlines shown in figure 5.23; the results were all within the uncertainty limit of 10%. In the present work the heat transfer coefficient was calculated as in the experiments, by means of the following relation:

$$h = \frac{\Phi}{T_s - T_{ref}} \tag{5.2}$$

where Φ is the convective heat flux, T_s is the surface temperature and T_{ref} is the reference temperature, which is the air inlet temperature ($293\ K$). Heat flux through the base plate and radiative heat flux were not considered in the simulations: this results in a general overestimation of the temperature and of the heat transfer coefficient. The temperature field around the cube is strictly dependent from the turbulence phenomena: the numerical results exhibit therefore significant differences, which depend on the adopted turbulence model.

For the sake of clarity, with the only exception of the LES, only the results obtained with the fine grid will be shown: as it was in fact already noticed during the analysis of the velocity field, results are only slightly dependent on the grid refinement. Figure 5.24 shows the temperature and the heat transfer coefficient on the horizontal pathline at $y = 7.75\ mm$. On the windward

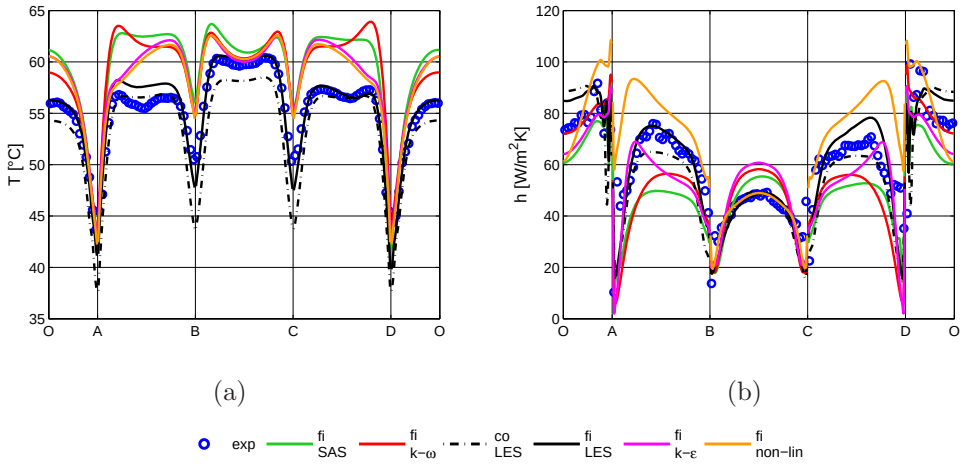

Figure 5.24: Temperature and heat transfer coefficient profiles along the horizontal pathline $y = 7.75\ mm$.

face temperature has a maximum in correspondence of the stagnation point, which is located approximately in the centre of the face (point O), and then sensibly decreases moving towards the front vertical edges. On the side faces local maxima can be found in proximity of the leading edge, due to flow separation, as it will be explained later on, discussing the results obtained for the top face. Finally on the back face, moving towards its centre, temperature first increases, as the cooling due to the shear weakens, and then slightly decreases, because of the cold air imported by the reverse wake flow.

The simulation that best agrees with the experimental data is the fine LES: the only discrepancies can be found in the section A-B, which is on the right side face, where the temperature is overestimated.

It is however interesting to notice that on the left face the predicted temperature is instead correct: there is therefore an asymmetry between the surface temperature of the two side faces, which is a consequence of the

asymmetry of the velocity field. This is also the case of the SAS model, which yields asymmetric velocity profiles and, as a consequence, asymmetric temperature profiles, especially in the wake region. On the other side the LES on the coarse grid tends to underestimate the temperature value on the front (sections O-A and D-O) and back faces (section B-C) of the cube, while on the sides the results show a better agreement with the measurements.

All the URANS simulations exhibit relevant discrepancies from the experimental data, except in the centre of the section B-C (back face), where the temperature value is correctly predicted: this is consistent with the correct reconstruction of the mean $u$profiles along the vertical and horizontal pathline in $x/H = 1.3$. On the front face the temperature overestimation is due both to the overprediction of the size of the recirculation and to the underestimation of the velocity: this causes a longer residence time of the fluid in the vortex and, consequently, the temperature increases.

The underestimation of the velocity of the flow impinging on the front face together with the incorrect reconstruction of the turbulence phenomena close to the side walls of the cube (see figure 5.17) yields also the overprediction of the side faces temperature.

Coherently with the prediction of the temperature profiles, the heat transfer coefficient profiles obtained with the LES on the fine grid exhibit a good agreement with the measurements. For what concerns the other simulations, instead, overestimations of the surface temperature lead to underestimations of the heat transfer coefficient, and vice versa. Local maxima of the heat transfer coefficient can be found in correspondence of the front edges (points A and D), where the strong acceleration of the flow enhances the heat removal, thus determining also local temperature minima. Figure 5.25 refers to the horizontal pathline at $y = 3.75\ mm$. The conformance of all the results with the experimental data is quite poor: this is essentially due to the fact that in proximity of the bottom wall -which is the case of the pathline $y = 3.75\ mm$- the heat transfer through the base plate, which was not modelled, is not negligible in comparison with the convective heat flux. All the performed computations yielded therefore an overestimation of the temperature values. Consistently with this overestimation of the temperature, all

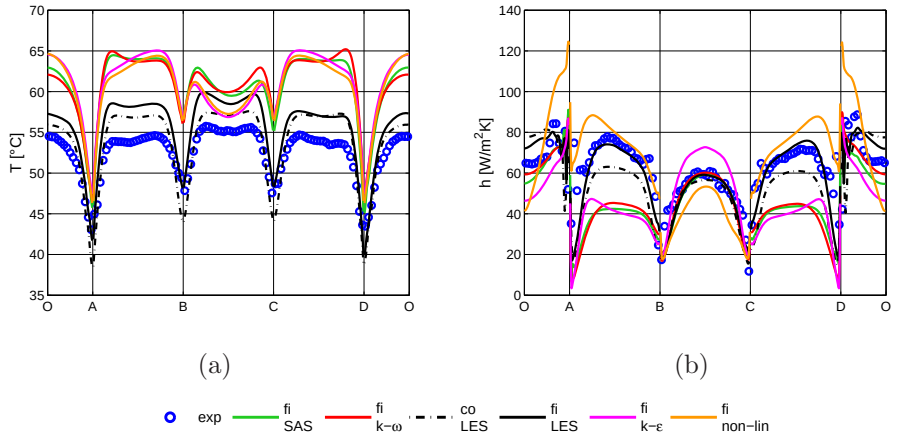

Figure 5.25: Temperature and heat transfer coefficient profiles along the horizontal pathline $y = 3.75\ mm$.

models generally tend to underestimate the heat transfer coefficient. Finally in figure 5.26 the results for the pathline $y = 11.25\ mm$ are shown. The

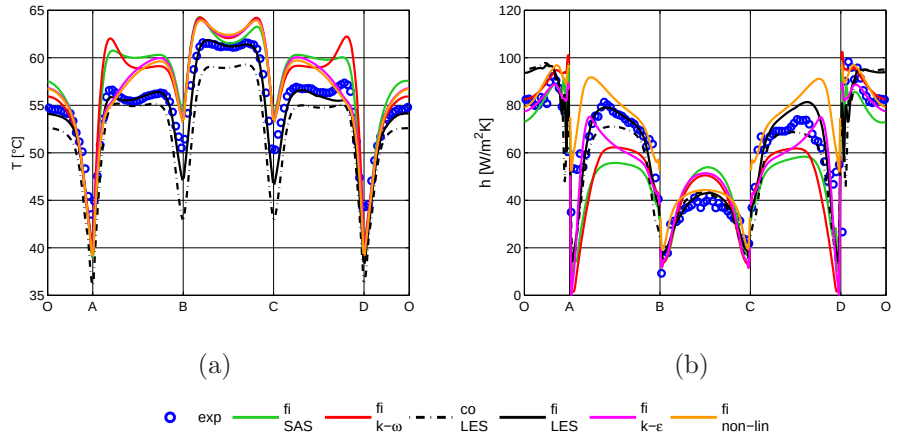

Figure 5.26: Temperature and heat transfer coefficient profiles along the horizontal pathline $y = 11.25\ mm$.

most accurate results are still those of the LES on the fine grid, while the simulation on the coarse grid tends to underestimate the local temperature. For what concerns the other models, the temperature profiles and, consequently, the heat transfer coefficient profiles show a better agreement with

the experimental data then in the previous cases. For example in the sections O-A and D-O the maximum difference between numerical and experimental results reduces to 6.5% of the measured temperature, while for $y = 3.75\ mm$ and $y = 7.75\ mm$ the maximum difference was respectively of 18% and 10%.

For $y = 11.25\ mm$ the influence of the recirculation in front of the cube becomes in fact weaker, consistently with the fact that the reconstruction of the mean streamwise velocity profiles on the vertical pathlines (see figure 5.9) is in good conformance with the measurements for $y/H \approx 1$. This implies that in proximity of the pathline $y = 11.25\ mm$ the velocity of the impinging flow is correctly predicted, thus leading to a more accurate prediction of the temperature profiles.

The highest discrepancy -about 9.5% of the measured temperature- can still be found on the side faces, but is less than along the two other horizontal pathlines, respectively 22% for $y = 3.75\ mm$ and 13% for $y = 7.75\ mm$. The next figures illustrate the temperature and heat transfer coefficient profiles for the vertical pathlines summarised in figure 5.23. The first two figures 5.27(a) 5.27(b) refer to the pathline $z = 0.25\ mm$, which is the closest to the cube midline. Like in the case of the horizontal pathlines, the best temperature

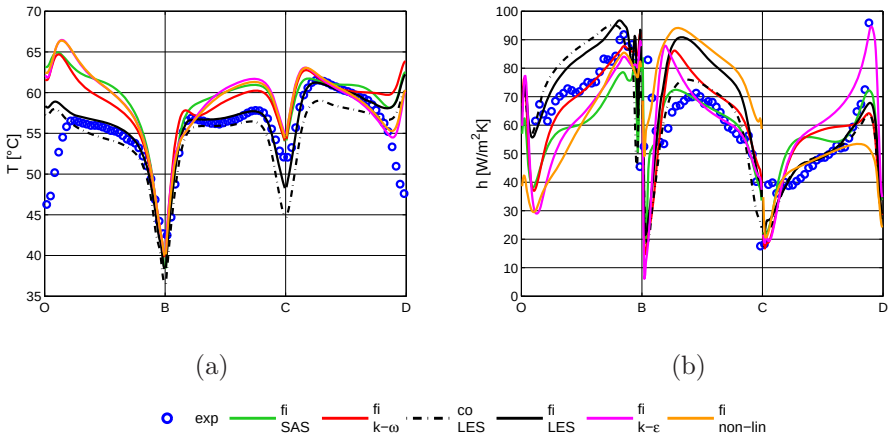

Figure 5.27: Temperature and heat transfer coefficient profiles along the vertical pathline $z = 0.25\ mm$.

and heat transfer coefficient profiles are still those obtained with the LES; the computation on the coarse grid has still the tendency to underestimate

the temperature values, but the discrepancy with the one on the fine grid is really appreciable only on the back face.

Since the heat flux through the base plate is not modelled, the temperature does not decrease in proximity of the bottom edge of the cube (points O and D). There are instead local peaks, which are due to the small corner vortices induced respectively by the horseshoe vortex on the front face and by the reverse wake flow on the back face. Heat is entrapped in these small structures, which act as a kind of insulation layer, thus preventing heat removal from the cube: this results in local minima of the heat transfer coefficient. Similar considerations can be made for the two other vertical pathlines, respectively $z = 2.75\ mm$ and $z = 4.75\ mm$, which are shown in figure 5.28. All the URANS simulations overestimate the temperature on the windward face: as mentioned in the case of the horizontal pathlines, this is due to the overestimation of the size of the recirculation in front of the cube and underestimation of the velocity of the impinging flow. This error becomes less important moving towards the top of the cube, as already noticed analysing the horizontal pathline $y = 11.25\ mm$, and consequently the discrepancy between numerical and experimental data decreases.

A local maximum of the heat transfer coefficient -and consequently a temperature minimum- can be found on the top leading edge (point B, figure 5.28(b) and 5.28(e)), where the heat removal benefits from the local acceleration of the flow.

On the top face, a slight local temperature maximum can be found in proximity of the leading edge, due to the small recirculation bubble which originates from the flow separation; since the amplitude the vortex shedding frequency is very high, the residence time of the fluid is quite low, thus preventing the local temperature to increase sensibly. It must be noticed that this flow feature is not detected by all models: the SAS and the two $k - \varepsilon$ are in fact not able to capture the effects of this small recirculation. Another local temperature minimum is located at the upper edge of the back face, where the cold air convected by the shear enhances the heat removal.

On the leeward face, moving towards the point D, the temperature first increases, as the cooling effect of the shear layer becomes weaker, then tends

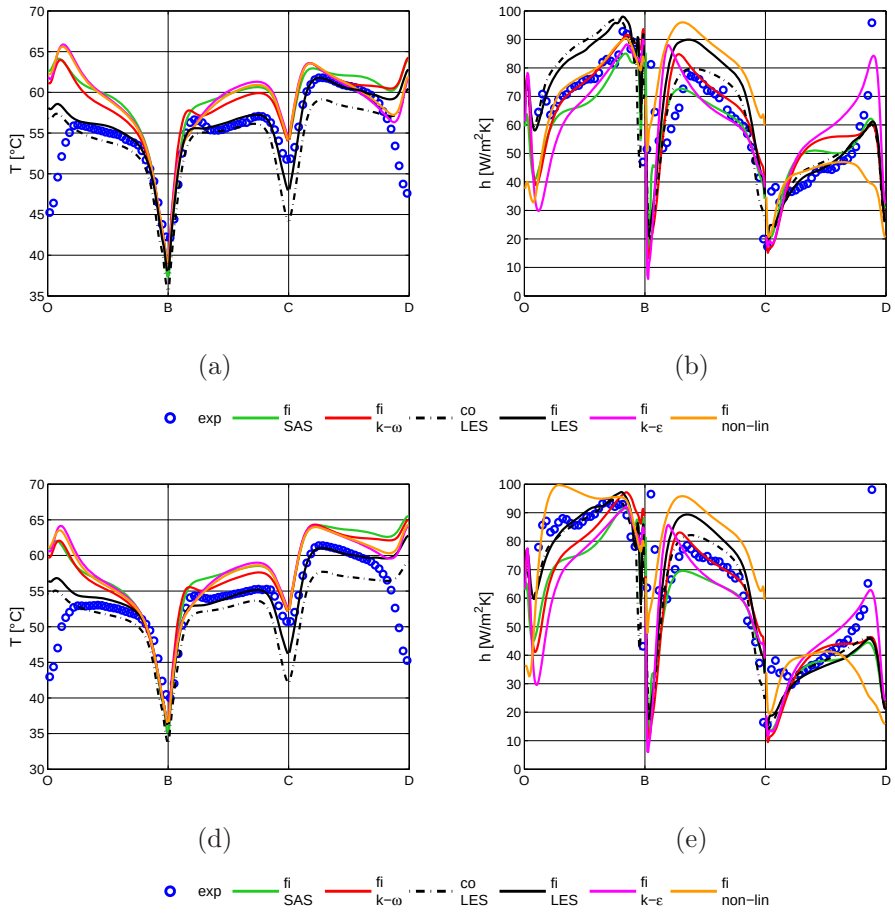

Figure 5.28: Temperature and heat transfer coefficient profiles along the vertical pathlines $z = 2.75\ mm$ and $z = 4.75\ mm$.

again to decrease, due to the cold air imported from the bottom by the wake reverse flow. Finally, as mentioned above, a temperature maximum is found, due to the corner vortex and the adiabatic boundary condition.

It must be noticed that, consistently with the good prediction of the mean streamwise velocity profile along the vertical pathline $x/H = 1.3$, the temperature profiles obtained with the URANS simulations for $z = 0.25\ mm$ and $z = 2.75\ mm$ are in good agreement with the measurements in the central part of the section C-D. The pathline $z = 4.75\ mm$ is instead too close to the back vertical edge and is therefore affected by the incorrect results obtained for the side faces.

5.7 Temperature fluctuations

In the next paragraphs some further results will be presented, for which experimental data are not available. As a consequence, the LES -in particular the one on the fine grid- will be used as a reference, since they have been proved to lead to the most accurate results.

As already mentioned, one of the aims of the present work is to investigate the accuracy of the prediction of the surface-temperature values and the possibility to capture local overheating; furthermore, an accurate prediction of the characteristics of the cyclic thermal loading is needed in order to allow a correct estimate of the thermal fatigue. It is therefore interesting to compare the prediction of the temperature fluctuations in different points of the cube faces. Figure 5.29 shows the three different points which have been considered; the coordinates are summarised in the adjacent table.

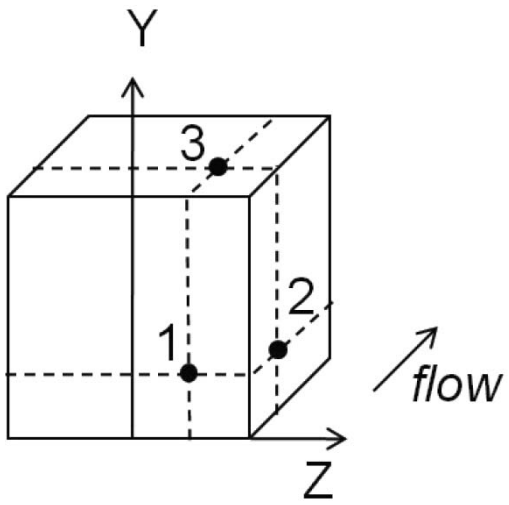

Figure 5.29: Measurement points of the fluctuations.

Point	x/H	y/H	z/H
p1	0	0.25	0.25
p2	0.25	0.25	0.5
p3	0.25	1	0.25

Table 5.4: Point coordinates

Since the results do not sensibly depend on the grid refinement, only simulations on the fine grid have been taken into account. In figure 5.30 the results obtained with the $k-\omega$, SAS and LES models are shown.

It is possible to notice that the LES predicts a fluctuation with the highest amplitude and frequency, thus leading to the most accurate reconstruction of the cyclic thermal loading. URANS models lead instead to smoother fluctuations with lower amplitude and a fundamental frequency which is the same of the vortex shedding. Furthermore, consistently with the results shown above, temperature values predicted by URANS simulations are sensibly higher.

All simulations capture the structure which forms in front of the cube, therefore in point *p1* the amplitude of the temperature fluctuation is almost the same (circa 1°C) for all the three considered models; however, the frequency predicted by the LES is sensibly higher and this results in a more efficient heat removal which determines a lower mean temperature value.

Another important remark is that the fluctuations predicted by the SAS and by the $k-\omega$ model are very similar: the SAS adds a random component but amplitude and frequency remain almost the same of the $k-\omega$. Similar remarks can be made for point *p2*: the fluctuation reconstructed by the $k-\omega$ behaves like a sinusoid with the same frequency of the vortex shedding, as well the one of the SAS, which still exhibits in addition also a weak random

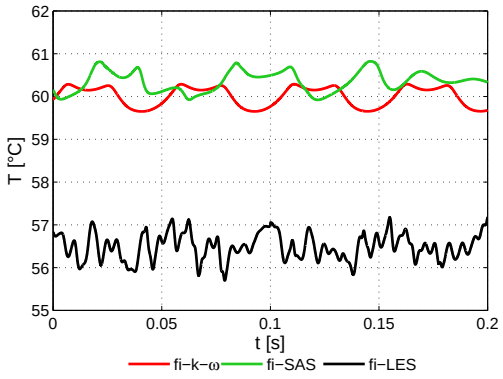

(a) *p1*

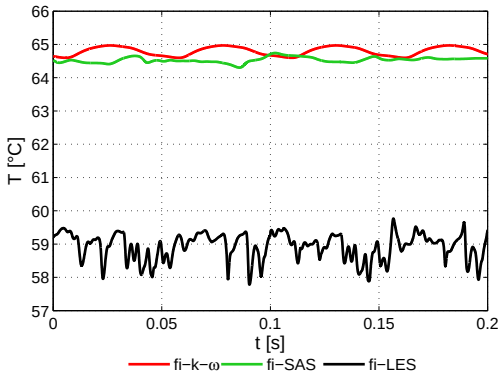

(b) *p2*

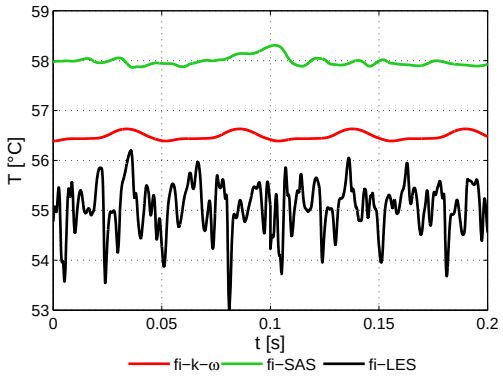

(c) *p3*

Figure 5.30: Temperature fluctuation.

component. On the other side the LES predicts a sensibly higher amplitude and frequency.

Finally on the top of the cube (point *p3*) the most considerable differences can be found: the URANS models predict a very smooth fluctuation, with a peak amplitude of circa 0.5°C and the same frequency obtained in the two previous points; the LES predicts instead a very high fluctuation amplitude (circa 3°C) and, again, a very high frequency.

5.8 Q iso-surfaces

Assuming that local pressure minima can be found in the centre of the vortices, it is possible to visualize turbulent structures by means of the following function:

$$Q = \frac{\nabla^2 p}{2\rho} \tag{5.3}$$

Q has been evaluated all over the computational domain, then all surfaces (Q *iso-surfaces*) on which $\frac{Q \cdot H^2}{u_b^2} = 7.55$ have been plotted, yielding the following figures (figure 5.31). With reference to figure 5.31 it can be noticed that LES are able to resolve a sensibly higher number of scales than the URANS simulations: the horseshoe vortex in front of the cube is clearly visible, as well as the recirculation bubbles on the side and on the top leading edge. Furthermore it is also possible to see structures which formed on the edges and are successively dragged away from the flow in the wake.

All these structures are not captured by the URANS models: the $k - \omega$ only detects the recirculation bubbles on the edges, the corner vortex at the bottom edge of the rear face and a small vortex in front of the cube, which bends around the corner. The SAS is instead also able to detect the presence of a more developed horseshoe vortex, but the visible structures are essentially the same of the $k - \omega$.

These results are consistent whit the prediction of the temperature fluctuation discussed in the previous chapter: although with some differences, unsteady phenomena in proximity of point *p1* (front face) are in fact captured by all models, therefore the fluctuation amplitude is almost the same

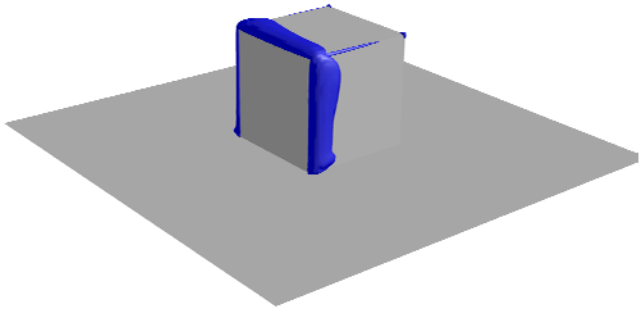

(a) $k - \omega$

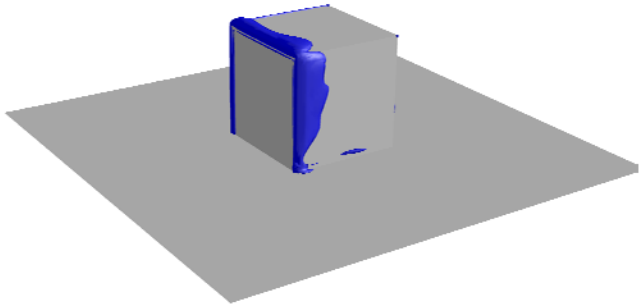

(b) SAS

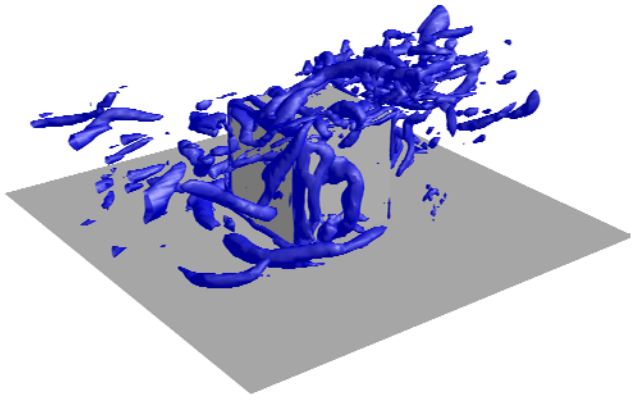

(c) LES

Figure 5.31: Q iso-surfaces.

in all cases. On the other side, considering URANS simulations, the absence of other significant structures and the lower frequency of the captured fluctuations (which results in a less efficient heat removal) determines a smoother fluctuation of the temperature.

5.9 Streamlines and temperature contours on the cube faces

In order to better appreciate the role of the turbulence model in the cooling of the cube faces, in the next figures the near-surface streamlines and the surface temperature contours will be shown. The five faces are folded out and mapped into a plane and the flow is from left to right; the colours are intended to give only a qualitative indication of the temperature distribution, and the colour scale is not the same for every figure. With reference to

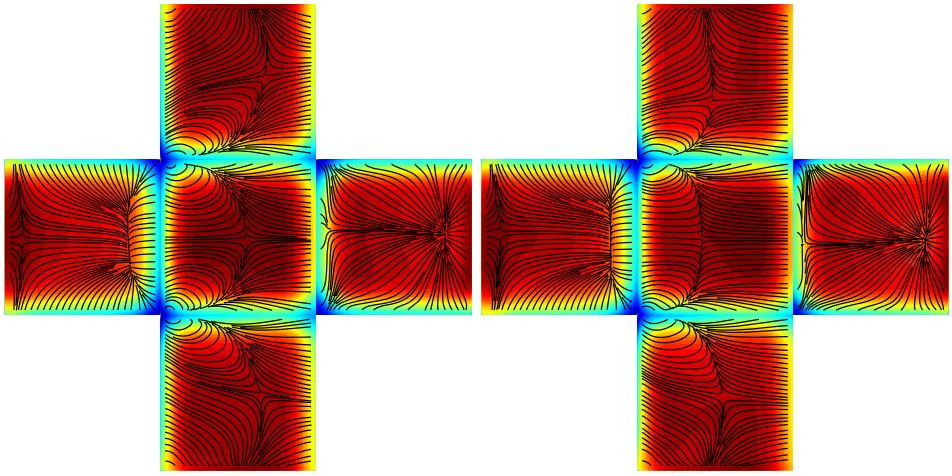

(a) Coarse LES (b) Fine LES

Figure 5.32: Near-surface streamlines and surface temperature contours.

figures 5.32(a) and 5.32(b), it can be noticed that the streamlines and the temperature contours on the front and back face are not affected by the different grid resolution. The impinging flow determines a stagnation line on the windward face, in proximity of the upper edge, while the imprint of the

corner vortex is visible close to the bottom edge. The temperature is low on the edges, where the flow strongly accelerates, and increases in the region of the corner vortex, due to the recirculation and to the absence of heat transfer through the base plate.

On the leeward face, a stagnation point is clearly visible in proximity of the bottom edge, due to the inward rotation of the wake vortex. The reverse flow imports low-temperature fluid which causes a local temperature minimum in the stagnation point; the fluid then heats up in the upwash flow towards the top edge. Like on the front face a local maximum can be found in the recirculation region close to the bottom edge.

The side and top faces exhibit more sensible differences: recirculations predicted by the LES on the coarse grid are larger than those obtained with the fine grid, due to the lack of resolution. A cooling effect can be detected close to the leading edges, due to the highly fluctuating character of the recirculations, which enhances the heat removal, and to the strong acceleration of the flow. Finally, a slight asymmetry of the streamlines can be noticed, consistently with the asymmetry of the velocity and temperature field. Also

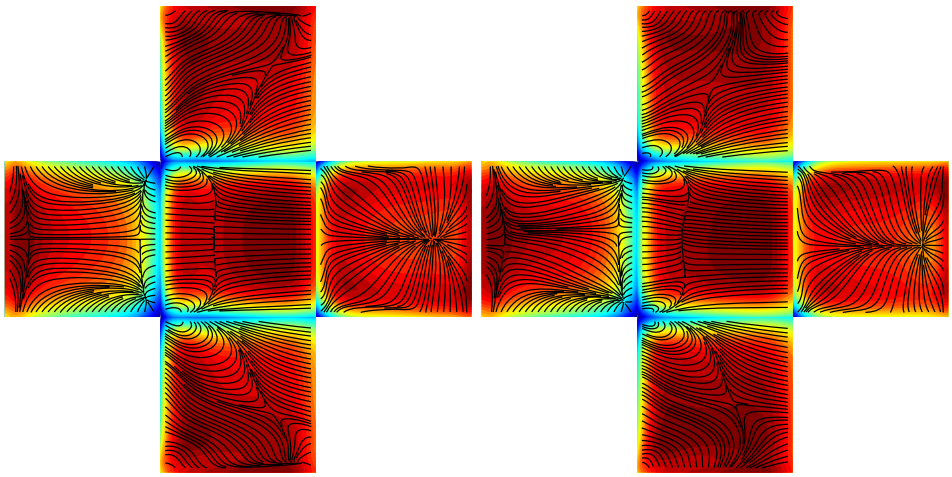

(a) $k-\omega$ (b) SAS

Figure 5.33: Near-surface streamlines and surface temperature contours.

the streamlines obtained with the $k-\omega$ and the SAS are quite similar (figure 5.33); for what concerns the front, top and back faces, the differences with

the results of the LES (which have been taken as a reference) are not very strong, except for the size of the recirculation on the top, which is smaller in the URANS simulations. The temperature distributions are also similar to those obtained with the LES, but, as noticed explaining the temperature profiles on the cube faces (section 5.6), the values are sensibly higher.

On the side faces, instead, the imprints of the recirculations are sensibly larger: as a consequence, heat is trapped in the side vortices and decreases the convective heat transfer. Finally in figure 5.34 the results of the standard

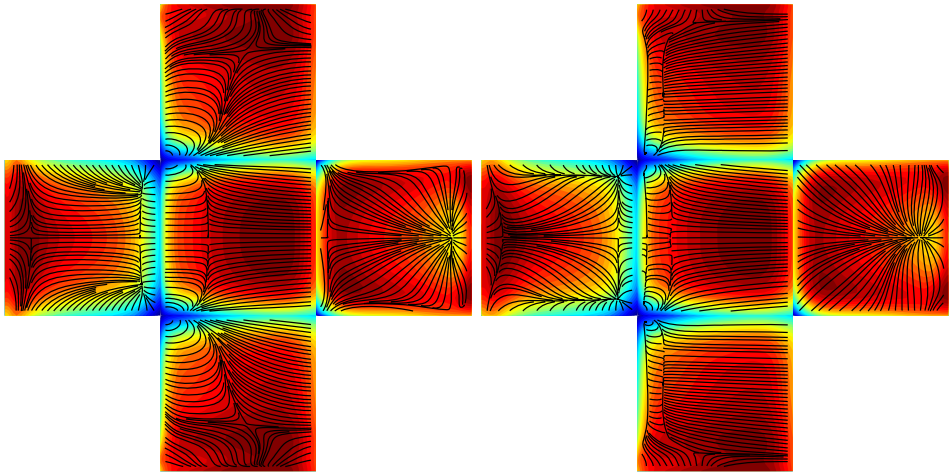

(a) $k-\varepsilon$ (b) Non linear $k-\varepsilon$

Figure 5.34: Near-surface streamlines and surface temperature contours.

$k-\varepsilon$ and non linear $k-\varepsilon$ are shown. The streamlines obtained with the standard model are quite similar to those obtained with the fine LES: besides some slight differences on the front and on the back side, the most significant discrepancy is the size of the imprints of the recirculations on the side faces, which are larger than those of the LES. Also the temperature contours do not exhibit considerable differences, except on the side faces, where a maximum can be found in proximity of the reattachment point.

With reference to figure 5.24 it can however be noticed that the predicted temperatures are -with the exception of the back face- higher than those obtained with the LES.

Finally the streamlines -and, consequently, the temperature contours-

obtained with the non linear $k - \varepsilon$ figure 5.34(b) are the ones which more sensibly differ from the results of the LES. The most remarkable characteristics are the two stagnation lines close to the vertical edges of the front face and the location of the recirculations on the top and side faces, which is slightly downstream of the edges. Furthermore, compared with the results of the LES, the size of the imprints of these recirculations is sensibly smaller and, in addition, a small corner vortex close to the bottom edge of the side faces appears: these are probably effects of the third order terms; this issue remains however currently unresolved, and requires further investigation.

Chapter 6

Computational costs

6.1 Computational costs

In the conclusion of the description of the adopted turbulence models (see paragraph 2.7), it has already been remarked that one of their fundamental characteristics is the number of further equations that they introduce, in order to achieve the closure of the system of equations discussed in chapter 2 and 3. Every additional transport equation due to turbulence modelling does in fact sensibly increase the computational costs, since its solution requires the complex discretization procedure explained in chapter 3.

As already mentioned, in this work mainly two-equations models have been adopted; two additional transport equations need therefore to be solved: one for the turbulence production and one for the turbulence dissipation. This is for example the case of the standard $k-\varepsilon$ and $k-\omega$ SST models.

Although they are also labelled as two-equations models, the non linear $k-\varepsilon$ and the SAS model are instead expected to be more expensive, under the point of view of the computational costs, because they introduce more operations in the solution procedure, mainly due to the evaluation of the source terms. This can be in fact a very complex procedure, since the evaluation of higher order derivatives is needed and consequently a further operation of discretization has to be carried out.

Finally large eddy simulations have been performed: in the LES approach no additional equations are introduced, since all the large turbulent scales are solved, while the smallest ones are modelled without the introduction of further transport equations. However, although less operations need to be carried out, it must be noted that to ensure a correct resolution of all captured scales a sufficiently fine computational grid has to be adopted, and this results in higher computational costs. LES are therefore sensibly affected by the grid characteristics, since the filter cutoff width Δ as well as the models for the subgrid scale turbulent viscosity strictly depend on the cell dimension Δ. It goes without saying that, if the Reynolds number increases, the range of turbulent scales becomes increasingly wider, thus implying the adoption of finer grids and hence the rise of the computational costs.

Nevertheless, in the present work LES turned out to be the most efficient

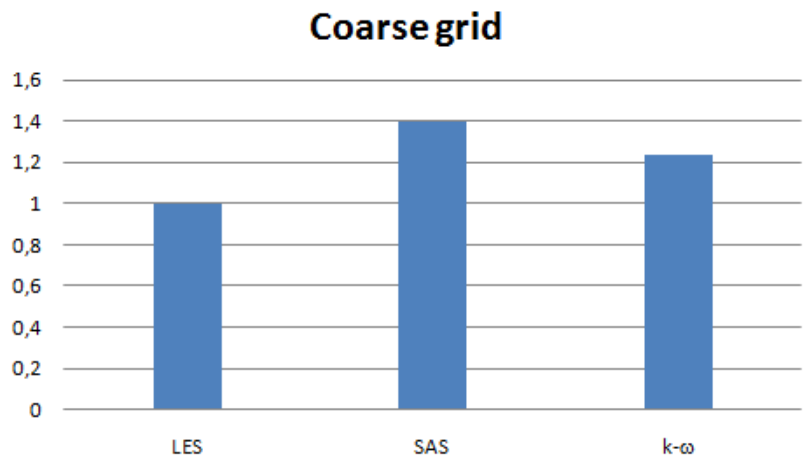

Figure 6.1: Average wall clock time per iteration: comparison between different simulations.

simulations: although they were designed for URANS applications, both the computational grids were in fact found to ensure a good accuracy of the results in proximity of the cube. Therefore, as no additional equations had to be solved, the LES computations were sensibly faster than those with other models. In figure 6.1 and 6.2 the average wall clock time per iteration (based on 100 iterations) needed by every model is shown. The time is made dimensionless by means of the wall clock time of the LES, which have been taken as a reference, since they needed the lowest computational time. As it was expected, the $k-\omega$ SST model requires more computational time than a LES for every single iteration, because two additional transport equations have to be solved. Furthermore, the SAS model turns out to be even slower, as it implies the evaluation of a complex source term. The computational times obtained with the fine grid are shown in figure 6.2: The LES is still the fastest simulation, while the $k-\omega$ and the SAS still need an increasing computational time.

The standard $k-\varepsilon$ model also needs mor time than a LES; however it is important to remark that, in spite of a higher computational time for single iteration, it allowed to obtain results very quickly, since it was not able to capture the unsteadiness of the flow and it was therefore not necessary to

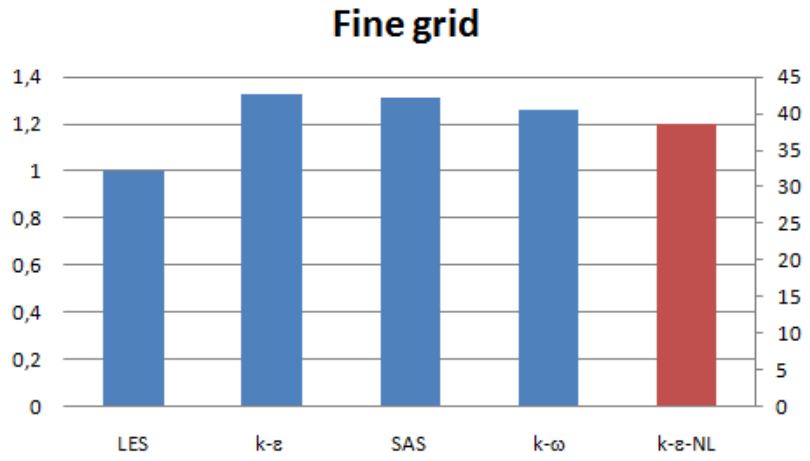

Figure 6.2: Average wall clock time per iteration: comparison between different simulations (fine grid). The scale on the right refers to the non linear $k - \varepsilon$.

collect time statistics, thus drastically reducing the needed computational time. Furthermore, since the obtained results were relatively good, the standard $k - \varepsilon$ was proved to be an excellent model to yield a fast qualitative description of the mean characteristics of the flow around the cube.

On the other side the non linear $k - \varepsilon$ model turned out to be the most costly one, due both to the complexity of the source terms which had to be evaluated and to its implementation, which prevented to adopt a non-iterative time advancement. Furthermore the stiffness of the introduced source terms made particularly difficult the convergence of the outer iterations cycle. As a consequence, a large number of iterations (40) per time step was needed, thus making the non linear $k-\varepsilon$ model circa 40 times slower than the LES.

Chapter 7

Conclusions

7.1 Conclusions

Different turbulence models were used to simulate the fully developed turbulent flow and heat transfer from a matrix of wall-mounted cubes in a plane channel: the results were then compared with the corresponding experimental data of Meinders *et al.* [7]. From the analysis of the obtained results it is possible to draw the following conclusions:

1. Although the computational grids were not specifically designed for large eddy simulations, these turned out to be the most accurate and less costly computations. Both the flow and the heat transfer were accurately reconstructed, with good conformance with the experimental data (also slight asymmetries of the velocity field were captured). Some slight discrepancies were due to an excessive cell-size grading, which affected the results in the upper part of the channel; these problems did however not affect the region in proximity of the cube, where the grid resolution was instead high enough and similar among the two adopted grids.

2. SAS simulations, which should be an hybrid between LES and URANS computations, did not lead to the expected results: they behaved in fact mainly as a $k-\omega$ model, without introducing sensible modifications due to the resolution of smaller scales. The most plausible causes of this are two: first of all the Reynolds number of the analysed case was relatively small, so there might have been a non optimal separation between URANS and LES features of the model. Second, the use of periodic boundary conditions, together with very different grid resolutions inside the domain, could have led to a not optimal activation of the LES mode of the model.

3. The $k-\varepsilon$ model was not able to detect the unsteadiness of the flow, but it could quite accurately reconstruct the mean flow features, although it was not able to capture local peaks of the velocity profiles, especially in correspondence of recirculations. However the very low computational time, due to the fact that the collection of time statistics was not

needed, made it the model with the best cost-benefit ratio, if only a qualitative evaluation of the mean flow features is needed.

4. The $k-\omega$ SST model was instead able to capture the unsteadiness of the flow, but failed to reconstruct the position of the recirculations up- and downstream of the cube. Unlike the SAS model, it was not able to detect the slight flow asymmetry.

5. The non linear $k-\varepsilon$ model turned out to be the most problematic one: it lead to an excessive stretching of the upstream vortex and failed to reconstruct the structures in proximity of the cube, probably due to effects of the third order terms. These terms also determined a considerable stiffness of the model, which had convergence problems inside the outer iterations cycle. Furthermore the model implementation prevented to adopt a non-iterative time advancement method, thus implying a sensibly higher computational time.

6. It has not been possible to give a proper explanation of the asymmetry of the velocity fields obtained with SAS and LES: this is however an interesting feature of the flow and should be carefully investigated.

7. For what concerns the temperature field, the most accurate predictions are those of the LES on the fine grid. The LES on the coarse grid has instead a tendency to underestimate temperatures. URANS simulations, on the other side, constantly overestimate temperatures: good agreement with the experimental data can be found only on the back face.

8. The results of the URANS simulations do not strictly depend on the adopted grid: those obtained with the fine mesh are in fact only slightly more accurate than those of the coarse mesh. On the other side, as it was expected, the LES exhibit a stronger grid-dependence, especially in the computation of the Reynolds stresses and the temperature field.

Bibliography

[1] Ansys Inc., *FLUENT 12.0 - Theory guide*, 2009.

[2] Y. Cheng, F.S. Lien, E. Yee, R. sinclair, *A comparison of large eddy simulations with a standard $k-\varepsilon$ Reynolds-averaged Navier-Stokes model for the prediction of a fully developed turbulent flow over a matrix of cubes*. J. of Wind Engineering and Industrial Aerodynamics 91 (2003), pp. 1301-1328

[3] J. H. Ferziger, M. Perić, *Computational methods for fluid dynamics*. Springer Verlag, 2002

[4] A. Hellsten, P. Rautaheimo (ed.), *Proceedings of the 8^{th} ERCOFTAC/IAHR/COST Workshop on Refined Turbulence Modelling*. 1999.

[5] P. Lampitella, *The quality and reliability of large eddy simulation in a commercial CFD software*, M. sc. thesis, Seconda Università degli studi di Napoli, Aversa, Italy, 2009.

[6] LES in Italy Group, *A comparative test for assessing the performances of large eddy simulation codes*, Proc. of XX AIMETA Congress, Bologna, 2011.

[7] E. R. Meinders, K. Hanjalić, *Vortex structure and heat transfer in turbulent flowover a wall-mounted matrix of cubes*. Int. J. of Heat and Fluid Flow 20 (1999) pp. 255–267

[8] E. R. Meinders, T. H. Van Der Meer, K. Hanjalić, *Local convective heat transfer from an array of wall-mounted cubes*. Int. J. of Heat and Mass Transfer 41, vol. 2 (1998) pp. 335–346

[9] F. R. Menter, Y. Egorov, *Development and application of SST-SAS turbulence model in the DESIDER Project*. Notes on Numerical Fluid Mechanics and Multidisciplinary Design 97, pp. 261-270, Springer Verlag, 2008

[10] F. R. Menter, Y. Egorov, *The Scale-Adaptive Simulation method for unsteady turbulent flow predictions. Part 1: theory and model description*. Flow, Turbulence and Combustion 85, pp. 113-138, Springer Verlag, 2010

[11] R. Mereu, *Non Linear Eddy Viscosity RANS-Based Models in the Framework of Complex Flows*.Ph. D. thesis, Politecnico di Milano, Milan, Italy, 2009.

[12] B. Ničeno, A.D.T. Dronkers, K. Hanjalić, *Turbulent heat transfer from a multi-layered wall-mounted cube matrix: a large eddy simulation*. Int. J. of Heat and Fluid Flow 23, pp. 173-185 (2002).

[13] S. B. Pope, *Turbulent flows*. Cambridge University press, 2009

[14] H. Schlichting, *Boundary layer theory*, 7^{th} edition, Mc Graw-Hill, 1979

[15] W. Rodi, *A new algebraic relation for calculating the Reynolds stresses*, ZAMM 56 (1976), pp. 219-221

[16] promp L. Thielen, H. J. J. Jonker, K. Hanjalić, *Symmetry breaking of flow and heat transfer in multiple impinging jets*. Int. J. of Heat and Fluid Flow 24, (2003), pp 444-453

[17] M. Van Dyke, *An Album of Fluid Motion*. Parabolic Press, 1982

[18] R.W.C.P. Verstappen, R.M. van der Velde, *Symmetry preserving discretization of heat transfer in a complex turbulent flow*. J. of Engineering Mathematics, vol. 54 (2006), pp. 299-318

[19] R.W.C.P. Verstappen, R.M. van der Velde, A. E. P. Veldman *DNS of turbulent flow and heat transfer in a channel with surface mounted cubes*. ECCOMAS, 2000, Barcelona

[20] H. K. Versteeg, W. Malalasekera, *An introduction to computational fluid dynamics. The finite volume method*. Pearson Educational, 2007

[21] D. C. Wilcox, *Turbulence modeling for CFD*. DCW Industries, 2006